^{3}He Ionization Chambers as Neutron Beam Monitors for the NPDGamma Experiment

by

R. Chad Gillis

A Thesis
Submitted to the Faculty of Graduate Studies
in Partial Fulfillment of the Requirements
for the Degree of

Master of Science

Department of Physics and Astronomy
University of Manitoba
Winnipeg, Manitoba

THE UNIVERSITY OF MANITOBA

FACULTY OF GRADUATE STUDIES

*****

COPYRIGHT PERMISSION

^{3}He Ionization Chambers as Neutron Beam Monitors for the NPDGamma Experiment

BY

R. Chad Gillis

A Thesis/Practicum submitted to the Faculty of Graduate Studies of The University of Manitoba in partial fulfillment of the requirement of the degree

OF

MASTER OF SCIENCE

ABSTRACT

NPDGamma is a low energy nuclear physics experiment that is in the final stages of preparation for a high precision measurement of A_γ, the parity-violating correlation between gamma-ray momentum direction and neutron spin direction in the reaction $\vec{n} + p \rightarrow d + \gamma$. Of crucial importance to this experiment are the beam monitors, ^{3}He ionization chambers that monitor the apparatus by observing the flux of the polarized pulsed neutron beam. In this thesis, it is verified that the beam monitors are simple, reliable, low noise detectors that are very effective at monitoring the rate of neutrons incident on them. These properties allow them to provide continuous knowledge of the beam polarization throughout an asymmetry measurement by observing the time of flight-dependent beam flux downstream of the beam polarizer. The ^{3}He content of these beam monitors was measured, and a Monte Carlo calculation was performed to determine the average amount of energy deposited in the chambers per detected neutron. It was verified that the beam monitor signals can be interpreted to reproduce the known time of flight dependence of beam flux from the neutron source, and that the neutron beam polarization can be measured at the 2 % level from direct measurements of the transmission of the beam through the beam polarizer. An absolute calibration of the beam monitors was attempted by comparing the beam monitor signals to a Monte Carlo calculation of the beam flux. This calibration, which is not important to analysis for the NPDGamma experiment, gave rise to a discrepancy that will require further measurements in order to be resolved.

This work is dedicated

to my parents and to my brother.

ACKNOWLEDGEMENTS

I would like to begin by thanking my supervisor, Professor Shelley Page. Through her resourcefulness and initiative, she has provided me with very amazing opportunities, and has demonstrated patience and support in working with me through details that I have encountered in my work.

I would also like to thank all of my friends and acquaintances of Los Alamos who have helped to make my time there very positive and fruitful. In particular, I would like to thank those that I've worked with on a daily basis, who behaved as mentors for me during my time at the lab, and who were willing to invest time to make me feel a part of the team: David Bowman, Michael Gericke, Greg Mitchell, Seppo Penttilä, Gil Peralta, Des Ramsay, Pil-Neyo Seo, Scott Wilburn, with periodic appearances of others. It's a privilege to work as a student surrounded by talented and knowledgeable people.

The staff at the P-23 group office at Los Alamos National Laboratory, and at the Department of Physics and Astronomy at the University of Manitoba, have worked very hard through the complications of my paperwork, and this has not gone unnoticed. Perhaps this is the place to also give many thanks to Gilles Roy for insight that he has provided into the vagaries of life and experimental physics.

I would also like to acknowledge the important financial support of the University of Manitoba and of NSERC Canada.

Finally, this list of acknowledgements would be incomplete without a recognition of all of the teachers and professors that have taught me what I know today.

THE NPDGAMMA COLLABORATION

Ricardo Alarcon [1], Libertad Barron [1], J. David Bowman (spokesman) [2], Roger D. Carlini [3], Wangchun Chen [4,5], Timothy E. Chupp [6], Kevin Coulter [6], Chris Crawford [7], Silviu Covrig [8], Mikayel Dabaghyan [8], Dharmin Desai [7], Stuart J. Freedman [9], Thomas R. Gentile [5], Michael T. Gericke [10], R. Chad Gillis [10], Geoffrey L. Greene [7,11], F. William Hersman [8], Takashi Ino [12], Gordon L. Jones [13], Martin Kandes [6], Bernhard Lauss [9], Mark Leuschner [4], Bill Losowki [14], Robert Mahurin [7], Yasuhiro Masuda [12], Jiawei Mei [4], Gregory S. Mitchell [2], Suguro Muto [12], Hermann Nann [4], Shelley Page [10], Seppo Penttilä [2], W. Des Ramsay [10,15], Dennis Rich [4,5], Americo Salas-Bacci [2], Satyaranjan Santra [16], Pil-Neyo Seo [17], Eduard Sharapov [18], Monisha Sharma [6], Todd Smith [19], W. Michael Snow [4], Takeyasu Ito [7], W. Scott Wilburn [2], Vincent Yuan [2], Hongguo Zhu [8]

1) Arizona State University, Tempe, AZ; 2) Los Alamos National Laboratory, Los Alamos, NM; 3) Thomas Jefferson National Accelerator Facility, Newport News, VA; 4) Dept. of Physics, Indiana University, Bloomington, IN; 5) National Institute of Standards and Technology, Gaithersburg, MD; 6) Dept. of Physics, Univ. of Michigan, Ann Arbor, MI; 7) Dept. of Physics, Univ. of Tennessee, Knoxville, TN; 8) Dept. of Physics, Univ. of New Hampshire, Durham, NH; 9) Univ. of California at Berkeley, Berkeley, CA; 10) Dept. of Physics, Univ. of Manitoba, Winnipeg, MB; 11) Oak Ridge National Laboratory, Oak Ridge, TN; 12) High Energy Accelerator Research Organization (KEK), Tsukuba, Ibaraki, Japan; 13) Dept. of Physics, Hamilton College, Clinton, NY; 14) Indiana University Cyclotron Facility, Bloomington, IN; 15) TRIUMF, Vancouver, BC; 16) Bhabbha Atomic Research Center, Mumbai, India; 17) Dept. of Physics, North Carolina State University, Raleigh, NC; 18) Joint Institute of Nuclear Research, Dubna, Russia; 19) Dept. of Physics, Univ. of Dayton, Dayton, OH

Funding for the NPDGamma experiment has been provided by the US DOE, the NSF, TRIUMF and NSERC Canada.

TABLE OF CONTENTS

LIST OF FIGURES

LIST OF TABLES

Chapter 1

THE MOTIVATION BEHIND THE NPDGAMMA EXPERIMENT

1.1 Introduction to this chapter

The NPDGamma experiment is a low-energy, high-precision nuclear physics experiment that, through measurement of a parity-violating observable in a simple system, aims to provide a better understanding of the weak interaction between hadrons (strongly interacting particles which are composed of quarks).

One of the most fundamental problems of nuclear physics is an accurate description of the internucleon potential. Significant advances have been made in this area by representing the strong interaction between nucleons (protons and neutrons) in terms of a meson exchange model, discussed for example in reference [1]. However, despite five decades of investigation, an equivalent model for the weak interaction between nucleons has not been rigorously tested by experiment.

At the level of noncomposite fermions (leptons and quarks), the weak interaction has been successfully modeled in terms of the exchange of W and Z bosons. However, knowledge of the weak interaction in hadronic systems has been limited by the inevitable involvement of the strong interaction. For this reason it is useful to take advantage of a feature that only the weak interaction is known to exhibit: it violates parity symmetry.

Due to the relative size of strong and weak probability amplitudes, parity-violating asymmetries are typically superposed on parity-conserving signals that are many orders of magnitude larger. As a result, the measurement of such asymmetries is slowed by the requirement for high statistical precision and the by the need for an extremely careful study

of systematic effects.

One solution to this problem has been to look for signals in systems where the parity-violating effect is magnified by structural effects in complex nuclei. The unfortunate consequence of this approach is that the observables are interpreted in terms of quantum mechanical matrix elements for which the wave functions of the systems must be known. The very complexity which makes the parity-violating effects more measurable gives rise in many cases to conflicting interpretations.

As a solution to this problem, it is necessary to perform difficult but practicable measurements in simple systems. For the case of internucleon interactions, the simplest system is one composed of two nucleons: the proton-proton (pp) or neutron-proton (np) system. Parity violation has been observed to the level of 7 standard deviations in the pp system [2] but has not to date been observed in the np system.

Measurements of parity-violating asymmetries in the np system are necessary for isolating important parameters in the theory of the hadronic weak interaction. The goal of the NPDGamma experiment is to measure such an asymmetry to a precision that will allow for a measurement of the coupling constant associated with weak pion exchange (as discussed in section 1.6.2). In doing so, NPDGamma will provide an important test of current models of the hadronic weak interaction.

1.2 Quantum mechanics and the parity transformation

The parity (also referred to as spatial inversion) transformation, π, is a linear and discrete mathematical operation. In classical physics, π transforms a system such that the magnitude of the position vector $\mathbf{r}$ is conserved and its direction is reversed:

$$\mathbf{r} \xrightarrow{\pi} -\mathbf{r}. \tag{1.1}$$

In quantum mechanics, physical systems are described in terms of states $|\psi\rangle$ that exist in a linear ket space. Observables are described in terms of Hermitian operators A. Expectation values of A are determined by computing the inner product $\langle\psi| A |\psi\rangle$ where $\langle\psi|$ is the bra vector dual to $|\psi\rangle$.

The notation used to describe the action of π on state vectors is:

$$|\psi\rangle \xrightarrow{\pi} \pi|\psi\rangle \tag{1.2}$$

$$\langle\psi| \xrightarrow{\pi} \langle\psi|\pi^\dagger. \tag{1.3}$$

The result of π in the quantum mechanical case is to transform the expectation value of the position operator $\hat{\mathbf{r}}$ so that it converts to its negative:

$$\langle\psi|\pi^\dagger\hat{\mathbf{r}}\pi|\psi\rangle = -\langle\psi|\hat{\mathbf{r}}|\psi\rangle = \langle\psi|(-\hat{\mathbf{r}})|\psi\rangle. \tag{1.4}$$

As equation (1.4) also illustrates, this is equivalent to stating that the state vectors remain unchanged while the position operator becomes its negative.

Now consider the projection of $\pi|\psi\rangle$ onto $|\phi\rangle$, which can be calculated as an integral over all space:

$$\begin{aligned}\langle\phi|\pi|\psi\rangle &= \int\langle\phi|\pi|\mathbf{r}'\rangle\langle\mathbf{r}'|\psi\rangle\,\mathbf{dr}' = \int\langle\phi|-\mathbf{r}'\rangle\langle\mathbf{r}'|\psi\rangle\,\mathbf{dr}' \\ &= \int\langle\psi|-\mathbf{r}'\rangle^*\langle\mathbf{r}'|\phi\rangle^*\,\mathbf{dr}' = \langle\phi|\pi|\psi\rangle^*\end{aligned} \tag{1.5}$$

where $|\mathbf{r}'\rangle$ is an eigenket with eigenvalue $\mathbf{r}' \in \Re^3$ of the operator $\hat{\mathbf{r}}$ [1]. Using the identity $\langle\phi|A|\psi\rangle \equiv \langle\phi|A^\dagger|\psi\rangle^*$, which applies for an arbitrary quantum mechanical operator A, it follows from (1.5) that π is Hermitian:

$$\pi = \pi^\dagger. \tag{1.6}$$

From the point of view of a physical observation, two successive parity transformations must be indistinguishable from the identity operation. This leads to the requirement that $\pi^2 = exp(i\theta)\mathbb{1}$ where θ is an arbitrary real number and $\mathbb{1}$ is an identity operator. Without loss of physical generality, it is possible to choose $exp(i\theta) = 1$, and thus to arrive at the result that π is unitary:

$$\pi = \pi^{-1}. \tag{1.7}$$

---

[1] At this stage, care is taken to distinguish between the Cartesian coordinate r and the operator $\hat{r}$. For the rest of this chapter, observables are represented as operators, and so such a distinction is no longer of importance. The use of the caret to denote an operator is therefore dropped.

Hermitian operators may only have real eigenvalues, and unitary operators may only have eigenvalues of unit magnitude. As a consequence, the eigenvalues of π are restricted to $+1$ or -1. States with parity eigenvalue $+1$ are referred to as parity-even, and states with parity eigenvalue -1 are referred to as parity-odd. Similarly, operators are referred to as parity-even if they commute with π or parity-odd if they anticommute with π.

1.3 Vectors and pseudovectors; scalars and pseudoscalars

In quantum mechanics, an operator $\mathbf{V}$ with components V_i is said to be a vector operator if the expectation values of V_i are altered as:

$$\langle\psi|\, U^\dagger(R) V_i U(R)\, |\psi\rangle = \sum_j R_{ij} \langle\psi|\, V_j\, |\psi\rangle\,, \tag{1.8}$$

where $U(R)$ is a unitary transformation that corresponds to rotation of conventional vectors by a matrix with Cartesian elements R_{ij}. Angular momentum, linear momentum and position operators are vector operators.

It is often useful to classify operators further in terms of how they transform under a parity transformation. It has already been stated (equation (1.4)) that the position operator is odd under a parity transformation.

It can also be shown that the linear momentum operator $\mathbf{p}$ is odd under a parity transformation:

$$\pi^\dagger \mathbf{p} \pi = -\mathbf{p}. \tag{1.9}$$

This statement is true given the facts that 1) momentum is the generator of translations in position space; and that 2) translation followed by parity is the same as parity followed by translation of equal magnitude but in the opposite direction.

It can also be shown that the angular momentum operator $\mathbf{J}$ is even under a parity transformation:

$$\pi^\dagger \mathbf{J} \pi = \mathbf{J}. \tag{1.10}$$

This statement is true given the facts that 1) angular momentum is the generator of rotations in position space; and that 2) the parity operator commutes with the rotation operator.

Scalar operators are operators that are unaltered by an arbitrary rotation. Scalar quantities can also be subdivided into two categories based on how they behave under a parity transformation. Some scalars such as the dot product between an axial vector and a polar vector (e.g. $\mathbf{J} \cdot \mathbf{p}$) reverse sign under a parity transformation. Such quantities are referred to as pseudoscalars. Ordinary scalars, such as the dot product between two vectors of the same type, are invariant under a parity transformation.

1.4 The Hamiltonian operator, time development and parity mixing

The evolution of a quantum mechanical state ket $|\psi\rangle$ between times t_0 and t is determined by the time evolution operator $U(t, t_0)$, the form of which is stated in equation (1.12). H is the Hamiltonian operator which for a two body system is shown in equation (1.13). The potential V describes the interaction between the particles. The momentum associated with the relative coordinate between the two bodies is given by $\mathbf{p}$ and the reduced mass is given by μ.

$$|\psi(t)\rangle = U(t, t_0)\,|\psi(t_0)\rangle \tag{1.11}$$

$$U(t, t_0) = exp\left(\frac{-iH(t - t_0)}{\hbar}\right) \tag{1.12}$$

$$H = \frac{\mathbf{p}^2}{2\mu} + V \tag{1.13}$$

The evolution of a physical system is thus for the most part determined by the potential. Given that the interaction inside a nucleus is largely described as being between nucleons, it is therefore not unexpected that a large effort in nuclear physics should involve an attempt to improve our knowledge of the internucleon potential.

The fact that the weak interaction violates parity is equivalent to the statement that V_{weak}, the potential for the weak interaction, does not commute with the parity operator:

$$[V_{weak}, \pi] \neq 0. \tag{1.14}$$

The fact that angular momentum is conserved requires for V_{weak} to be invariant with respect to an arbitrary rotation. As such, V_{weak} is a scalar operator and must therefore contain pseudoscalar terms, by the definition on page 5.

Due to the relative strengths of the weak and strong interactions, the weak Hamiltonian is often treated as a perturbation that mixes the parity eigenstates of the parity-conserving strong Hamiltonian H_0. An example is the case of a first order time-independent perturbation. Consider two nearly degenerate eigenstates $|\psi_+\rangle$ and $|\psi_-\rangle$ of H_0 with eigenvalues E_+ and E_- respectively. The difference (E_+ - E_-) is given by δE. Consider also that they have the same angular momentum quantum number. These states are mixed by V_{weak} to produce the following state:

$$|\phi\rangle = |\psi_+\rangle + \frac{\langle\psi_-|\, V_{weak}\, |\psi_+\rangle}{\delta E}\, |\psi_-\rangle\,. \tag{1.15}$$

It is assumed that other terms in the expansion correspond to wide enough energy spacings that they do not contribute significantly to the sum. Since V_{weak} does not commute with π, it is possible for the inner product of equation (1.15) to be nonzero, even if $|\psi_+\rangle$ and $|\psi_-\rangle$ have opposite parity. In such a case, $|\phi\rangle$ is of mixed parity.

The concepts mentioned in this section are discussed in more detail in popular quantum mechanics texts such as in references [3, 4, 5, 6].

1.5 Symmetries and the weak interaction

1.5.1 Parity violation and the weak interaction

The conservation and violation of symmetries has played a key role in the development of an understanding of subatomic physics. Of historical note is a puzzle relating to the existence of two particles, referred to at the time as the τ^+ and θ^+ mesons. These two particles were observed to have the same masses, lifetimes and electrical charges, and were known to be unstable by the weak interaction. However, given their decay products, and given conservation of angular momentum and conservation of parity, it would not have been possible for them to be the same particle.

In their celebrated paper of 1956 [7], T. D. Lee and C. N. Yang observed that parity

conservation in the weak interaction had been assumed from knowledge of the other interactions, but had not been independently verified. As a solution to the so-called τ-θ puzzle, they proposed several experiments that could be used to confirm whether or not parity was violated by the weak interaction. Included in their discussion was the observation that previous beta decay experiments could not be used to test parity conservation since all of the measurements that had been made were of observables that are invariant under a parity transformation. Only a measurement of a pseudoscalar observable would allow for a clear test of parity nonconservation.

In 1957, C. S. Wu et al. performed one of these experiments and thus provided the first unequivocal confirmation of parity violation [8]. C. S. Wu (who had been consulted by T. D. Lee on some experimental matters) and her collaborators measured a nonzero dot product between the average momentum of beta particles and the average spin of the ^{60}Co nuclei from which they were emitted.

It is now accepted that the τ^+ and θ^+ mesons are the same particle and are referred to as the K^+ meson. The decays that gave rise to the initial controversy are:

$$K^+ \rightarrow \pi^+ + \pi^0 \tag{1.16}$$

$$K^+ \rightarrow \pi^+ + \pi^0 + \pi^0 \tag{1.17}$$

$$K^+ \rightarrow \pi^+ + \pi^+ + \pi^- \tag{1.18}$$

Since pions are of negative intrinsic parity, and since all of the mesons shown in the above three reactions are of zero intrinsic angular momentum, the end product of reaction (1.16) must be of opposite parity from the end product of reactions (1.17) and (1.18).

1.5.2 A strong interaction context

The current theoretical framework of particle physics, the Standard Model, describes matter in terms of three *generations* of spin-$\frac{1}{2}$ particles (fermions). The three generations are similar in that they all comprise a total of two quarks and two leptons, but higher generations correspond to particles of higher mass that decay to lower-generation counterparts via the weak interaction.

Strongly interacting particles (hadrons) are composed of quarks. The six aforementioned types of quarks are distinguished by a label that is referred to as *flavor*. At low energies, the description of hadronic matter is typically limited to the three least massive quark flavors: the up (u), the down (d) and the strange (s). The quantum numbers relevant to these three quark flavors are *isospin* and *strangeness*, both of which are conserved by the strong interaction.

The introduction of isospin, or I, was motivated by the observation of symmetries associated with the strong interaction. It was noticed that some strongly-interacting particles could be separated into groups of similar mass and with incrementally varying electric charge. Examples are the neutron and proton; the π^+, π^0 and π^- mesons; and the Σ^+, Σ^0 and Σ^- baryons. Isospin is a quantity that was proposed as a method for labeling these groups, which are referred to as isospin multiplets.

It has also been observed that processes involving strongly-interacting particles sometimes proceed independently of which particle from an isospin multiplet is participating. As an example, consider s-wave nucleon-nucleon scattering. The two processes:

$$p + p \rightarrow d + \pi^+ \tag{1.19}$$

$$n + n \rightarrow d + \pi^- \tag{1.20}$$

are dominated by the strong interaction and proceed with equal probability. Another example is that of *mirror nuclei* (pairs of nuclei such as ${}^{13}_{7}\mathrm{N}$ and ${}^{13}_{6}\mathrm{C}$ that can be transformed into each other by exchanging all protons for all neutrons) that have energy spectra displaying states of the same angular momentum and parity at approximately the same energy.

The idea that the strong interaction is independent of any interchange of particles from the same multiplet is rejected, however, by the fact that a third scattering process:

$$p + n \rightarrow d + \pi^0 \tag{1.21}$$

proceeds with only half the probability of that corresponding to equations (1.19) and (1.20). A similar observation can be made of the fact that the np system has a bound state whereas the pp and nn systems have no bound state.

This situation is explained by treating isospin in a mathematically identical manner to angular momentum. Each isospin multiplet corresponds to a group of total isospin I, and each member of the multiplet corresponds to a projection I_3 of the isospin vector onto an axis in an abstract isospin space. The fact that these strongly bound states of the same I but different I_3 are almost degenerate in energy indicates that the strong interaction is invariant with respect to a rotation in isospin space. The strong interaction therefore conserves I and I_3 in the same way that it conserves angular momentum.

I is thus used to label the similarity of particles under the strong interaction, while their distinguishability is preserved by the use of I_3. The nucleon, as an isospin doublet, can combine in pairs to produce an isospin triplet (*nn*, *np* and *pp*), or an isospin singlet (*np*). Since empirically the deuteron exists as a spin singlet of even intrinsic parity, Fermi statistics requires that it exist as an isospin singlet. By rules of isospin conservation, and by knowledge of the appropriate Clebsch-Gordan coefficients, the relative cross sections associated with equations (1.19), (1.20) and (1.21) can thus be understood.

At the quark level, isospin conservation is understood as arising from the conservation of the total number of up quarks and the total number of down quarks. The similar masses of isospin multiplets is explained additionally in terms of the similar masses of the u and d quarks. The total number of strange quarks is referred to as *strangeness* or S. Quark flavor in general is conserved by the strong interaction so S must be unchanged during any strong interaction. Like parity, however, neither isospin nor strangeness are conserved by the weak interaction.

1.6 The hadronic weak interaction

1.6.1 *Classifications of the weak interaction*

The Standard Model describes the weak interaction between noncomposite fermions (leptons and quarks) in terms of the exchange of massive left-handed vector bosons: the W^+, W^- and Z^0 particles. The large masses of these exchange particles account for the small probability amplitudes associated with the weak interaction; their left-handed helicity accounts for the parity-violating nature of weak processes.

This model has been extensively verified by experiment. However, aspects of the weak interaction between composite hadrons (the hadronic weak interaction) remain to be understood. For example, the $\Delta \mathrm{I} = \frac{1}{2}$ rule, a selection rule that favors $\Delta \mathrm{I} = \frac{1}{2}$ channels over $\Delta \mathrm{I} = \frac{3}{2}$ channels in $\Delta S = 1$ hadronic decays, empirically exists but is of unknown dynamical origin (see for example p. 226 of reference [9]). Also, the potential that would be used to model weak interactions between composite hadrons has not been empirically quantified.

Figure 1.1 is intended as an illustration of common classifications that are made of the weak interaction. Of these classifications, the purely leptonic, semileptonic and $\Delta \mathrm{S} = 1$ hadronic interactions can be isolated by symmetry requirements as purely weak effects. However, there is nothing that would prevent flavor-conserving hadronic interactions ($\Delta S = 0$ in figure 1.1) such as $np \rightarrow np$ from passing through a purely strong channel.

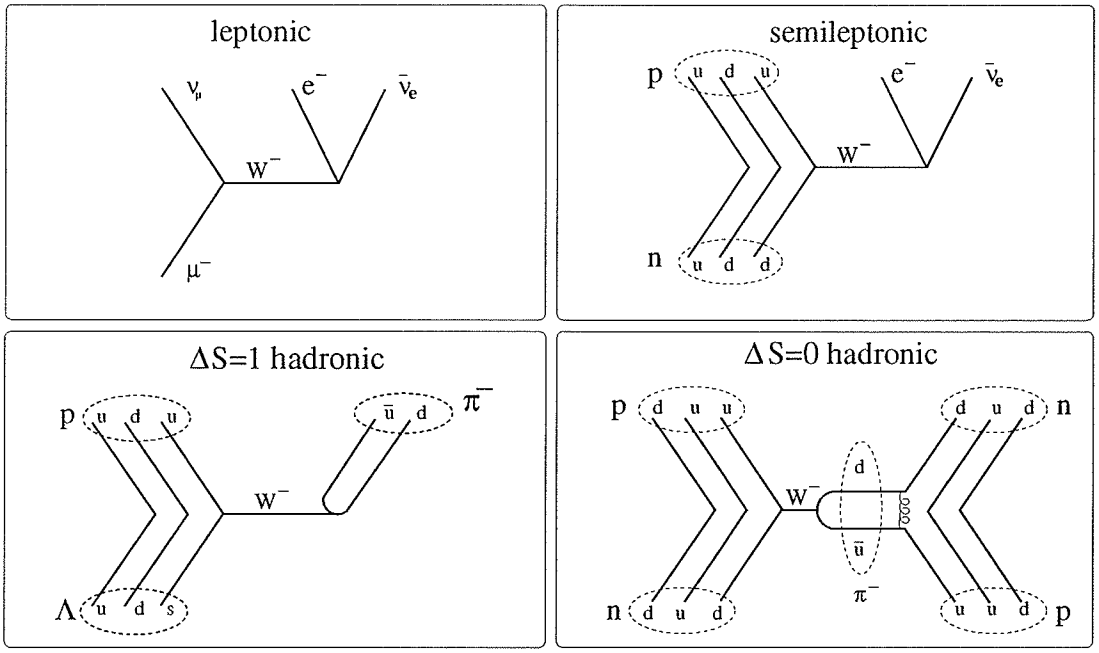

Figure 1.1: Various manifestations of the weak nuclear interaction. Shown are: 1) the purely leptonic decay of a muon: $\mu^- \rightarrow e^- \nu_\mu \bar{\nu}_e$; 2) the semileptonic beta decay of a neutron: $n \rightarrow p e^- \bar{\nu}_e$; 3) the strangeness-nonconserving purely hadronic decay of a Λ baryon: $\Lambda \rightarrow p\pi^-$; 4) strangeness-conserving purely hadronic neutron-proton scattering: $np \rightarrow np$.

Experimental studies of the flavor-conserving hadronic interactions are therefore hindered by the fact that strong couplings are several orders of magnitude greater than weak couplings. In the case of a purely hadronic flavor-conserving exchange, the weak component of the interaction remains detectable only due to its unique parity-violating signature. Due to the weaker nature of the weak interaction, a large portion of the experimental effort involves careful studies to eliminate systematic errors that could overshadow true parity-violating signals. Experimental studies are also limited by the fact that high flux sources are required in order to achieve the necessary precision. Theoretical studies on the other hand are hindered by the fact that calculations of strong interactions are difficult to perform reliably at low energies.

1.6.2 The meson exchange model of the hadronic weak interaction

Experimental searches for parity violation in the nucleon-nucleon (NN) interaction were begun in 1957 by Neil Tanner [10] who looked for parity-nonconserving transitions to the ground state of ^{16}O from a 340 keV resonance of $^{19}\mathrm{F}(p,\alpha)^{16}\mathrm{O}$. This transition would have passed via α emission from a 1^+ resonance in ^{20}Ne to the 0^+ ground state of ^{16}O. As such it is forbidden by parity conservation since the final system ($^{16}\mathrm{O}+\alpha$) would have orbital angular momentum $l=1$, and would thus be of negative parity. This transition was not observed.

In 1964, the first observation of parity violation inside the nucleus was reported. Applying the method of R. Haas et al. [11], but to a higher precision, Abov et al. [12] observed an asymmetry of $-(3.7\pm0.9)\times10^{-4}$ in the directional distribution of gamma quanta from polarized neutron capture on ^{113}Cd [2]. Parity violation in the NN interaction became more statistically convincing with the measurement provided by Lobashov et al. [13] in 1967. Lobashov's group measured the circular polarization $-(6\pm1)\times10^{-6}$ of gamma radiation from a 482 keV transition of unpolarized ^{181}Ta nuclei. For other early measurements of nuclear parity violation, and an early discussion of the theory, see reference [14]. More recent reviews on this subject are provided in references [15, 16, 17].

---

[2]This asymmetry is the same as that provided by a nonzero A_γ in equation (1.35).

A meson exchange model has been proposed as a description of the weak interaction between hadrons. In understanding this model, it should be considered that the weak vector bosons are limited by their large masses to a range that is two to three orders of magnitude smaller than the femtometer hard-core repulsion between nucleons. As a result, the component of the weak NN interaction that is due to direct W or Z exchange is essentially zero. In the hadronic weak interaction, the exchange still involves the $W^{\pm}$ and Z^0 particles, but at only one vertex. The interaction is instead modeled in terms of meson exchange, as illustrated in figure 1.2.

Despite their composite nature, mesons and nucleons are the degrees of freedom that are used when modeling intranuclear interactions, which are typically in the energy range of hundreds of MeV. This assertion that the physics be modeled in terms of mesons and nucleons is inspired by the theory of the strong interaction. The model for strong meson exchange between nucleons is widely confirmed (see for example [1]). The physics of the interaction is described by the potential which is given as a linear combination of terms, each term corresponding to a particular type of meson exchange.

The parity-violating NN interaction is expected to be mediated in a similar manner. In the model for weak exchange between nucleons, the $W^{\pm}$ or Z^0 convert into a light meson which couples strongly at the other vertex. The weak boson exchange is collapsed to a point and becomes a weak meson-nucleon vertex. This idea is illustrated in figure 1.2, which can be compared to the bottom right-hand diagram of figure 1.1.

An important trait of this model is that one of the vertices of the exchange is weak while the other vertex is strong. The couplings at the strong vertex have been determined experimentally from studies of meson exchange in the strong NN interaction. Due to the presence of the weak vertex, weak meson exchange does not conserve parity or isospin.

The potential V_{PNC} for weak meson exchange is described by the following linear combination of terms:

$$V_{PNC} = \sum_{\mu} \sum_{\Delta I} H_{\mu}^{\Delta I} V_{\mu}^{\Delta I}. \tag{1.22}$$

Each term corresponds to a meson μ and to an isospin exchange ΔI. The size of the contribution from each term is determined by the coupling constant that is represented by

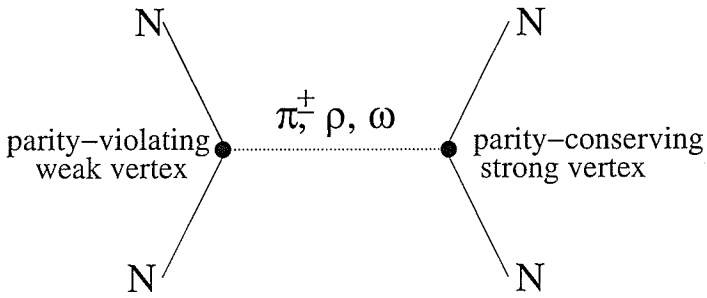

Figure 1.2: The meson exchange model of the hadronic weak interaction. In this model, the weak interaction between nucleons is mediated by the exchange of a meson. One of the meson-nucleon couplings is weak and therefore violates parity and isospin. The other coupling is strong.

$H_\mu^{\Delta I}$. The functional dependence of each term on dynamical variables is given by $V_\mu^{\Delta I}$, which is a function of space, spin and isospin. A benchmark theoretical prediction of the weak coupling constants for this meson-exchange potential has been provided by B. Desplanques, J. F. Donoghue and B. R. Holstein (DDH) [18, 19, 20].

A short-range internucleon repulsion has been interpreted from phase shift analysis of high energy nucleon-nucleon scattering experiments (see e.g. section 4.4 of [21]). As is embodied in the Yukawa formulation for an exchange potential, the range of a virtual exchange particle is determined by its mass, and decreases with increasing mass. The range of this short range repulsion corresponds to an exchange particle mass of about 800 MeV. Thus mesons of mass higher than 800 MeV are neglected in the DDH model. Barton's theorem [22] provides the assertion that neutral spin-zero meson exchange is forbidden by CP conservation. Thus, to the extent that CP conservation applies, mesons such as the π^0 and η can also be neglected.

The low mass mesons are shown in table 1.1. The mesons used in the DDH model are the π^+, π^-, ρ^+, ρ^0, ρ^- and ω mesons. Different projections of the same isospin multiplet do not contribute different terms to the potential: for example, the term for the π^- is not distinct

from the term for the π^+. Terms involving double meson exchange are neglected. The ρ mesons contribute possible isospin exchange of ΔI = 0,1 or 2. The ω mesons contribute possible isospin exchange of ΔI = 0 or 1. The $\pi^{\pm}$ mesons contribute possible isospin exchange of ΔI = 1. The general expression for the DDH potential then follows from equation (1.22) and is described by six separate couplings:

$$V_{PNC}^{DDH} = H_\pi^1 V_\pi^1 + H_\rho^0 V_\rho^0 + H_\rho^1 V_\rho^1 + H_\rho^2 V_\rho^2 + H_\omega^0 V_\omega^0 + H_\omega^1 V_\omega^1. \tag{1.23}$$

Quark constituents	$^1S_0$ state	$^3S_1$ state	Isospin
$\left\|u\bar{d}\right\rangle$	π^+ (140)	ρ^+ (769)	1
$\frac{1}{\sqrt{2}}\left(\left\|d\bar{d}\right\rangle - \left\|u\bar{u}\right\rangle\right)$	π^0 (135)	ρ^0 (769)	1
$\left\|\bar{u}d\right\rangle$	π^- (140)	ρ^- (769)	1
$\frac{1}{\sqrt{2}}\left(\left\|d\bar{d}\right\rangle + \left\|u\bar{u}\right\rangle\right)$	η (547)	ω (782)	0

Table 1.1: Low mass mesons. Masses are stated in parentheses to the nearest MeV/c^2. The π and ρ mesons are isospin triplets. The ω and η mesons are isospin singlets of zero charge. All of these mesons have negative intrinsic parity.

For the form of the $V_\mu^{\Delta I}$, see [18] or the review articles [15, 16]. The pion exchange potential, which is of particular relevance to the NPDGamma experiment, is given by:

$$V_\pi^1 = \frac{i}{m}\left[\vec{I}_1 \times \vec{I}_2\right]_z (\vec{\sigma}_1 + \vec{\sigma}_2)\cdot\left[\vec{p}, \frac{exp\left(-m_\pi r\right)}{4\pi r}\right], \tag{1.24}$$

where m is the nucleon mass, $\vec{I}$ is isospin, $\vec{\sigma}$ is spin and $\vec{p}$ is momentum associated with the relative coordinate $\vec{r} = \vec{r}_1 - \vec{r}_2$. The subscripts 1 and 2 are used to differentiate between the two nucleons, and the subscript z is used to indicate projection onto the third axis in isospin space.

It can be seen from equation (1.24) that V_π^1 is composed of terms that are proportional to $(\vec{\sigma}_1+\vec{\sigma}_2)\cdot\vec{r}$, where $(\vec{\sigma}_1+\vec{\sigma}_2)$ is an angular momentum and $\vec{r}$ is a displacement. These terms are therefore altered by a parity transformation. The factor $exp\left(-m_\pi r\right)/4\pi r$ is the Yukawa

potential that was first applied to describe the strong interaction. This factor determines the relationship between the range of the interaction and the mass of the exchange particle.

For each coupling constant, DDH have provided a reasonable range of possible values and their estimate of the most likely value. The reasonable range is designed to encompass all theoretical uncertainties so that future refinements will lead to results inside the range. These ranges and best values are shown in table 1.2. From table 1.2, it can be seen that considerable uncertainty exists in the DDH predictions, at 100 % or more of the best predicted values. An initiative is currently underway to determine these coupling constants, to provide experimental quantification of the model, and to allow for a better understanding of the model itself.

Coupling	Best Value	Reasonable Range
H_π^1	1.08	0.0 $\rightarrow$ 2.71
H_ρ^0	1.59	-1.59 $\rightarrow$ 4.26
H_ρ^1	0.03	0.0 $\rightarrow$ 0.053
H_ρ^2	1.33	-1.06 $\rightarrow$ 1.54
H_ω^0	0.80	-2.39 $\rightarrow$ 4.29
H_ω^1	0.48	0.32 $\rightarrow$ 0.80

Table 1.2: DDH predicted values of weak meson-nucleon couplings [18]. All numbers in this table are in units of 10^{-6}.

Of the mesons that contribute to the hadronic weak potential, the pion is of particular interest. Being the least massive of the mesons, the pion is responsible for the longest range component of the internucleon interaction. As such, it can be expected to provide the most important contribution to internucleon parity-violating effects.

The parity-violating observable to be measured by the NPDGamma experiment is referred to as A_γ and is calculated to be directly proportional to the weak πNN coupling H_π^1. The relationship shown in equation (1.25) is discussed in [15]. It is assumed that the $H_\mu^{\Delta I}$ lie within the DDH reasonable range so that couplings other than H_π^1 will contribute

negligibly to A_γ. Other calculations [23, 24] are consistent with this coefficient of H_π^1 and with the prediction that contributions from other mesons are small.

$$A_\gamma = -0.045(H_\pi^1 - 0.02H_\rho^1 + 0.02H_\omega^1 + 0.04H_\rho'^1) \tag{1.25}$$

1.7 *Parity-violating observables*

With the existence of parity violation in the weak interaction, nuclear states are not parity eigenstates. As was explained in section 1.4, a description of the parity mixing of strong eigenstates can be achieved using perturbation theory, with the extent of the parity mixing determined by the size of ϵ in equation (1.26). The value of ϵ can in turn be determined using matrix elements similar to the one shown in equation (1.15). Thus, ϵ can be expressed as a linear combination of the couplings $H_\mu^{\Delta I}$ as shown in equation (1.27). The coefficients $a_\mu^{\Delta I}$ are dependent on the nature of the unperturbed states and on the parity-violating potential [3].

$$|\phi\rangle = |\psi_+\rangle + \epsilon\,|\psi_-\rangle \tag{1.26}$$

$$\epsilon = \sum_{\Delta I}\sum_{\mu} a_\mu^{\Delta I} H_\mu^{\Delta I} \tag{1.27}$$

The expectation value $\langle A\rangle$ of the observable A is obtained by calculating a diagonal matrix element of the corresponding operator as shown in equation (1.28). A transition probability λ related to the transition operator T is obtained between initial and final states using the expression in equation (1.29). In the case of a potential that violates parity, it is possible for the states $|\phi\rangle$,$|\phi_1\rangle$,$|\phi_2\rangle$ and for the observable A or transition T to be of mixed parity.

$$\langle A\rangle = \langle\phi|\,A\,|\phi\rangle \tag{1.28}$$

$$\lambda = |\langle\phi_2|\,T\,|\phi_1\rangle|^2 \tag{1.29}$$

It is possible for the general observable A to be expressed as a sum of both parity-even and parity-odd terms as shown in equation (1.30). The expectation value of A can

[3] Although the concept of a parity-mixing amplitude that is proportional to a linear combination of the weak coupling constants still applies, it should be noted that equation (1.15) cannot literally be used for the *np* system, which has only one bound state.

then involve a term that is proportional to the weak mixing ϵ and that is thus a linear combination of the weak coupling constants. This is expressed in equation (1.31). As will be shown in section 1.9, a similar expression exists for the transition rate between states of mixed parity.

$$A = A_{even} + A_{odd} \tag{1.30}$$

$$\langle\phi| A |\phi\rangle = \langle\psi_+| A_{even} |\psi_+\rangle + 2\epsilon \mathrm{Re}\left\{\langle\psi_-| A_{odd} |\psi_+\rangle\right\} + O(\epsilon^2) \tag{1.31}$$

An initiative is currently underway to measure such parity-odd observables and thus to determine the weak meson-NN coupling constants in a variety of systems. Examples of such observables include: violation of parity selection rules (e.g. the previously mentioned work of Tanner [10]); a difference in cross-section of scattering by particles of opposite helicity (e.g. the helicity-dependent pp scattering experiment performed at TRIUMF [25]); linear momentum that is released preferentially parallel to an angular momentum (e.g. the NPDGamma experiment as will be discussed); angular momentum that is released preferentially parallel to a linear momentum (e.g. nonzero average helicity of radiation from an unpolarized source [26]); the generation of a rotation about an axis of translation (e.g. the rotation of a particle's spin about its linear momentum such as the neutron-^{4}He spin rotation experiment that is under development [27]); and parity-violating charge and current distributions (e.g. anapole moments and electric dipole moments).

Due to the relative size of the weak and strong couplings, ϵ is quite small compared to unity. Observation of the odd parity term in the presence of the even parity term is difficult. Given this situation, it can be beneficial to look for mechanisms that enhance parity-violating signals. These mechanisms often occur in many-body systems.

For example, in the case of gamma polarization from unpolarized ^{18}F, enhancement is achieved in part due to a pair of energy eigenstates with δE sufficiently small (see equation (1.15)). Measurements of the circular polarization of the 1.081 MeV γ emission from unpolarized ^{18}F are believed to provide a minimal dependence on nuclear models [28]. These measurements [26, 29] have yielded a null measurement of the pion coupling constant of $H_\pi^1 = (0.7 \pm 2.0) \times 10^{-7}$, considerably lower than the DDH best value.

Another example, measurement of the nonzero anapole moment of ^{133}Cs [30, 31], has

been interpreted to give a larger value of $H_\pi^1 = (2.26 \pm 0.50\ (\text{expt}) \pm 0.83\ (\text{theory})) \times 10^{-6}$. Unfortunately there is a difficulty due to uncertainties associated with many-body wavefunctions. Wilburn and Bowman [32] point out that the anapole moment interpretation may be flawed, and that the ^{133}Cs and ^{18}F measurements may be in agreement with each other. In any case, these analyses have pointed out a discrepancy that must be addressed.

Figure 1.3 shows a recent summary of current experimental knowledge of H_π^1, from reference [33]. A similar analysis can be found in reference [34]. In this figure, a linear combination of H_ρ^0 and H_ω^0 is expressed in terms of H_π^1. DDH best values are used for any couplings that are not shown in the plot. It should be visible from this plot that at present, significant uncertainty remains in the experimental determination of these coupling constants. This is in addition to the fact that the size of the DDH reasonable range (see table 1.2) allows for the plot to change significantly (see for example [32]).

1.8 The directional gamma asymmetry

Given the importance of H_π^1 to the understanding of nuclear weak interactions, and given the fact that the current experimental situation does not challenge or constrain the DDH model, it is necessary to resolve the H_π^1 dilemma by providing a precise measurement in a simple system. The simplest internucleon system possible is the two nucleon system. Due to the fact that the *pp* interaction is purely neutral current, pion exchange is excluded. It is therefore necessary to look in the *np* system.

The goal of the NPDGamma experiment is to measure the parity-violating directional gamma-ray asymmetry A_γ when a neutron and a proton fuse to form a deuteron. This asymmetry is measured relative to the direction of the neutron spin. A polarized neutron beam is therefore used. The reaction of interest is thus shown in equation (1.32). In addition to the fact that it is a two body system, *np* capture is also simplified by the fact that only one gamma-ray of unique energy is produced per capture.

$$\vec{n} + p \rightarrow d + \gamma \ \ (2.2\ \text{MeV}) \tag{1.32}$$

Let the angles θ_{sk} and ϕ_{sk} be defined in equations (1.33) and (1.34) where $\vec{k}_\gamma$ is the gamma-ray wave vector, $\vec{s}_n$ is the neutron spin, and $\vec{k}_n$ is the neutron wave vector. θ_{sk} is

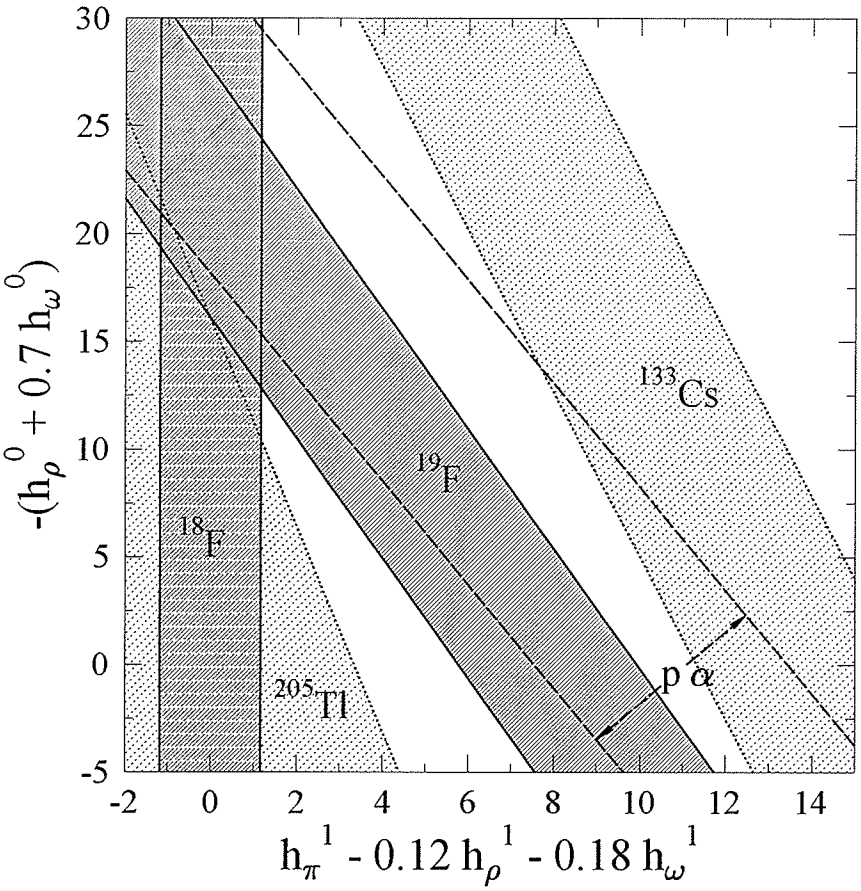

Figure 1.3: A summary of current experimental knowledge of H_π^1 [33]. Both axes display units of 10^{-7}. Shown are results from measurement of: the nuclear anapole moments of ^{205}Tl and ^{133}Cs; the helicity dependence of p-α scattering; the polarization of gamma radiation emitted from unpolarized excited states of ^{18}F; the directional asymmetry associated with radiative capture of polarized neutrons on ^{19}F. This plot uses a different naming convention: $H_\pi^1 = g_{\pi NN} h_\pi^1/\sqrt{32}$; $H_\rho^0 = -g_\rho h_\rho^0/2$; $H_\omega^0 = -g_\omega h_\omega^0/2$; $H_\rho^1 = -g_\rho h_\rho^1/2$; $H_\omega^1 = -g_\omega h_\omega^1/2$. The g_μ are the strong couplings at one vertex: $g_{\pi NN} = 13.45$; $g_\rho = 2.79$; $g_\omega = 8.37$ [15]. These plots can be compared to the DDH best predictions of $(h_\pi^1 - 0.12h_\rho^1 - 0.18h_\omega^1) = 4.8 \times 10^{-7}$ and $-(h_\rho^0 + 0.7h_\omega^0) = 13 \times 10^{-7}$. The DDH reasonable ranges allow $-16 < -(h_\rho^0 + 0.7h_\omega^0) < 38$ and $0.8 < (h_\pi^1 - 0.12h_\rho^1 - 0.18h_\omega^1) < 12$. There is considerable room for improvement on this current state of affairs.

a polar angle that is measured from the direction of $\vec{s}_n$ to the direction of $\vec{k}_\gamma$. ϕ_{sk} is an azimuthal angle that is measured about $\vec{k}_n$, from $\vec{s}_n$ to the component of $\vec{k}_\gamma$ that lies in the

plane perpendicular to $\vec{k}_n$, as shown in figure 1.5. A system using these two angles is not a polar coordinate system, since both angles are measured from the same vector, but is useful for a discussion of the gamma asymmetry that is observable in the NPDGamma apparatus.

Let $d\omega/d\Omega$, given in equation (1.35), be the probability per unit solid angle Ω for emission of a gamma-ray in the direction (θ_{sk}, ϕ_{sk}). A_γ is defined as the coefficient that determines the cosine dependence of $d\omega/d\Omega$ on θ_{sk}, and is illustrated in figure 1.4. Since $d\omega/d\Omega$ is an observable scalar quantity, and since $cos\,(\theta_{sk})$ is reversed by a parity transformation, it follows that a nonzero A_γ is parity-violating. An asymmetry A_{PC} that is proportional to $sin\,(\phi_{sk})$, and therefore parity-conserving, is also expected.

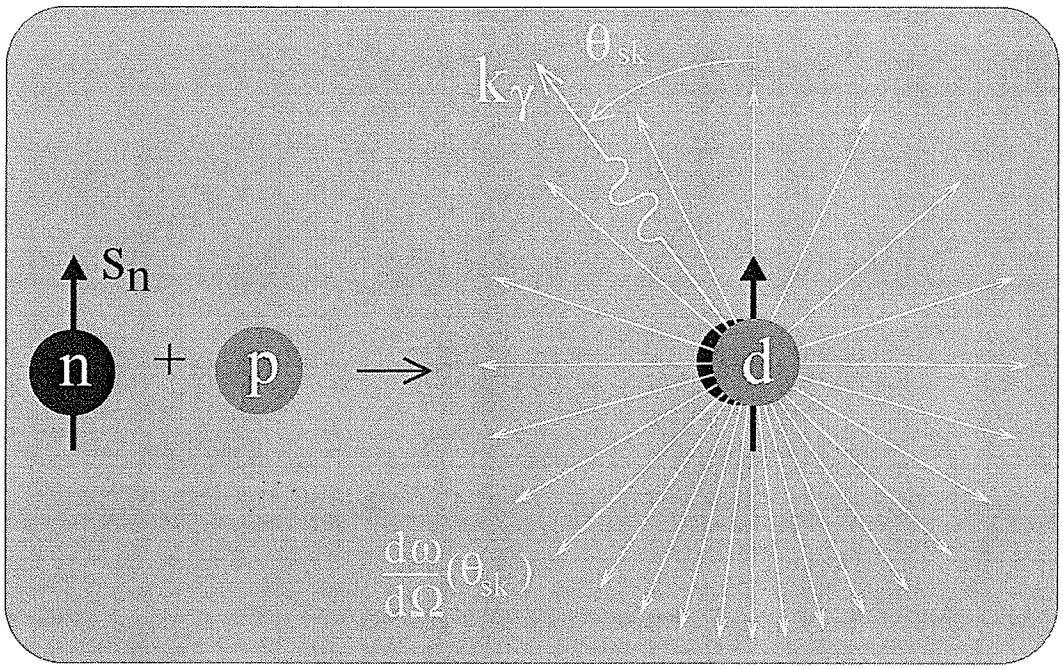

Figure 1.4: The distribution of gamma energy from the reaction $\overrightarrow{n} + p \rightarrow d + \gamma$ is to a large extent isotropic but is expected to have small directional asymmetries. These asymmetries are dependent on the polar angle θ_{sk} and on the azimuthal angle ϕ_{sk} which are illustrated in figure 1.5. A nonzero A_γ allows for a term in the expression for $d\omega/d\Omega$ that is proportional to the cosine of θ_{sk}. Such a term is parity-violating and is illustrated in this diagram. A parity-allowed asymmetry that is proportional to $sin(\phi_{sk})$ (not illustrated in this diagram) is also expected. The method for measuring A_γ is illustrated in figure 2.6.

$$cos(\theta_{sk}) = \frac{\vec{s}_n \cdot \vec{k}_\gamma}{|\vec{s}_n||\vec{k}_\gamma|} \tag{1.33}$$

$$sin(\phi_{sk}) = \frac{\vec{s}_n \cdot \left(\vec{k}_\gamma \times \vec{k}_n\right)}{|\vec{s}_n||\vec{k}_\gamma \times \vec{k}_n|} \tag{1.34}$$

$$\frac{d\omega}{d\Omega}(\theta_{sk}, \phi_{sk}) \propto 1 + A_\gamma cos(\theta_{sk}) + A_{PC} sin(\phi_{sk}) \tag{1.35}$$

In terms of its effect on known physical interactions, a parity transformation is equivalent to a reversal of any one of the Cartesian coordinates on its own. This can be explained by the fact that either one of these two types of coordinate reversal can be transformed into the other by including rotation and translation operations, and by the fact that all known interactions are invariant with respect to rotation or translation.

It is impractical to produce an actual parity transformation of an entire apparatus. In order to understand the transformation that is carried out in the NPDGamma experiment, define the direction of beam momentum as forwards and then consider that the beam is polarized perpendicular to this, in the up-down direction. A reversal is performed of the beam polarization. Since the target is left-right symmetric, this reversal is equivalent to an interchange of left and right (single coordinate reversal) of the incident beam and target. Hence, it is equivalent to a parity transformation.

If a left-right reversal of the gamma momentum is taken into account, as shown in the top half of figure 1.6, then $sin(\phi_{sk})$ is conserved while $cos(\theta_{sk})$ is reversed. However, a polarization reversal is not accompanied by a left-right reversal of the gamma detection apparatus. As such, a left-right reversal of the gamma momentum is not taken into account. A reversal of both $sin\,(\phi_{sk})$ and $cos(\theta_{sk})$ therefore occurs, as shown in the bottom half of figure 1.6. Since A_{PC} is expected to be of approximately the same size as A_γ, an important part of the experiment involves accurate positioning of the beam and detectors in order to separate these two components of the asymmetry.

Due to the nonzero extent of the gamma detectors and target along the beam axis, it would be possible for the gamma signal to contain an admixture of a forward-backward asymmetry, if such an asymmetry were to exist. However, a forward-backward asymmetry

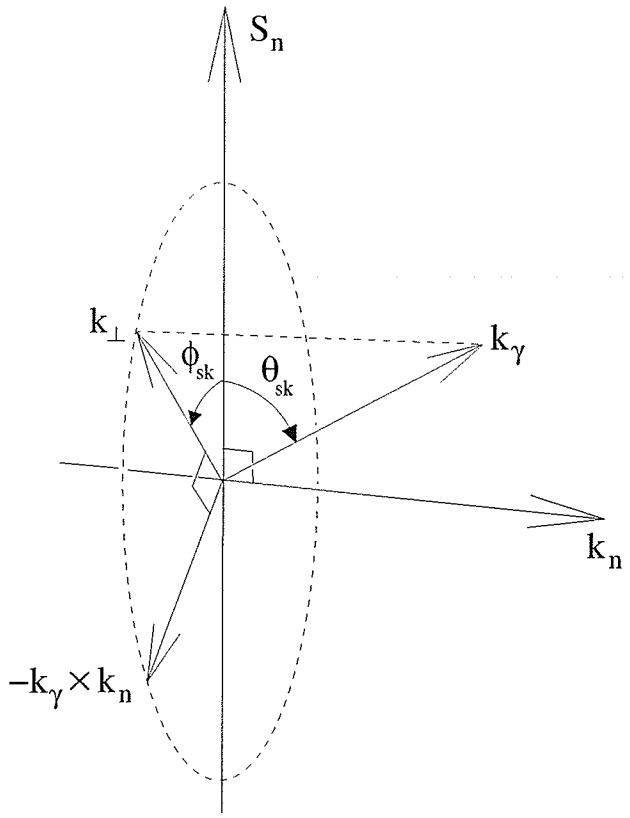

Figure 1.5: A visualisation of the angles θ_{sk} and ϕ_{sk} that are defined in equations (1.33) and (1.34). $\vec{k}_\gamma$ and $\vec{k}_n$ are the gamma and neutron wavevectors respectively. $\vec{s}_n$ is the neutron spin which, for the NPDGamma experiment, is aligned perpendicular to $\vec{k}_n$. $\vec{k}_\perp$ is the projection of $\vec{k}_\gamma$ that lies in the plane perpendicular to $\vec{k}_n$. θ_{sk} is a polar angle that is measured from $\vec{s}_n$ to $\vec{k}_\gamma$. ϕ_{sk} is an azimuthal angle that is measured, about $\vec{k}_n$, from $\vec{s}_n$ to $\vec{k}_\perp$. The magnitudes of the vectors in this diagram are not drawn to scale.

must be dependent on odd powers of $sin\,(\theta_{sk})$, and would therefore be parity-conserving. Since the forward-backward orientation of both the beam and apparatus is maintained during the measurement, no forward-backward asymmetry can be observed.

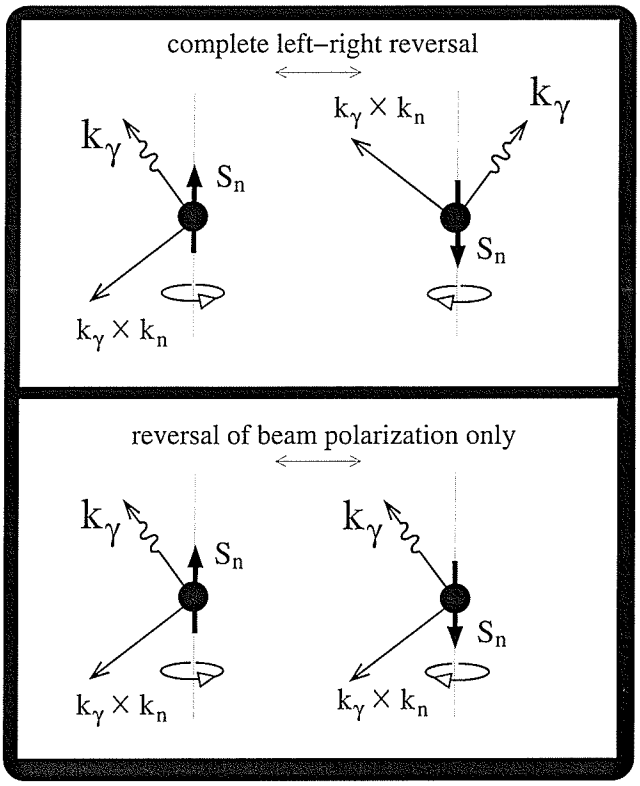

Figure 1.6: If translation and rotation invariance are assumed, then a parity transformation is equivalent to the reversal of one Cartesian coordinate. An example is the left-right reversal of the NPDGamma reaction that is shown in the top half of this diagram. The momentum of the neutron, and possibly a component of the gamma momentum, is perpendicular to the page and therefore unaffected by a left-right reversal. The proton has no average momentum or average spin so is not shown. The recoil of the deuteron and the angular momentum of the final system are redundant so are also not shown. The bottom half of the diagram shows a spin reversal that is not accompanied by a left-right reversal of the gamma momentum. A complete left-right reversal alters the sign of $\vec{s}_n \cdot \vec{k}_\gamma$ but leaves $\vec{s}_n \cdot (\vec{k}_\gamma \times \vec{k}_n)$ unchanged. A polarization reversal that is not accompanied by a left-right reversal of gamma momentum alters the sign of both.

1.9 The origin of A_γ

The total internal angular momentum J of the bound deuteron is known to exist in a triplet state ($J = 1$). It is also known from experiment that the total coupled spin S of the two

nucleons exists in a triplet state ($S = 1$). The spin singlet state is empirically unbound. Angular momentum associated with the relative motion of the two nucleons exists primarily as $L = 0$ with a 4 % admixture of $L = 2$. The total internal parity of the deuteron is positive.

For the purpose of what follows, a discussion on the origin of A_γ, the presence of the $L = 2$ state is ignored. The bound deuteron is therefore approximated as the $|^{2S+1}L_J\rangle = |^3S_1\rangle$ state that is shown in bold on the righthand side of figure 1.7.

The unbound *np* wavefunction can be expanded in terms of spherical harmonics. To a good approximation, at meV energies (the relevant energies for this experiment), the unbound system is represented purely as an S wave. The two S states that are in bold on the lefthand side of figure 1.7 are therefore the dominant states of the initial *np* system.

The existence of parity-violating observables indicates admixtures of states that are of opposite parity. For this discussion, only the lowest order admixtures are considered. The existence of P states (negative parity) with $J = 1$ are therefore hypothesized for the bound deuteron. Similarly, P states that conserve J are expected to mix with the S states of the unbound system. The isospin of each state is determined by considering that the wave function of the two-fermion system must be antisymmetric with respect to particle interchange.

The formation of a bound deuteron from an unbound *np* system occurs as a result of an electromagnetic transition that can be expanded in terms of multipole moments oriented about the axis of polarization. The allowed components of the transition are shown in figure 1.7.

In determining which transitions should be shown in figure 1.7, the usual angular momentum and parity selection rules for electromagnetic transitions apply (see for example section 10.4 of [21]). Thus E1 transitions occur between states of opposite parity, M1 transitions occur between states of the same parity, and both carry an orbital angular momentum quantum number of $L = 1$. Only the lowest order transitions that will allow for parity violation are considered. Quadrupole transitions are therefore not considered.

The following isospin selection rules for a self-conjugate ($N = Z$) nucleus also prove to be useful: $\Delta I = 0$ E1 transitions and $\Delta I = 0$ M1 transitions can be ignored (see for

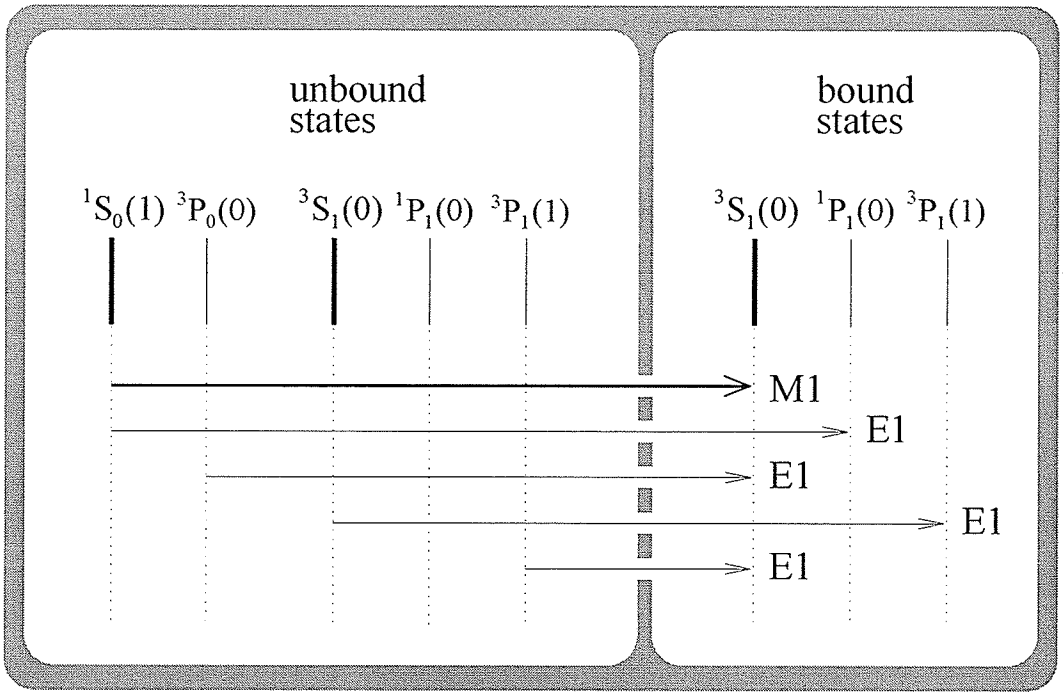

Figure 1.7: A simplified level diagram of the *np* system, from chapter 10 of reference [35]. States are shown using the convention $^{2S+1}L_J(I)$ where S is total spin, L is orbital angular momentum, J is total angular momentum and I is isospin. The bound state of the deuteron before parity mixing is considered to be purely $^3S_1$. The $^3S_0$ state is empirically unbound. The continuum states that are most present for a low energy system are the S waves. Higher order partial waves are ignored. Parity mixing allows for: admixtures of states with opposite parity but the same total angular momentum; and interference between transitions of opposite parity. It is the interference between E_1 and M_1 transitions that gives rise to the asymmetry A_γ.

example chapter 4 of [36]). As a result of this rule, and since only dipole transitions are being considered, transitions between states of the same isospin can be neglected.

The M1 transitions that can occur between the $|^3P_1\rangle$ and $|^1P_1\rangle$ states are also ignored. Owing to the fact that they are magnetic transitions, they are of smaller amplitude than electric transitions of the same order. Furthermore, since they arise from parity mixing, they are of less importance than the primary M1 transition. The transitions that are considered

as contributing to A_γ are thus the ones shown in figure 1.7.

The only transition between the unmixed states (the bold states in figure 1.7) that survives the aforementioned cuts is $\left|^1S_0\right\rangle \overset{M1}{\rightarrow} \left|^3S_1\right\rangle$ which, since it is an M1 transition, is of positive parity. All of the other transitions are E1 and are therefore of negative parity. It is the presence of interference between transitions of opposite parity that supports this phenomenological explanation of the origin of A_γ.

Consider a general parity mixing $|S\rangle \leftrightarrow |P\rangle$ that occurs both in the initial and final states. Isospin mixing is not explicitly represented, since it does not affect the qualitative result of this discussion. For the same reason, it is also not explicitly stated that there are in reality two different initial states. The states $|\phi_i\rangle$ and $|\phi_f\rangle$ are therefore represented as in equations (1.36) and (1.37). The transition that connects the initial and final states is given by T in equation (1.38). The parity reflection of T is shown in equation (1.39).

$$|\phi_i\rangle = |S_i\rangle + \epsilon_i |P_i\rangle \tag{1.36}$$

$$|\phi_f\rangle = |S_f\rangle + \epsilon_f |P_f\rangle \tag{1.37}$$

$$T = M1 + E1 \tag{1.38}$$

$$\pi^\dagger T \pi = M1 - E1 \tag{1.39}$$

The probability of the transition T can be determined by equation (1.29). If a nonzero difference exists between the rate of T and the rate of its parity reversal $\pi^\dagger T \pi$, then an instance of parity violation can be observed. To first order in ϵ, and neglecting $\langle E1\rangle$ terms relative to $\langle M1\rangle$ terms (since the M1 transition is dominantly present and the E1 terms are only allowed by parity violation), this difference can be used to represent A_γ:

$$\begin{aligned} A_\gamma cos\left(\theta_{sk}\right) &\propto \frac{|\langle\phi_i|\, T\, |\phi_f\rangle|^2 - \left|\langle\phi_i|\, \pi^\dagger T \pi\, |\phi_f\rangle\right|^2}{|\langle\phi_i|\, T\, |\phi_f\rangle|^2 + \left|\langle\phi_i|\, \pi^\dagger T \pi\, |\phi_f\rangle\right|^2} \\ &\propto \frac{\mathrm{Re}\left\{\langle S_i|\, M1\, |S_f\rangle \left(\epsilon_i \langle S_f|\, E1\, |P_i\rangle + \epsilon_f^* \langle P_f|\, E1\, |S_i\rangle\right)\right\}}{|\langle S_i|\, M1\, |S_f\rangle|^2}. \end{aligned} \tag{1.40}$$

With knowledge of the wave functions and the potential, it is possible to predict the size of A_γ (as relevant to equation (1.35)) from an expression that is similar to that given in

equation (1.40). A more rigorous explanation of the origin of A_γ, which includes a derivation of the angular dependence of the asymmetry, is available in chapter 2 of reference [37] or in reference [24].

Based on the DDH best value for H_π^1, the expected size of the asymmetry is $A_\gamma = -5 \times 10^{-8}$ [38, 24]. The NPDGamma collaboration proposes to make a measurement of A_γ with a statistics-limited uncertainty of $\pm 10^{-8}$. As a result of the difficulty involved in such a measurement, and the requirement for high counting statistics, only one previous measurement has been made. This measurement, which was carried out in 1977, yielded the null result $A_\gamma = (6 \pm 21) \times 10^{-8}$ [39]. The goal of the NPDGamma experiment is to improve this uncertainty by a factor of twenty, to within a factor of five smaller than the best estimate of the asymmetry's size.

Chapter 2

THE NPDGAMMA EXPERIMENTAL APPARATUS

2.1 Requirements for a measurement of A_γ

In order to achieve the goal of a statistics-limited measurement of A_γ at the 10^{-8} level, particular attention must be paid to maximizing the gamma-ray signal and to eliminating false systematic effects. A brief list of the requirements for such an apparatus follows.

1. It is important to perform the measurement of A_γ in a reasonable amount of time. Since the uncertainty of a statistics-limited measurement is proportional to $1/\sqrt{N}$ where N is the number of detected events, it is therefore important to maximize the rate of gamma detection. This leads to the requirement that the experiment be run at a high flux neutron source. Since pulse counting is not possible at such a high detection rate, the detection instruments must be designed to operate in current mode.

2. Since A_γ is measured relative to the direction of neutron spin, the neutron beam must be polarized. The beam polarization must be reliably measurable at all times, and the method of polarization must not introduce false signals elsewhere in the apparatus. With these considerations taken care of, the requirement for high beam polarization must be balanced with the requirement for minimizing beam losses during the polarization process.

3. The polarization of the beam must be maintained until the neutrons are absorbed in the target. It must also be possible to verify that the polarization is not being lost prior to the *np* capture event.

4. There must be an abundant source of unpolarized protons that absorbs the majority of the neutron beam, that does not produce excessive scattering of the beam, and that does not depolarize the beam before it is absorbed.

5. There must be a gamma detection apparatus that efficiently absorbs incident gamma radiation, that occupies a large solid angle about the target so as to take advantage of the available signal, and that is preferably sensitive to the directional distribution of the asymmetry.

6. As a result of the requirement to separate the left-right signal from the up-down signal, it must be possible to align the beam momentum and polarization axes with the axes of the gamma detection apparatus.

7. Every aspect of the apparatus must be designed with the consideration for eliminating false asymmetries. False asymmetries are effects that give rise to a beam polarization-correlated up-down variation in the gamma detector signal and that are not proportional to A_γ. Since false asymmetries are not restricted by parity conservation, they are easier to produce than A_γ and are present unless very carefully eliminated. In order that the measurement of A_γ be statistics limited, false asymmetries must be maintained well below the target 10^{-8} level of precision.

Figure 2.1 shows a schematic of the NPDGamma experimental apparatus which was designed to satisfy these criteria. The apparatus has undergone construction and commissioning (i.e. preparation for data-taking) at the Los Alamos Neutron Science Center (LANSCE). In fall of 2000, an engineering run was carried out during which most major components of the apparatus were tested. This run is discussed in reference [40] which also serves as a good explanation of the workings of many aspects of the experiment. The data that are discussed in this thesis were obtained during a commissioning run that was carried out in February and March of 2004. At the time of writing of this thesis, all components of the NPDGamma apparatus and beamline had been commissioned, except for the liquid hydrogen target which was still undergoing construction and safety approval. The elements of the NPDGamma experimental layout will now be discussed in turn.

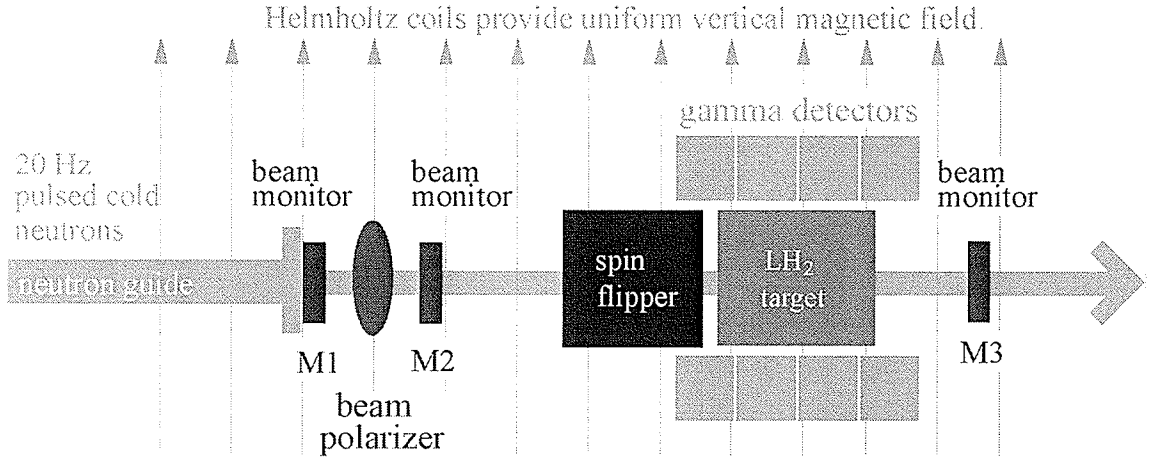

Figure 2.1: A schematic of the NPDGamma apparatus. The beam monitor upstream of the polarizer is mounted directly onto the beam guide. The three beam monitors typically go by the names M1, M2 and M3 that are determined by their position in the apparatus. The distance from M1 to M3 is approximately two meters. During the commissioning run in 2004, the liquid hydrogen target was not present (but was sometimes replaced by other capture targets), and M3 was not always present. Not shown in this diagram is the detector stand and associated motion control electronics which allow for the array of gamma detectors to be positioned relative to the liquid hydrogen target.

2.2 *Flight Path 12 at the Lujan Center*

The neutrons for the NPDGamma reaction (equation (1.32)) are provided by a pulsed cold neutron beam from the LANSCE spallation neutron source that is located at the Manuel Lujan Jr. Neutron Scattering Center. An 800 MeV proton beam is produced by the LANSCE linac. This proton beam is compressed into 250 ns wide 20 Hz pulses by the Proton Storage Ring. The pulsed proton beam is directed to a tungsten spallation target at the Lujan Center. High energy neutrons from the spallation reaction are slowed to meV energies as they are scattered from a liquid hydrogen moderator.

A new flight path at the Lujan Center (Flight Path 12 or FP12) was designed and built by the NPDGamma collaboration and will be dedicated to fundamental nuclear physics research. This development involved the installation of a new neutron guide, the installation of a frame overlap chopper, the construction of an experimental cave, and installation of the experimental apparatus in the cave. FP12 has the highest intensity pulsed cold neutron beam in the world. At 100 μA proton current, neutrons enter the apparatus at a peak rate of 3×10^{10} n/s at an energy of 9 meV (3 Å) (from a Monte Carlo calculation [41] based on the measurement discussed in [42]).

A large part of the construction of the flight path involved the installation of a neutron guide. Perpendicular to its axis, the inner surface of the neutron guide is 9.5 cm $\times$ 9.5 cm square. The inner walls of the guide are coated with layers of ^{58}Ni and ^{47}Ti, allowing for more reflection than that afforded by nickel-only guides. The end flange of the neutron guide is at 21.00 m from the moderator.

Approximately halfway between the moderator and the end of the neutron guide there is a frame overlap chopper. The chopper has two blades coated in Gd_2O_3. The gadolinium coating ensures that the blades are opaque to low energy neutrons. The blades are rotated so that a blade passes through the beam once per pulse. The phase of the blades is chosen with the purpose of eliminating slow neutrons that would overlap with higher energy neutrons from the following pulse. The purpose of the chopper is thus to allow for a one-to-one correspondence between time of flight and neutron energy. For an illustration of the time of flight spectrum from the FP12 neutron guide, see figure 3.17.

A measurement of the brightness and energy spectrum of the moderator as seen by Flight Path 12 is discussed in reference [42]. This measurement was made during the beamline construction, when the first 8 meters of the neutron guide were in place. A measurement was also made in February 2004, after the construction of the experimental cave and installation of the apparatus had been completed (See section 3.2.1 of [37]). The two measurements were found to be consistent.

2.3 The magnetic holding field

An important observation from figure 2.1 is that the entire apparatus is immersed in a uniform vertical static magnetic field of approximately 10 G. This field is provided by four horizontal Helmholtz coils, of equal vertical spacing, which surround the apparatus in a racetrack shape. For this reason, they are sometimes referred to as racetrack coils. This field is important in holding the polarization of the neutron beam, and is also essential in the operation of the spin flipper and of the polarizer. The spin flipper and polarizer were designed to not require their own static magnetic fields for the purpose of avoiding static field gradients. Such gradients, if larger than a few mG/cm, would result in a false measurement of A_γ due to spin-dependent Stern-Gerlach steering of the beam. The gradients have been measured to be less than or close to 1 mG/cm along the length of the beam [43].

2.4 The beam monitors and beam flux

The first component of the apparatus that the beam sees after entering the experimental cave is a beam monitor. The beam monitors are parallel plate ionization chambers that contain a mixture of ^{3}He, ^{4}He and N_2 gases. They efficiently convert low energy neutrons into energetic charged particles by making use of the 764 keV of kinetic energy that is released during the reaction $n + {}^3He \rightarrow {}^1H + {}^3H$. They have been demonstrated to work reliably as low-noise current mode detectors. They are also straightforward to use and maintain and do not create any noise or background for the other components of the apparatus.

During data-taking, the beam monitors are positioned directly in the beam. A photograph of one of the beam monitors that was taken during installation of the apparatus into

the experimental cave is shown in figure 2.2.

Figure 2.2: A photograph of a beam monitor mounted on the end flange of the neutron guide, before most of the apparatus had been installed in the experimental cave. The aluminum box with a circular cover contains the preamplifier. The standing frame that is downstream of the monitor is used to support the beam polarizer. The black slab that sits on this frame is polyethylene with boron added, to prevent scattered neutrons from continuing farther downstream. Seen running immediately above and below the neutron guide are two of the magnetic holding field coils. The monitor shown in this photograph is M1 (see figure 2.1).

The monitors are useful since, for a given neutron energy, they provide a signal that is proportional to the instantaneous rate of neutrons incident. In this thesis, this quantity is referred to as *flux*. Unfortunately the term *flux* has multiple uses and can sometimes give rise to confusion. In this thesis, the quantity that is of relevance is the instantaneous rate of neutrons passing a point in the beam, measured for example in neutrons per second. If the term *flux* is used, it is therefore this quantity that is being referred to.

Figure 2.3 shows the signal from the preamplifier of M1 as a function of time for three

beam pulses. The time of flight dependence of the signal is visible. The shape of the waveform is determined by the time of flight dependence of the incident neutron rate; and by the intrinsic gain of the monitor, which also depends on time of flight.

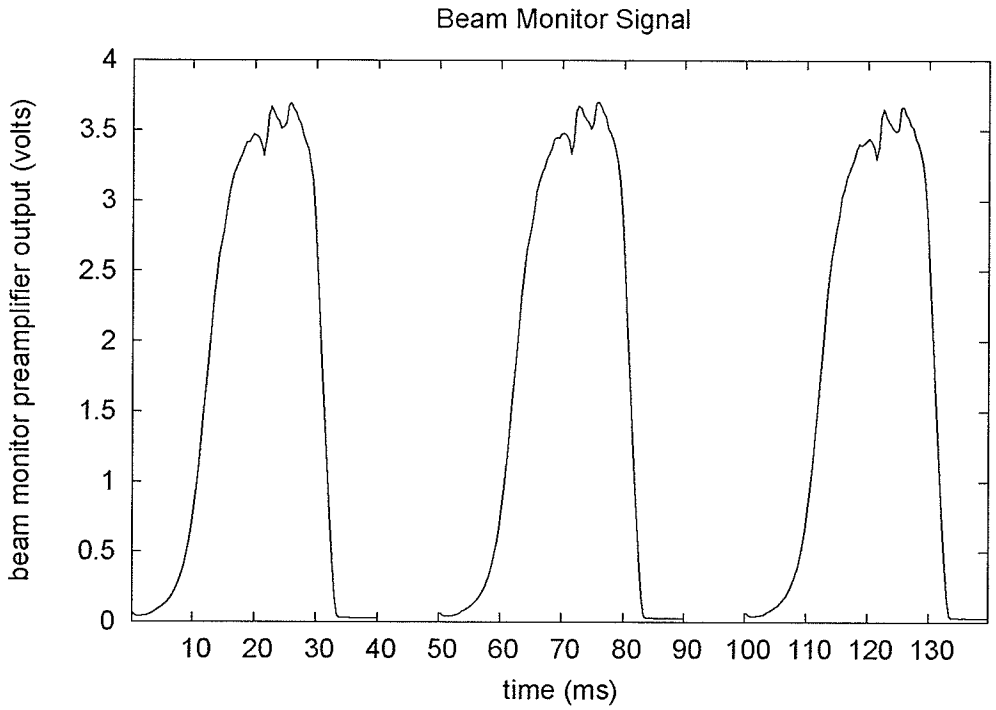

Figure 2.3: The beam monitor signal as a function of time for the first three beam pulses of data run 4364. In this plot, a new pulse begins at 0, 50 and 100 ms. Time of flight is the time measured from the beginning of a beam pulse. The frame overlap chopper can be seen to be cutting through the beam at around 30 ms time of flight. The use of the frame overlap chopper allows for a one-to-one correspondence to exist between time of flight and neutron energy. The dips in the signal near the peak occur as a result of enhanced attenuation of the beam from Bragg scattering that occurs due to the presence of aluminum in the flight path.

The frame overlap chopper allows for a correspondence between time of flight and neutron energy. This corresponence is very important to most of the analysis that uses the beam monitors. The beam monitors are the main area of focus of this thesis and are discussed in more detail in later chapters.

2.5 The polarized ^{3}He neutron spin filter

Shortly after entering the NPDGamma experimental cave, the neutron beam is polarized by transmission through a glass cell containing nuclear-spin-polarized ^{3}He. The very large spin-dependent cross section for absorption of neutrons by ^{3}He allows these cells to preferentially transmit neutrons of one spin state.

The ^{3}He cells also contain small amounts of rubidium and nitrogen. The cells are maintained at a temperature (typically $\approx$ 160 $^\circ$ C) for the rubidium to take vapour form. The rubidium vapour is polarized by spin-exchange optical pumping using circularly-polarized laser light. Polarization is transferred from the Rb atomic states to the ^{3}He nuclei via a hyperfine interaction. The ^{3}He is polarized vertically so that the neutrons are also polarized vertically, parallel to the beam axis.

^{3}He cells are ideal in minimizing backgound since the n + ^{3}He reaction does not create any products that would contribute to background signals elsewhere in the apparatus. Furthermore, ^{3}He polarizers need not contain any magnetic materials, and the holding field that is used to maintain ^{3}He polarization is the same as the field that is present throughout the apparatus. It is thus possible to maintain the uniformity of the static holding field at a level that does not introduce a false asymmetry.

From the point of view of analysis, ^{3}He cells are convenient since the polarization of the ^{3}He and of the neutron beam can both be determined using transmission measurements of the cell (see chapter 4). Such transmission measurements are made using the beam monitors. The use of ^{3}He cells also allows for polarimetry measurements to be made continually, in simultaneity with the gamma asymmetry measurements. ^{3}He spin filters and beam monitor polarimetry are discussed in more detail in chapter 4, and transmission measurements are discussed in section 3.1.8. A photograph of the part of the apparatus that is relevant to beam polarization and polarimetry is shown in figure 2.4. A photograph of the polarizer cell is shown in figure 2.5.

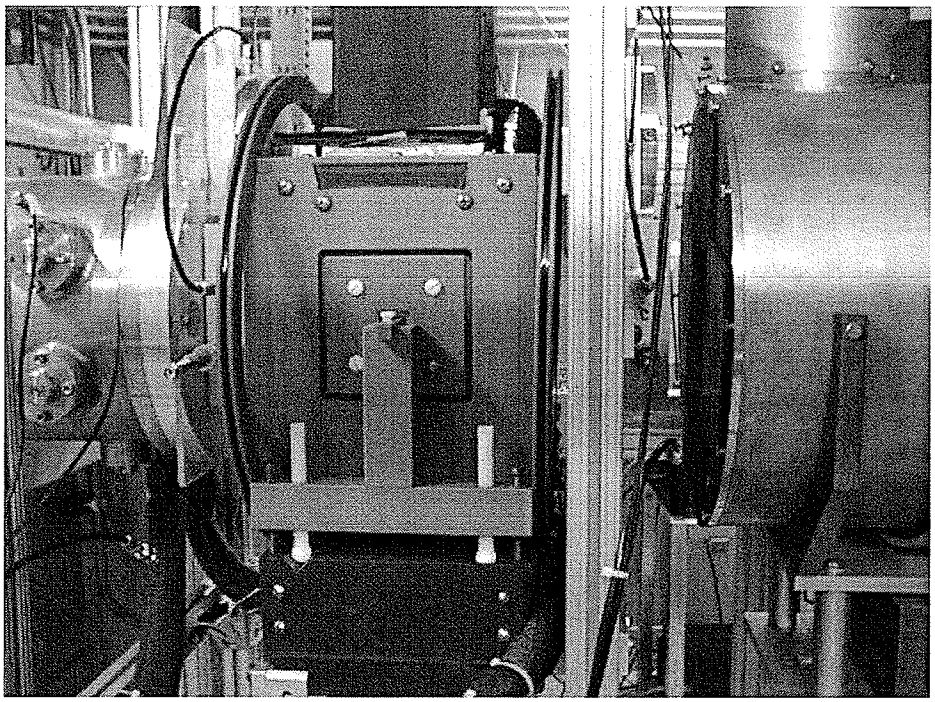

Figure 2.4: A photograph of the apparatus upstream of the target. At the left is the beam guide. Mounted on the end flange of the beam guide is M1 which can only barely be seen. The box downstream of M1 is the polarizer oven which contains the ^{3}He cell. The two round coils upstream and downstream of the oven are not typically used, but allow for an occasional reversal of ^{3}He polarization using magnetic resonance. Circularly polarized laser light is carried by optical fibers through the black pipe that is shown above the oven, and through a similar pipe that is located below the oven. M2 can be seen mounted on the frame immediately downstream of the polarizer oven. Downstream of M2 is the spin flipper which is cylindrical and concentric with the beam (The spin flipper is discussed on p. 43). On top of the spin flipper, in an aluminum case, is the spin flipper dummy load. The section of the apparatus that is shown in this photograph occupies a bit less than a meter along the length of the beam. This photograph can be compared to the one in figure 2.2.

2.6 The para-hydrogen target

The protons for the $\vec{n} + p \rightarrow d + \gamma$ reaction will be provided by a liquid para-hydrogen target. The liquid hydrogen will be contained in a 30 cm diameter $\times$ 30 cm long cylinder that will be located coaxially with the neutron beam.

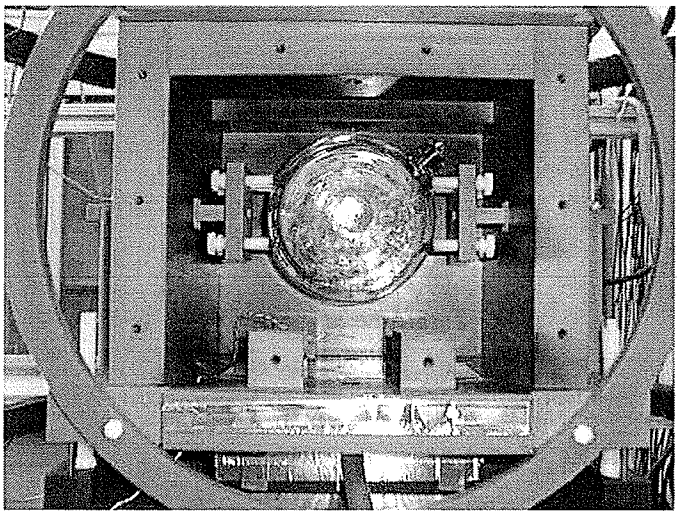

Figure 2.5: A photograph of the polarizer cell and the interior of the polarizer oven. For this photograph, one of the walls of the oven was removed to obtain a view of the cell down the axis of the beam. This photograph was taken before the polarizer was transported to the beamline. A small coil around the pinchoff of the cell, which is located at the 1:30 position in this photograph, allows for NMR measurements to be used to measure ^{3}He polarization.

Molecular hydrogen may exist in two nuclear spin states. Ortho-hydrogen (aligned nuclear spins) exists at 15 meV higher energy than para-hydrogen (antialigned nuclear spins). Neutrons of less than 15 meV energy remain polarized in para-hydrogen, but neutrons with greater energy than this tend to depolarize by scattering. Neutrons of any energy tend to depolarize from scattering in ortho-hydrogen. As such it is necessary to have a target that is composed primarily of para-hydrogen, and to conduct asymmetry measurements with neutrons of less than 15 meV energy.

For the purposes of NPDGamma, liquid hydrogen in equilibrium has a tolerable presence of ortho-hydrogen. However, it is necessary to verify that the ortho-hydrogen content is being kept low. Since ortho- and para-hydrogen have significantly different neutron cross-sections, this objective can be achieved by monitoring the transmission of neutrons through the target. The purpose of M3 (see figure 2.1) will be to monitor this transmission.

2.7 *The gamma detector array*

The gamma asymmetries are measured using an array of four rings of CsI(Tl) scintillators, with 12 scintillators per ring [44]. The detector rings are concentric with the beam and with the liquid hydrogen target. All four rings together encompass a solid angle of nearly 3π about the liquid hydrogen vessel.

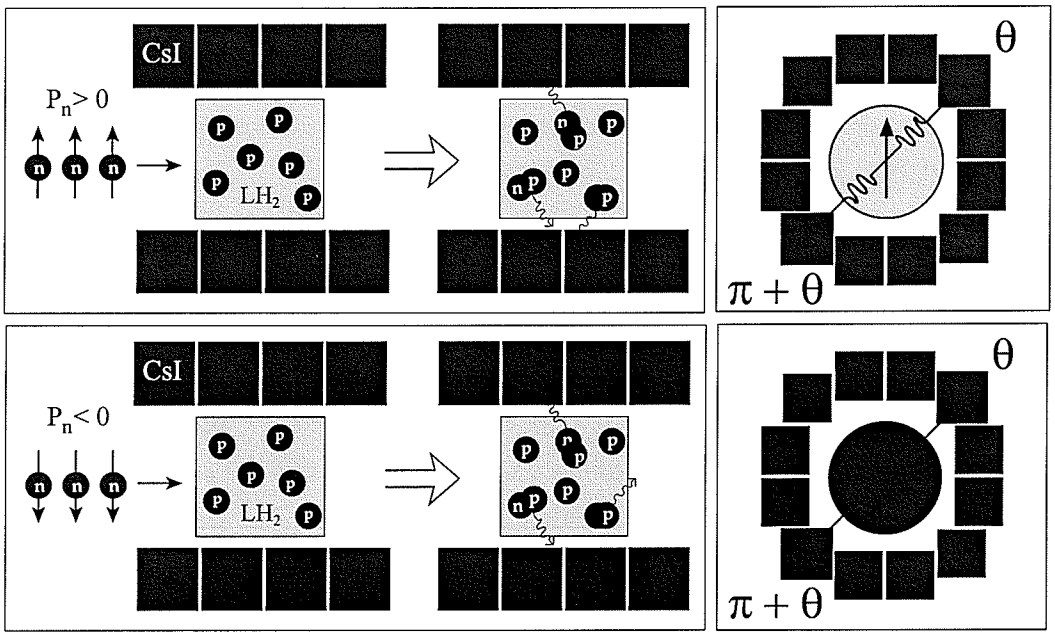

Figure 2.6: A schematic of an A_γ measurement. Each detector ring is composed of detectors measuring 15 cm × 15 cm × 15 cm and the LH_2 vessel is 30 cm long. Due to the cylindrical symmetry of the observable and of the apparatus, θ is an azimuthal angle. Due to the finite extent of the target and detectors, the weighted contribution of θ to each detector must be considered. Note that since θ remains fixed despite a change in the beam polarization, θ is different from ϕ_{sk} that is defined in equation (1.33). Also, a polar angle must be used to take into account a small effect arising from the fact that not all gammas travel perpendicular to the beam direction.

Each detector consists of a 15 cm wide scintillator cube. Due to the practical difficulties of manufacturing complete cubes of that size, each detector in fact contains two separate 15 cm × 15 cm × 7.5 cm crystals. Each pair of crystals is separately housed in a hermetically

sealed case of teflon and 1 mm thick aluminum.

Each scintillator cube is optically coupled to a vacuum photodiode and amplified using a low noise solid state preamplifier [45]. Each photodiode is powered by its own pair of 45 V batteries. This amplification method was chosen since it is negligibly affected by spin-correlated magnetic field interference from the spin flipper (as opposed to photomultiplier tubes which are strongly affected by variations in magnetic fields).

Beam pulses are 50 ms long. The signals from the preamplifiers are digitized by 16 bit ADCs, summed over each of 100 $\times$ 0.4 ms long time bins (there is a 10 ms break during data taking at the end of each pulse), and stored in a binary data file. Before digitization, one average signal and 12 difference signals are produced per ring. The average signal is the average voltage out of the 12 detectors in the ring and the difference signal is the difference between each detector's signal and the average. This method is used since: 1) the dynamic range of the ADCs is limited; and 2) the asymmetric component of the gamma distribution is much smaller than the isotropic component. Separate digitization of the difference and sum signals therefore prevents the parity-violating signal from being lost in the bit noise of the ADCs. To benefit from using this method, it is necessary to ensure that all of the detector gains of one ring are of similar size.

2.8 Measurement of the gamma asymmetry

A schematic of the method for performing a gamma asymmetry measurement is shown in figure 2.6. Consider first the signal in one detector of interest. The angle of a given detector does not change during a spin reversal. This new angle is referred to as θ and should be distinguished from the angles θ_{sk} and ϕ_{sk} that were introduced in section 1.8. θ is an azimuthal angle that is measured from a fixed direction parallel or antiparallel to the beam polarization, as shown in figure 2.6. θ is measured in the same direction about the beam momentum as ϕ_{sk}.

When considering the method of an asymmetry measurement, the lone neutron of equation (1.35) is replaced by a beam. Assume a detector of sufficently small volume that its spatial extent can be ignored. Furthermore, assume that the solid angle subtended by the

detector about the target is well defined. Only gamma rays that travel perpendicular to the momentum of the beam will be considered.

Let n_+ denote the number of neutrons with spins that are initially oriented in the direction $\theta = 0$. Let n_- denote the number of neutrons with spins that are initially oriented in the direction $\theta = \pi$. After some time, the orientation of all neutron spins is reversed, along with the role of the n_+ and n_- labels. Since a perfect polarization reversal is assumed, both n_+ and n_- remain constant despite the reversal. A label P is used to record the orientation of the neutrons such that $P =\uparrow$ before the reversal (when n_+ neutrons are in the $\theta = 0$ direction) and $P =\downarrow$ after the reversal (when n_+ neutrons are in the $\theta = \pi$ direction).

The gamma current in a detector is a linear sum of two currents originating separately from the n_+ and n_- populations. This sum is determined by: the number of captured neutrons that occupy the two populations; by P; and by the location of the detector. Since for this discussion $\vec{k}_\gamma \perp \vec{k}_n$, replacing θ_{sk} by ϕ_{sk} has no effect on $\frac{d\omega}{d\Omega}(\theta_{sk}, \phi_{sk})$, as can be verified by referring to equations (1.33), (1.34) and (1.35). Therefore, $\frac{d\omega}{d\Omega}$ need only be a function of ϕ_{sk}.

If $P =\uparrow$, the voltage signal out of a detector located at θ is therefore given by equation (2.1), as follows from the definition of $\frac{d\omega}{d\Omega}$. $g\{\theta\}$ is a constant of proportionality between incident gamma rate and output voltage, and is unique to the detector that is located at θ. $\delta\Omega$ is the solid angle that the detector subtends about the target. From figure 2.6, it can be seen that the signal entering a detector will change with spin reversal as determined by the transformation $(\phi_{sk} = \theta) \rightarrow (\phi_{sk} = \theta + \pi)$. If $P =\downarrow$, the voltage signal out of the detector located at θ is therefore given by equation (2.2).

$$N(n_+, n_-, \uparrow, \theta) = g\{\theta\}\left[n_+\frac{d\omega}{d\Omega}(\theta) + n_-\frac{d\omega}{d\Omega}(\theta + \pi)\right]\delta\Omega \tag{2.1}$$

$$N(n_+, n_-, \downarrow, \theta) = g\{\theta\}\left[n_+\frac{d\omega}{d\Omega}(\theta + \pi) + n_-\frac{d\omega}{d\Omega}(\theta)\right]\delta\Omega \tag{2.2}$$

An asymmetry measurement is performed using one detector located at θ and another located at $\theta + \pi$, and by performing the measurement that is stated on the lefthand side of equation (2.3). P_n is the beam polarization before a spin reversal and is defined in equation (2.4). By knowing the angle associated with each detector, a measurement of A_γ can be

extracted.

$$\frac{[N(\uparrow,\theta) - N(\uparrow,\theta+\pi)] + [N(\downarrow,\theta+\pi) - N(\downarrow,\theta)]}{[N(\uparrow,\theta) + N(\uparrow,\theta+\pi)] + [N(\downarrow,\theta+\pi) + N(\downarrow,\theta)]} = P_n \left(A_\gamma cos\theta + A_{PC} sin\theta\right) \tag{2.3}$$

$$P_n = \frac{n_+ - n_-}{n_+ + n_-} \tag{2.4}$$

In principle, it would be possible to measure A_γ using a single pair of detectors located at $sin\theta = 0$ without a spin reversal. However, since $g\{\theta\}$ and $g\{\theta+\pi\}$ cannot be matched at the level of precision required, pulse by pulse polarization reversals are performed to allow for comparison of gamma rate in the same detector. Both detectors are still used, however, in order to take advantage of the full solid angle available. As a polarization reversal is not 100 % efficient (see section 2.11), it is the average value of P_n that is relevant to equation (2.3).

It is also possible that the detector gains or the beam flux may change between polarization reversals. In order to account for such drifts that would cause an otherwise constant signal to vary linearly or quadratically in time, each individual asymmetry measurement uses a total of eight pulses, with P varying per pulse according to the sequence $\uparrow\downarrow\downarrow\uparrow\downarrow\uparrow\uparrow\downarrow$. Each pair of square brackets in equation (2.3) then corresponds to a sum over four pulses, rather than to one pulse. Variations with other time dependences will average to zero provided that they are not correlated with the beam polarization. Gamma asymmetry analysis is explained in more detail in reference [37].

2.9 The spin filter figure of merit

The figure of merit of a spin filter is a measure of its effect on the statistical uncertainty of the gamma asymmetry measurement. This consideration arises from the fact that in order to polarize the beam to make the asymmetry detectable, a spin filter must absorb part of the beam, thus diminishing the statistical power of the measurement. An explanation of the determination of this figure of merit follows.

The measurement of a gamma asymmetry A is carried out by first performing several individual measurements of a raw asymmetry A_{raw}. These individual measurements are

used to fill a histogram that is fit to a statistical distribution. For an infinitely precise measurement (an infinitely narrow distribution or an infinite number of histogrammed events), the mean of that distribution corresponds to the true value of the raw asymmetry.

Ignoring other effects that add independently (i.e. in quadrature) to the effect from statistics, the uncertainty in the measurement of the raw asymmetry is determined by the width of the parent distribution and by the number of events N that are used to fill the histogram. This is expressed more precisely in equation (2.5) where δ is used to denote the uncertainty in the mean of the distribution and σ is used to denote the standard deviation.

$$\delta_{Araw} = \frac{\sigma_{Araw}}{\sqrt{N}} \tag{2.5}$$

As stated in equation 2.6, A is related to A_{raw} by a proportionality constant C with $|C| < 1$:

$$A = CA_{raw}. \tag{2.6}$$

C is dependent on energy, but constant time of flight is considered here, so this energy dependence is ignored.

Since only the statistical uncertainty is currently being addressed, the relationship of equation (2.6) leads directly to :

$$\frac{\delta_A}{A} = \frac{\delta_{A_{raw}}}{A_{raw}}. \tag{2.7}$$

Incorporation of equation (2.5) leads to the determination that δ_A is inversely proportional to the product $C\sqrt{N}$:

$$\delta_A = \frac{1}{C}\left(\frac{\sigma_{Araw}}{\sqrt{N}}\right). \tag{2.8}$$

For a fixed running time, the number of events N recorded in the detectors is proportional to the flux of the beam entering the target. For constant beam flux, N is therefore proportional to the transmission of the beam to the target. Referring to equation (2.3), it can be seen that C is just the beam polarization where $A = A_\gamma cos\theta + A_{PC} sin\theta$.

It follows that, at a given time of flight, a minimum statistical uncertainty will be achieved by a maximum value of $P_n\sqrt{T_n}$, where T_n is the transmission of the neutrons through the polarizer. Since NPDGamma deals with a range of neutron energies, and since

$P_n\sqrt{T_n}$ is a function of neutron energy, this quantity must be integrated over the appropriate time of flight range.

For a given achievable ^{3}He polarization, maximizing $P_n\sqrt{T_n}$ corresponds to determining an appropriate ^{3}He content (according to the theory that is developed in section 4.1). For the beam polarizations that are relevant to the NPDGamma experiment, a ^{3}He thickness of approximately 4 atm·cm is appropriate (see p. 21 of [46]).

2.10 The spin flipper

The spin reversals that were discussed in section 2.8 are achieved using a magnetic resonance spin flipper. The spin flipper is a 30 cm long × 30 cm diameter solenoid that is mounted upstream onto the frame of the detector array and placed coaxially with the beam. Current is directed through the solenoid in order to reverse the polarization of the beam. When the polarization is to remain unchanged, the same current is directed to a dummy coil that mimics the coil of the solenoid, to prevent spin-correlated interference in the associated electronics. The solenoid is surrounded by a 40 cm diameter × 40 cm long aluminum shielding. The purpose of the shielding and dummy coil is to prevent spin-correlated interference in the detectors and associated electronics.

The spin flipper functions by magnetic spin resonance. Spin resonance is possible as a result of the fact that a linear relationship exists between the neutron spin $\vec{s}_n$ and the neutron magnetic moment $\vec{\mu}$. The proportionality constant is referred to as γ and is expressed in terms of known constants in equation (2.9). The constants are $g = -3.82$ and $\mu_N = 3.15 \times 10^{-8}$ eV/T.

$$\vec{\mu} = \gamma\vec{s} = g\frac{\mu_N}{\hbar}\vec{s} \tag{2.9}$$

For the purposes of this derivation (which is adapted from [3]), the vertical holding field, given by:

$$\vec{\mathbf{B}}_\mathbf{0} = B_0\hat{\mathbf{z}} \tag{2.10}$$

is taken to be in the z direction.

A torque $\vec{\tau} = \vec{\mu} \times \vec{\mathbf{B}}_\mathbf{0}$ causes the neutron spin to precess about $\vec{B}_0$ with the Larmor

frequency ω_0, which is given by:

$$\omega_0 = -\gamma B_0. \tag{2.11}$$

The precession occurs in a direction that is determined by $\vec{\tau} = d\vec{s}/dt$ where $\vec{s}$ in this case is the spin expectation value (or it is the spin operator in the Heisenberg representation). If $B_0 > 0$, the neutron will precess in a counterclockwise direction (as seen looking from the $+z$ direction).

An oscillating magnetic field $\vec{\mathbf{B}}_\mathbf{1} = B_1 cos\omega t\hat{\mathbf{x}}$ is provided in the x direction by the solenoid. This field can be represented as the following superposition of two counterrotating fields:

$$\vec{\mathbf{B}}_\mathbf{1} = \frac{B_1}{2}\left(cos\omega t\hat{\mathbf{x}} + sin\omega t\hat{\mathbf{y}}\right) + \frac{B_1}{2}\left(cos\omega t\hat{\mathbf{x}} - sin\omega t\hat{\mathbf{y}}\right). \tag{2.12}$$

Near resonance ($\omega \approx \omega_0$), and if $B_0 \gg B_1$, the effect of the clockwise field is negligible but the effect of the counterclockwise field remains. This can be visualized by considering that the spin precesses in phase with the counterclockwise field and sees the rapidly alternating clockwise field average to zero. For practical purposes, the net magnetic field can therefore be represented as:

$$\vec{\mathbf{B}} = \vec{\mathbf{B}}_\mathbf{0} + \vec{\mathbf{B}}_\mathbf{1} \approx B_0\hat{\mathbf{z}} + \frac{B_1}{2}\left(cos\omega t\hat{\mathbf{x}} + sin\omega t\hat{\mathbf{y}}\right). \tag{2.13}$$

The Hamiltonian of this system is thus given by

$$H = -\vec{\mu}\cdot\vec{\mathbf{B}} = -\mu(B_0\sigma_z + \frac{B_1}{2}\left\{cos\omega t\sigma_x + sin\omega t\sigma_y\right\}) \tag{2.14}$$

where $\sigma_{x,y,z}$ are the x,y and z coordinates of the vector operator $\vec{\sigma}$=$(2/\hbar)\vec{s}$. Due to the fact that this Hamitonian is not static, it is possible for transitions to occur between states.

The neutron's time-dependent spin wavefunction can be represented (using the Schrödinger picture) as an arbitrary linear combination of its two time-independent eigenstates of s_z. This is expressed in equation (2.15) where $e^{\mp i\omega t}\alpha_\pm$ are conveniently represented time-dependent probability amplitudes.

$$|\psi(t)\rangle = e^{-i\omega t}\alpha_+(t)\,|+\rangle + e^{+i\omega t}\alpha_-(t)\,|-\rangle \tag{2.15}$$

Schrödinger's equation:

$$i\hbar\frac{\partial}{\partial t}|\psi(t)\rangle = H\,|\psi(t)\rangle, \tag{2.16}$$

which governs the time evolution of a quantum system, produces a pair of coupled linear differential equations:

$$i\frac{d}{dt}\alpha_{\pm} = \mp\frac{\omega-\omega_0}{2}\alpha_{\pm} + \frac{\omega_1}{2}\alpha_{\mp}, \tag{2.17}$$

where

$$\omega_1 = -\gamma\frac{B_1}{2}. \tag{2.18}$$

This result can be verified by expressing the $\sigma_{x,y}$ in terms of raising and lowering operators (which are explained in popular quantum mechanics textbooks).

Now performing the time derivative of equation (2.17) and reusing equation (2.17) to eliminate occurrences of $\frac{d}{dt}\alpha_{\pm}$, the result is:

$$\frac{d^2}{dt}\alpha_{\pm} + \left(\frac{\Omega}{2}\right)^2\alpha_{\pm} = 0, \tag{2.19}$$

where the frequency Ω is defined by:

$$\Omega^2 \equiv (\omega-\omega_0)^2 + \omega_1^2. \tag{2.20}$$

The general solution to equation (2.19) is:

$$\alpha_{\pm} = A_{\pm}sin\left(\frac{\Omega}{2}t\right) + B_{\pm}cos\left(\frac{\Omega}{2}t\right) \tag{2.21}$$

where $A_{\pm}$ and $B_{\pm}$ are arbitrary and independent of time. If the condition $|\psi(0)\rangle = |+\rangle$ is imposed, equations (2.17) and (2.21) can be used to derive Rabi's formula:

$$|\langle -|\psi(t)\rangle|^2 = \left[\left(\frac{\omega_1}{\Omega}\right)sin\left(\frac{\Omega}{2}t\right)\right]^2. \tag{2.22}$$

It follows that to produce a full polarization reversal, such that $|\langle -|\psi(t)\rangle|^2 = 1$, it is necessary to tune the applied frequency f of the oscillating field to be equal to the frequency of precession about the holding field. After a time t has passed, a full reversal will occur if $B_1 = -2\pi/\gamma t$ is satisfied. If the solenoid has length l, the distance from the source to the solenoid is L, and the time of flight of the neutron is T, it follows that the time spent in the solenoid by the neutron is $t = (l/L)T$. The amplitude of the oscillating field must therefore be ramped inversely with time of flight. These conditions for a full polarization reversal are

summarized as:

$$f = \frac{|\gamma|}{2\pi} B_0 \tag{2.23}$$

$$B_1 = \left(\frac{2\pi L}{|\gamma|\, l}\right) \frac{1}{T} \tag{2.24}$$

For NPDGamma, B_0 is approximately 10 G, L is approximately 22 m, l is 30 cm, and B_1 is ramped for times between 4 and 40 ms.

2.11 The analyzer cell

The spin flipper does not reverse beam polarization with 100 % efficiency. The reasons for this include: 1) the oscillating field is not at all locations perpendicular to the holding field; 2) The magnitude of the oscillating field varies with the distance from the axis of the solenoid; 3) the magnitude of the oscillating field varies with time, even for a given neutron; 4) the holding field is not perfectly uniform; and 5) the parameters on the righthand side of equations (2.23) and (2.24) are known to finite precision.

It is in fact the *integral* of the oscillating amplitude over the neutron's trajectory that must be ramped with time, and so it is in principle possible to correct partly for the nonuniformity of the field magnitude. However, the imperfections cannot be corrected for completely. The polarization is therefore reversed, as in equation (2.25), by a multiplicative factor $-R$ that is slightly greater than -1. R has been measured previously by the NPDGamma collaboration to be 0.98 ± 0.02 [40].

$$P_n \rightarrow -RP_n \qquad (R \lesssim 1) \tag{2.25}$$

The efficiency of the spin flipper is measured with the use of a second polarized ^{3}He cell that is referred to as the analyzer cell. In this case no capture target is used, and the analyzer cell is placed between the spin flipper and M3 (see figure 2.1). The transmission of the analyzer cell is measured while the spin flipper is turned on and off (as for regular gamma asymmetry data taking). Applying the theory that is developed in section 4.1, the efficiency R can be determined. In order to do so, precise knowledge of the ^{3}He content of the analyzer and polarizer cells is required. The transmission of intervening materials such

as the cell walls must be known, and materials with time of flight-dependent cross sections that mimic the presence of ^{3}He should be avoided.

Chapter 3

THE BEAM MONITORS AS FLUX MONITORS

3.1 Background on the NPDGamma beam monitors

3.1.1 The role of the beam monitors

The beam monitors play a key role in the NPDGamma experiment by monitoring beam flux throughout the apparatus. The importance of beam flux (as defined on p. 33) — to the measurement of beam polarization; to the measurement of spin flip efficiency; and to the monitoring of the ortho- to para-hydrogen ratio in the liquid hydrogen target — was discussed in chapter 2. A brief introduction to the construction and use of the beam monitors was also given in section 2.4.

A new generation of fundamental physics experiments is being made possible by the development of high flux pulsed neutron sources such as the Spallation Neutron Source that is currently under construction at Oak Ridge in Tennessee (see, for example, [47, 48]). Many such experiments will likely be similar to NPDGamma in that they will be high precision measurements of parity-violating observables. As such they will have a similar requirement for high counting statistics and will therefore be run in current mode. It is also likely that reliable monitoring of beam flux throughout the apparatus will play an essential role in these experiments. A detailed study of the NPDGamma beam monitors is therefore beneficial not only to NPDGamma but also to future neutron physics experiments that may incorporate a similar class of beam monitors.

3.1.2 The $n + {}^3He$ reaction

The beam monitors make use of the interaction between neutrons and ^{3}He, which is well understood. A review of studies done on the $n + {}^3$He interaction can be found in the series

of articles *Energy levels of light nuclei A = 4*, of which the most recent edition is given in reference [49]. An important aspect of this reaction is that, for eV energies and lower, the (n, p) cross section strongly dominates. For the purposes of this thesis, this interaction can be considered as passing exclusively through this channel which is given by:

$$n + {}^3\mathrm{He} \rightarrow {}^1\mathrm{H} + {}^3\mathrm{H} + 764\ \mathrm{keV\ (KE)}. \tag{3.1}$$

This reaction has a very large cross section as a result of a 500 keV wide 0^+ resonance that exists in the ^{4}He system at 20.2 MeV above the 0^+ ground state (source: evaluated nuclear structure data from [50]). Note that a separated neutron and ^{3}He nucleus at rest exist at 20.6 MeV above the ^{4}He ground state (source: atomic mass data from [21]). Since no intermediate nuclear levels exist, and since $0^+ \rightarrow 0^+$ transitions involving the emission of a single gamma-ray are disallowed, gamma transitions can be ignored. Given the end products, the 764 keV is not sufficient for it to be released in any form other than kinetic energy.

Measurements of the total $n + {}^3\mathrm{He}$ cross section have given results that show a very clean $1/v$ dependence (v here is neutron speed), as is characteristic of an absorption cross section. The most recent measurement of the total n + ^{3}He cross section was done at energies between 0.1 eV and 400 eV and is given in reference [51]. The result is stated here in barns (1 b = 10^{-28} m^2) as a function of energy:

$$(\sigma/\mathrm{b}) = \frac{849.77 \pm 0.14 \pm 1.02}{\sqrt{E/\mathrm{eV}}} - (1.253 \pm 0.00^{+0.008}_{-0.049}). \tag{3.2}$$

The first uncertainty is statistical, the second systematic.

Another measurement, which was done at energies between 0.3 meV and 11 eV, yielded the result $\sigma_{\mathrm{total}} = 5327^{+10}_{-9}$ b at 2200 m/s. Despite having been done over different energy ranges, these two measurements agree. The continuity of the $1/v$ dependence over a range of neutron energies is verified by analysis in this thesis (see section 4.3.3).

At a pulsed cold neutron source, equation (3.2) can be rewritten in terms of time of flight t and distance from the source L as:

$$(\sigma/\mathrm{b}) = (11750 \pm 20) \left[\frac{t/\mathrm{ms}}{L/\mathrm{m}}\right]. \tag{3.3}$$

In analysis discussed in this thesis, the uncertainty in equation (3.3) can be ignored.

Measurements of the n + ^{3}He elastic cross-section have given results of about 3.3 b (independent of energy) [52, 53]. The cross section of the (n, γ) channel has been measured to be only 54 ± 6 μb [54].

3.1.3 The construction of the beam monitors

NPDGamma has a total of at least five beam monitors. They were manufactured by LND Inc [55]. Four of these five monitors were designed specifically for the NPDGamma Experiment. One of the four is a prototype that was tested in the fall of 2001 [56] and that has since been kept on hand as a spare. The successful testing of this prototype led to an order for three more monitors of the same construction. These three are the monitors that are routinely used in the experiment and that are referred to as M1, M2 and M3 (see figure 2.1). They are visibly distinguishable from the prototype since they do not have the refilling valve that the prototype has. Although these three are outwardly identical to each other, they contain different gas mixtures and can be distinguished by the serial numbers that are printed on their cases. Figure 3.1 shows a photograph of one of these three most commonly used NPDGamma beam monitors.

The fifth monitor is one that was used in previous experiments and is smaller in size than the other four. This monitor is referred to here as the TRIPLE monitor since it was used in the TRIPLE experiment. Apart from the fact that it is smaller in size and contains only ^{3}He gas, it is of similar construction to the other four. The exact amount of aluminum that it contains is not known. Some details on the TRIPLE monitor can be found in reference [57].

The drawings that were used by LND Inc. in the construction of the prototype NPDGamma monitor are shown in figure 3.2. A cross-sectional view of a chamber from the side (top drawing in figure 3.2) shows that a neutron passing through the monitor will see five layers of aluminum (two outer windows and three electrodes) and four layers of gas. The outer windows are each 1 mm thick and the electrodes are each 0.5 mm thick. The gas layers are each 9.9 mm thick.

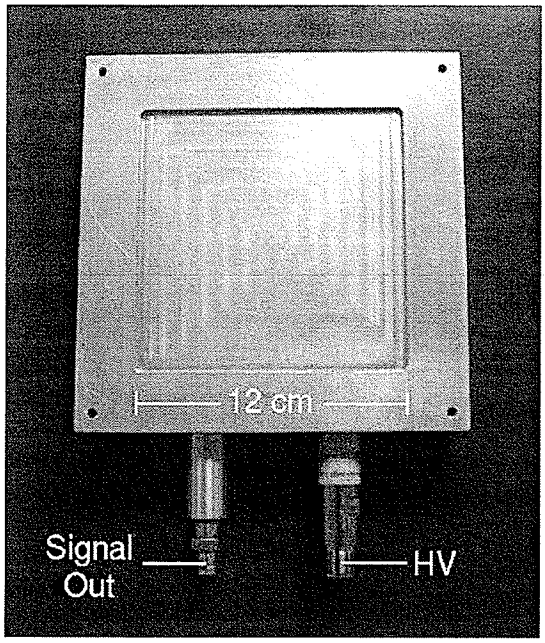

Figure 3.1: A photograph of one of the NPDGamma beam monitors. This photograph could be of any of the three monitors with serial numbers 084153, 084154 or 084155 and that are used as M3, M1 and M2 respectively. The beam monitors are constructed from aluminum and contain a mixture of ^{3}He, ^{4}He and N_2 gases. The neutron beam passes through the center of the monitor and would travel perpendicular to the plane of this photograph. There is one high voltage input which is applied to two outer electrodes. A BNC connection is used to measure the current passing to ground from the center electrode. The holes in the frame are used for mounting the monitor. A description of the beam monitors' construction is shown in figure 3.2. An illustration of the conversion of neutrons to an electrical signal is shown in figure 3.3.

A face-on view (bottom drawing in figure 3.2) shows that the active area of the monitors is a 12 cm wide square. The beam at Flight Path 12 measures 9 cm $\times$ 9 cm. Ions from neutron capture in the monitors that contain N_2 are not expected to travel farther than 1.6 cm (see section 3.2.3). The majority of the deposited energy therefore contributes to the detector signal (see p. 78).

A thicker frame out beyond the 12 cm face provides protection for the chamber. Including this frame, the chambers are 2″ wide along the direction of the beam.

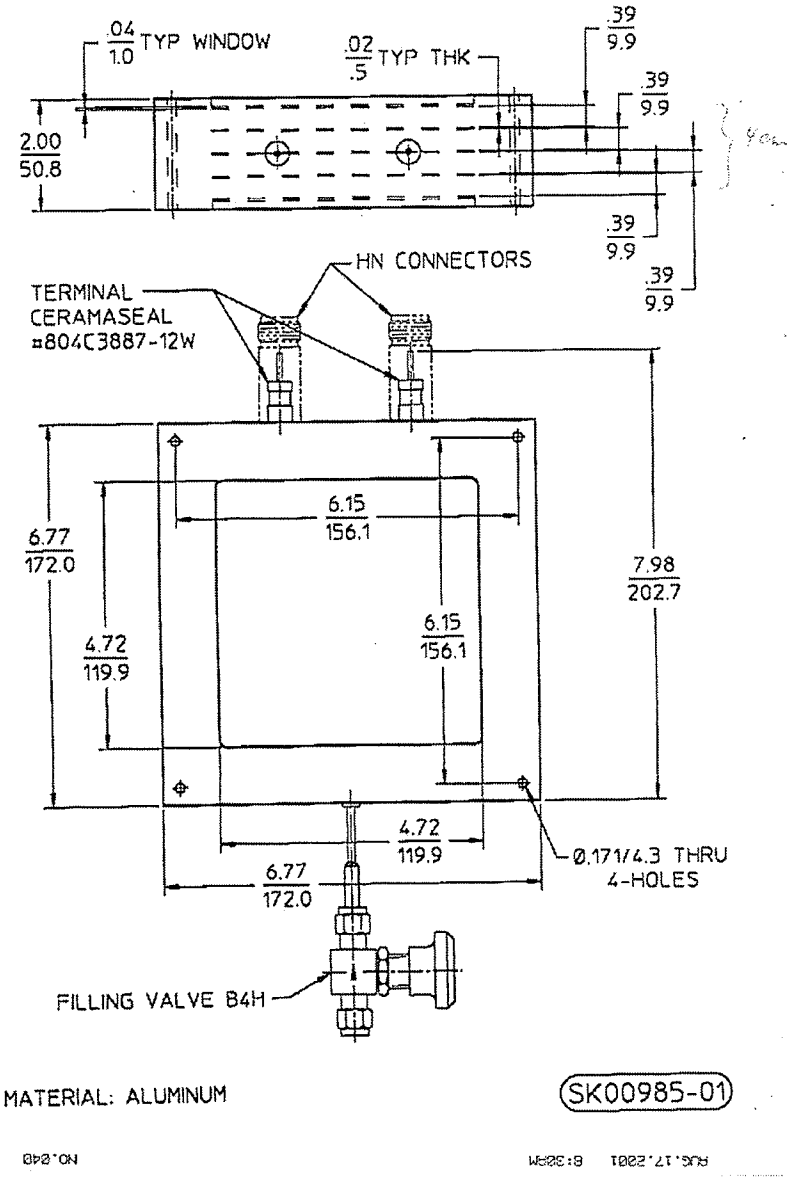

Figure 3.2: A drawing of the NPDGamma beam monitors, provided by the manufacturer LND Inc. This drawing applies to M1 and M2 (both of model number LND27528) as well as M3 and the prototype (both of model number LND27527). The different model numbers in this case only indicate different gas content specifications which are shown in table 3.1. Dimensions are shown in inches (top number) and mm (bottom number). Note that one of the connectors is BNC and not HN as shown here (see figure 3.1).

Two separate beam monitor gas mixtures were specified to the manufacturer. These quantities are shown in table 3.1. The three gases that are present in the monitors are ^{3}He, ^{4}He and N_2, each to varying amounts. Only the ^{3}He plays an active role in capturing neutrons.

identifier	^{3}He content	^{4}He content	N_2 content
prototype	0.50 atm	0	0.5 atm
SN 084153	0.50 atm	0	0.5 atm
SN 084154	0.03 atm	0.5 atm - 0.03 atm	0.5 atm
SN 084155	0.03 atm	0.5 atm - 0.03 atm	0.5 atm
TRIPLE[57]	1 atm	0	0

Table 3.1: Beam monitor gas pressure specifications. SN denotes the monitor's serial number. During gamma asymmetry measurements, monitors with serial numbers 084154 and 084155 are used as M1 and M2 around the polarizer. For the gamma asymmetry measurements that were made during the commissioning run in 2004, 084154 was used as M1 and 084155 was used as M2. Serial number 084153 is used as M3 at the back of the apparatus. A company representative stated that the gas pressures were determined at ambient temperature. The measured contents of the beam monitors are shown in table 3.9.

The amount of ^{3}He contained in a particular monitor is determined by its location in the apparatus. M1 and M2 should only absorb a small fraction of the neutrons and therefore must contain a small amount of ^{3}He. Four centimeters of ^{3}He at 0.03 atm and 0 °C absorbs 2.6 % of 10 meV neutrons (see section 3.1.2). There is no need for neutrons downstream of M3, and it is desirable for neutrons downstream of the hydrogen target to be absorbed so that background and radiation damage from scattering is minimized. M3 was therefore constructed with a higher concentration of ^{3}He. Four centimeters of ^{3}He at 0.5 atm and 0 °C absorbs 36 % of 10 meV neutrons.

N_2 plays no role in neutron capture. The N_2 is useful, however, for two reasons. First of all, nitrogen gives rise to a greater ionic stopping power. The distance traveled by ions

of hundreds of keV of energy (the energies of interest for the beam monitors) in 1 atm of gas is comparable to the 1 cm spacing between beam monitor electrodes. The presence of N_2 limits this range, therefore forcing more energy to be deposited by the ions before they exit the chamber. A larger and more stable signal is therefore obtained without absorbing more neutrons from the beam. Secondly, helium has a dielectric strength (the electric field strength at which breakdown occurs) that is 0.15 that of nitrogen [58]. The presence of nitrogen therefore allows for a higher voltage to be applied without sparking. Use of a higher voltage allows for a prompt collection time and minimizes recombination of electron-hole pairs.

^{4}He also plays no role in neutron capture. The extra ^{4}He allows for the monitors to have the same amount of helium, in order for them to have similar properties. Neutron capture is the only relevant property of the monitors that is dependent on a particular isotope, and so the four monitors are expected to be the same in all other respects. When comparing two monitor signals, for example, it is useful to be able to assume that the average energy deposited by a neutron is the same in the two monitors. It is also useful for the two monitors to have the same ion collections times when operated at the same high voltage. However, it was determined from test measurements that the compositions of the monitors are not identical (see section 3.3.4).

3.1.4 An expression for the signal from a beam monitor

Ionization chambers make use of the fact that energetic charged particles deposit energy as they pass through matter. The energy is deposited via ionization, and this ionization can in turn be collected as an electrical signal. ^{3}He provides an efficient method for conversion of low energy neutrons into energetic ions, and thus for conversion of a high flux beam of low energy neutrons into an electrical current. Figure 3.3 illustrates how this concept applies to the beam monitors.

Each monitor has three parallel plate electrodes. The two outer electrodes are held at a high voltage (3 kV for the measurements discussed in this thesis, except for the TRIPLE monitor which was run at 300 V). The center electrode is connected through a current meter

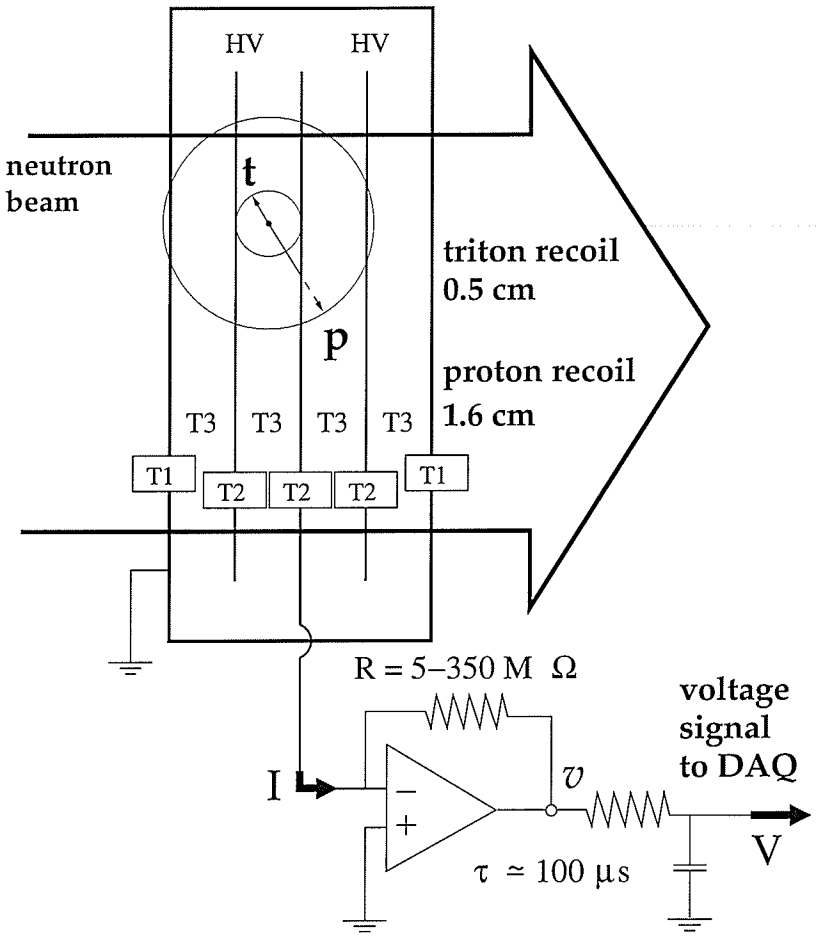

Figure 3.3: A side view of the capture of a neutron inside a beam monitor. The ions deposit their energy in the chamber through ionization of the gas. Due to the high rate of neutron capture, current mode detection is used. The current from ionization is sent to the center electrode by application of a high voltage to the two outer electrodes. The resulting current signal is converted into a voltage using a solid state preamplifier which is shown schematically in the lower part of the diagram. T_1 is the transmission of a 1 mm aluminum wall of the chamber. T_2 is the transmission of a 0.5 mm electrode and T_3 is the transmission of one of the gas gaps.

to ground. The charge created during ionization is therefore observed as a current signal that is dependent on the incident beam flux.

With this information, it is possible to derive an expression for the dependence of the output signal on the incident neutron flux. The ionization in the chamber is made possible by the energy that is released when a neutron capture occurs. As such, the average amount of energy deposited per neutron into the gas ($\overline{E}_{dep}$) is the first quantity to be considered. As some of the energy is also dissipated in the walls and electrodes, $\overline{E}_{dep}$ is not the same as the amount of energy released in the reaction.

When a neutron capture occurs, $\overline{E}_{dep}$ is distributed over a number of individual ionization events. During this process, electrons can be liberated from different energy levels, and other interactions besides ionization can take away energy. For a given $\overline{E}_{dep}$, the number of electron-hole pairs created is therefore determined by the amount of energy on average that is used up by the creation of one pair. This amount of energy is known as the *average energy dissipation per ion pair* (W) and is not the same as the ionization energy of the gas. There is not a clear consensus in the literature on the precise values of W. However, it is about 42 eV for He and 35 eV for N_2 [59].

The effect of varying the applied high voltage was studied during some tests that were carried out on Flight Path 5 at LANSCE. The voltage applied to the prototype monitor electrodes was varied during a time when the proton current to the spallation target was stable. Below 1 kV, the signal from the preamplifier increased with applied voltage. From 1 kV to 3 kV, however, the signal did not change. It is therefore believed that the monitors are operating in the region of voltages where electron-ion recombination is not occurring (see e.g. [60]). In this region, the applied voltage is high enough that no electron-hole recombination occurs, and thus all liberated charge is converted to a signal. The current signal out of the beam monitor is therefore determined as given in equation (3.4). N_{cap} is the total rate of signal-generating neutron capture and e, the charge on an electron, is the amount of charge liberated per ionization event.

$$I = N_{cap}\frac{\overline{E}_{dep}}{W}e \tag{3.4}$$

N_{cap} can be related to the total neutron flux, N, that is incident on the face of the monitor with the help of figure 3.3. T_1, T_2 and T_3 are the attenuations of the aluminum walls, aluminum electrodes and gas gaps respectively. The cross-section for an interaction

with ^{3}He is three orders of magnitude larger than that for nitrogen and five orders of magnitude larger than that for ^{4}He. T_3 is therefore treated as being due exclusively to ^{3}He. The probability for a neutron capture is correspondingly given by $(1 - T_3)$.

Charges that are accelerated towards the outer walls of the chamber are not converted to a signal, so N_{cap} includes only those neutrons that are captured in the two inner regions of the monitor. A beam monitor therefore has two *signal regions*, which are the regions that exist between the high voltage plates and the signal plate. By taking into consideration the attenuations that the beam encounters when traveling through the monitor to the detection regions, N_{cap} can be determined in terms of N:

$$\begin{aligned} N_{cap} &= NT_1T_3T_2(1-T_3) \qquad \text{(upstream region)} \\ &+ NT_1T_3T_2T_3T_2(1-T_3) \qquad \text{(downstream region)} \\ &= NT_1T_2T_3(1-T_3)(1+T_2T_3) \end{aligned} \tag{3.5}$$

The circuit shown in the lower part of figure 3.3 is a schematic representation of the solid state preamplifier [45] that is used to amplify the current signal and to convert it into a voltage. The resistor-op amp combination is a current-to-voltage converter which produces an output voltage given by:

$$V = IR. \tag{3.6}$$

The resistor-capacitor combination is a low pass filter that serves to eliminate high frequency noise. This low pass filter is set to have a time constant of approximately 100 μs. This time constant was chosen since it is small enough to not have an effect on data stored by the DAQ (the time bins have a width of 400 μs), and is about the same as the ion collection time.

Combining of equations (3.4), (3.5) and (3.6) provides an expression for the signal out of a beam monitor preamplifier:

$$V = NT_1T_2T_3(1-T_3)(1+T_2T_3)\frac{\overline{E}_{dep}}{W}eR. \tag{3.7}$$

In the case that higher time resolution is required, it will be important to remember that equation (3.7) does not take into account the existence of the low pass filter. Also, since

T_1 and T_2 are due in large part to scattering, equation (3.7) is not exact. However, the attenuation from the aluminum is small enough that, for the situations discussed in this thesis, T_1 and T_2 can be approximated as unity.

3.1.5 Correction for the low pass filter

Under conditions where higher time resolution is of importance, it is possible to make corrections to the expression that is given in equation (3.7). If not many measurements requiring high time resolution are being made, it can be preferable to use this method rather than to risk damaging the preamplifier by changing one of its components.

The relationship between V and v in figure 3.3 can be determined by considering the voltage drops across R and C as shown in equations (3.9) and (3.8) where $\frac{dQ}{dt}$ is the current flowing through the resistor and Q is the charge on the capacitor. Combination of equations (3.9) and (3.8) yields equation (3.10).

$$v = \frac{dQ}{dt}R + \frac{Q}{C} \tag{3.8}$$

$$V = \frac{Q}{C} \tag{3.9}$$

$$v = \frac{dV}{dt}RC + V \tag{3.10}$$

Given a collection of data points V_i which are sufficiently closely spaced at times t_i, it follows that V_i occurring at times T_i can be reliably approximated as shown in equations (3.11) and (3.12). Figure 3.4 shows an example of this correction.

$$v_i = \frac{V_{i+1} - V_i}{t_{i+1} - t_i}RC + \frac{V_i + V_{i+1}}{2} \tag{3.11}$$

$$T_i = \frac{t_i + t_{i+1}}{2} \tag{3.12}$$

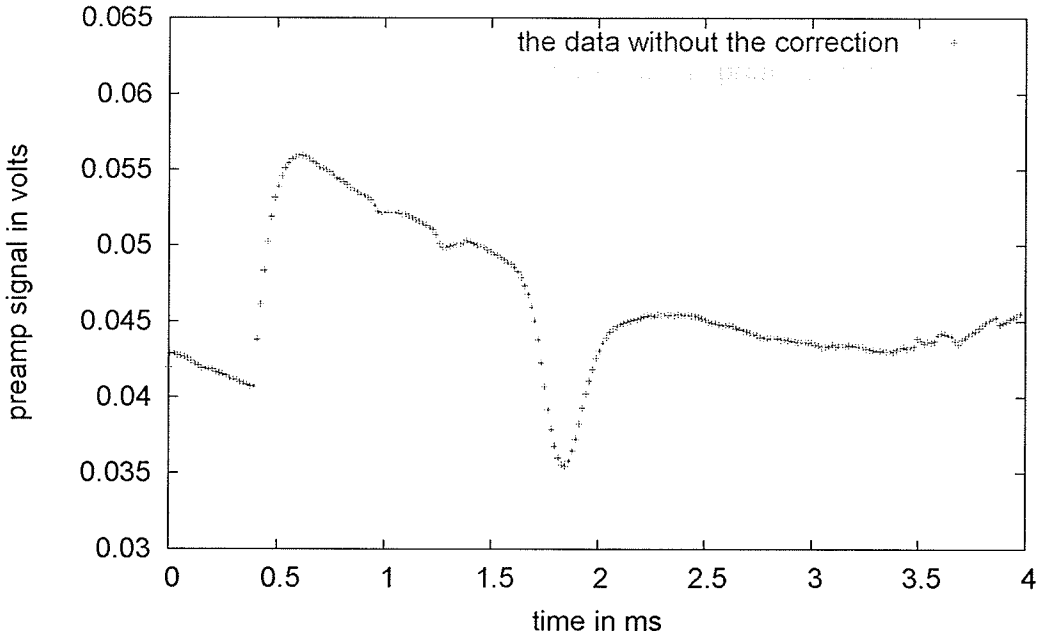

Figure 3.4: It is possible to correct for the low pass filter that is present in the beam monitor preamplifiers. This plot shows the effect of such a correction to a preamplifier with a 0.1 ms time constant. The plot is the signal downstream of a piece of indium foil. The data were taken using a digital oscilloscope and have a time resolution of 0.056 ms. Indium has multiple absorption resonances of well-defined energy that give rise to dips in transmitted flux. The features are shifted to earlier times and become noticeably more pronounced as a result of the correction. The signal at T0 is also much closer to vertical in the corrected data set. That the signal be vertical here is more reasonable since gamma rays and high energy neutrons arrive almost instantaneously from the source. The signal before T0 is not flat since the frame overlap chopper was not in use during this measurement.

3.1.6 Time binning and digitization

The voltage signals out of the beam monitor preamplifiers are digitized and stored in binary data files. Beam pulses arrive at 50 ms intervals. The first 40 ms after the start of each pulse is divided into 100 time bins of 0.4 ms duration each. A 10 ms break at the end of each pulse (during which there is not a significant number of neutrons in the beam) allows for the electronics to prepare for the following pulse. The NPDGamma data acquisition electronics

are synchronized with the accelerator by a signal that is sent from the accelerator control at the beginning of each beam pulse. This signal is referred to as the *T0 pulse*, and the start of each beam pulse is sometimes referred to as *T0* (or *T-zero*).

The beam monitor preamplifier voltages are sampled by 16 bit ADCs at 62.5 kHz and summed over each time bin. The digitized signal S that is recorded from an ADC and stored in a data file can be expressed in terms of the input analog voltage V as shown in equation (3.13). The signal is created by summing N samples over a time bin. V_{max} and V_{min} are the maximum and minimum voltages that can be read in by the ADC. Each sample of the analog voltage is converted into a binary integer of 16 bits before being added to the sum. In a base other than two, the integer that is stored in the data file to represent the voltage over one time bin is expressed as $\widetilde{S}$ in equation (3.13). The average voltage S can be deduced from $\widetilde{S}$ using equation (3.14).

$$\widetilde{S} = \left(\frac{2^n}{V_{max} - V_{min}}\right) \sum_{i=1}^{N} V_i \tag{3.13}$$

$$S = \frac{1}{N} \sum_{i=1}^{N} V_i = \left(\frac{V_{max} - V_{min}}{2^n}\right) \left(\frac{\widetilde{S}}{N}\right) \tag{3.14}$$

For the ADCs that were used for beam monitor data-taking, the following values apply: $n = 16$, $N = 25$, $V_{max} = 10$ V, and $V_{min} = -10$ V. When converting the digital data into an average voltage, a conversion factor of 81,920 counts/V is therefore used.

3.1.7 The beam monitor pedestals

One of the most useful aspects of the beam monitors is that, as indicated in equation (3.7), they provide a voltage that is linearly proportional to the incident beam flux. Until now the discussion has excluded any consideration of voltage offsets. Realistically, the signal voltage V in figure 3.3 is superposed on top of an offset voltage (pedestal). Typically the pedestals are in the millivolt range, and the signals of interest are in the range of volts or hundreds of millivolts. The pedestals are constant over a period of a few hours. Unless the pedestal is known and subtracted, it is not correct to assume a linear proportionality between beam flux and voltage. For this reason, pedestal runs are taken. A pedestal run is carried out in

the same manner as a regular data run, except a beam shutter is closed upstream of the apparatus. The beam shutter prevents any beam from entering the apparatus. Any analysis that requires a linear proportionality between beam flux and voltage is carried out after a subtraction of the voltage offsets.

A problem arises from the fact that a true voltage offset is not easily distinguised from background signals, such as from activation of the apparatus. For example, it was noticed that, when the frame overlap chopper blocks the beam at the end of a pulse (see p. 31), a signal is present above the pedestals (it exists above the signal that is observed when the shutter is closed). It is always present in M1 but is only present in M2 when the polarizer is not present in the apparatus. This signal has a level of about 20 mV, compared to typical M1 signals of 2-3 V. Since the polarizer is opaque to slow neutrons, this additional signal is consistent with the possibility that slow neutrons are in the beam, despite the use of the frame overlap chopper. Since the frame overlap chopper was designed to be opaque to slow neutrons, the most likely explanation for this observation is that overlap from two pulses previous is occurring. The analysis that is carried out in this thesis uses regular pedestal runs for the voltage offsets. When necessary, additional uncertainties are considered.

3.1.8 A transmission measurement

Given their usefulness for measuring beam flux, the beam monitors are particularly useful for performing beam transmission measurements. As was discussed in chapter 2, they are thus useful for monitoring the ortho- to para-hydrogen ratio of the liquid hydrogen target, for monitoring beam polarization, and for measuring the efficiency of the spin flipper.

A transmission measurement involves measuring the change of beam transmission that occurs when the properties of the apparatus change. Such a measurement is most easily performed with the use of two beam monitors. One monitor is used to measure the change in beam transmission that results from the attenuation being studied. The other monitor is used to account for any changes in flux that would have occured if the transmission had stayed fixed.

An illustration of a transmission measurement using the beam monitors is shown in

figure 3.5. This example consists of measuring the transmission of a piece of attenuating material. The top half of the diagram shows two beam monitors without the attenuating material in place. In such a case, the flux seen by the second monitor will be less than that seen by the first monitor. The reasons for this may include attenuation by absorption, scattering or collimation; or the possibility that neutrons have sufficient transverse velocity to leave the beam. Allow N to be defined as the flux incident on the first monitor and αN to be defined as the flux incident on the second monitor. The neutrons' behaviour is assumed to be independent of N. α is therefore also independent of N but is dependent on energy and on the positions of the monitors.

The lower half of figure 3.5 shows a measurement that is made at a different time. The beam flux seen by the first monitor has changed, and the attenuating material has been placed between the two monitors, so that the fraction seen by the second monitor has been changed by a factor T which depends on energy E. Neither monitor-preamplifier combination has been moved or altered.

The voltage out of the preamplifier in each case can be deduced from equation (3.7) as shown in equations (3.15). Each signal is dependent on the properties of the monitor-preamplifier combination that it originates from and is proportional to the flux incident on the monitor. The subscripts 1 and 2 are used to differentiate the two monitor-preamplifier combinations. $f(E)$ is used to represent the factor of proportionality between incident flux and voltage. $f(E)$ is characteristic to each monitor and is a function of neutron energy. The exact form of $f(E)$ is irrelevant to this analysis. Since the monitors are located at different distances from the source, the energies E_1 and E_2 are different for the same time of flight.

$$\begin{aligned} V_1 &= N f_1(E_1) R_1 \qquad & V_2 &= \alpha N f_2(E_2) R_2 \\ \widetilde{V_1} &= \widetilde{N} f_1(E_1) R_1 \qquad & \widetilde{V_2} &= T(E_2) \alpha \widetilde{N} f_2(E_2) R_2 \end{aligned} \tag{3.15}$$

The transmission T can then be deduced by considering a ratio between the pedestal-subtracted voltages from equations (3.15). This concept is demonstrated in equation (3.16). Since T is observed by the downstream monitor, the energies of any time of flight-dependent features in T should be calculated using the distance from the moderator of the downstream

monitor.

$$\frac{\widetilde{V_2}/\widetilde{V_1}}{V_2/V_1} = \frac{\left[T(E_2)\alpha\tilde{N}f_2(E_2)R_2\right] / \left[\tilde{N}f_1(E_1)R_1\right]}{[\alpha N f_2(E_2)R_2] / [N f_1(E_1)R_1]} = T(E_2) \tag{3.16}$$

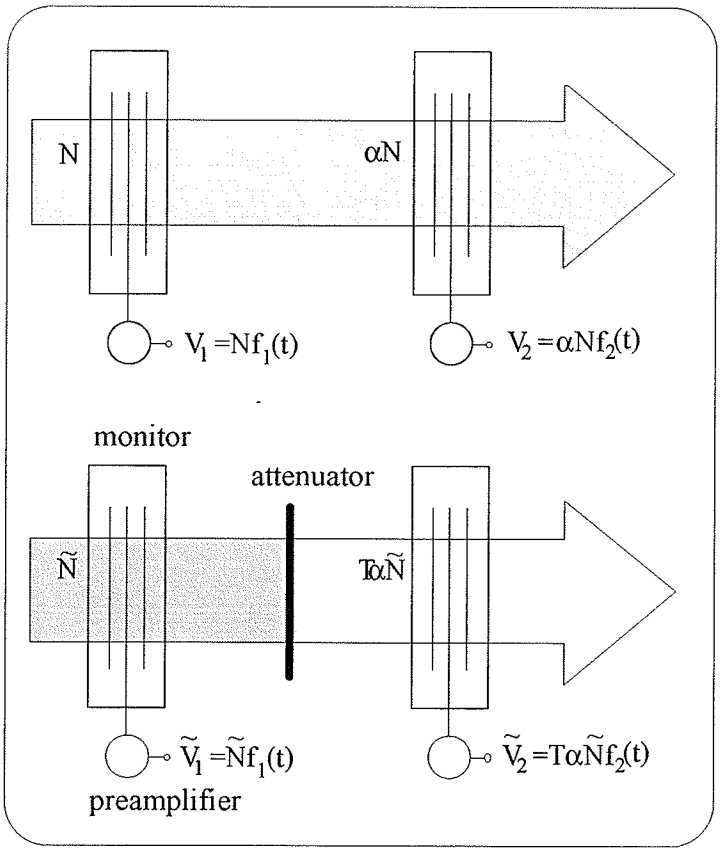

Figure 3.5: An illustration of a transmission measurement using the beam monitors. A measurement is made by recording the voltages from the preamplifiers with and without an attenuating material in between. Equation (3.7) shows how the voltages are dependent on: 1) the beam flux (N); 2) the neutron energy (E); 3) the properties of the preamplifiers (P); and 4) the properties of the monitors (M). A ratio of the four voltages allows for a determination of the change in transmission that arises due to the insertion of the attenuating material, as shown in equation (3.16). It is important to leave the preamplifiers and monitors untouched between the two stages of the measurement, and to calculate the ratio at a fixed time of flight, in order to be able to assume that the voltage signals are proportional to the beam flux.

3.2 A Monte Carlo Calculation of the energy deposited per neutron

3.2.1 Introduction to this section

This section discusses a methodology for finding the average ($\overline{E}_{dep}$) and standard deviation (σ_{Edep}) of the energy deposited per capture of a single neutron in the beam monitors.

Determining these quantities helps in providing insights into the properties of the beam monitors. For example, knowledge of σ_{Edep} provides information on how much noise to expect above neutron counting statistics. Also, since an approximate value of the W value of the gas is known, knowledge of $\overline{E}_{dep}$ can act as a test of whether the beam monitor calibration is reasonable. Knowledge of $\overline{E}_{dep}$ was also used in the assessment of the uncertainty in the ^{3}He content of the beam monitors.

The initial energies of the proton and triton are determined by knowing the amount of energy created in the n + ^{3}He reaction. The total energy released is known to equal 764 keV and to be entirely kinetic. By conservation of energy and momentum, it follows that the triton with a mass of 3.016 u will take away 191 keV and that the proton with a mass of 1.007 u will take away 573 keV.

With knowledge of the materials and geometries involved, a Monte Carlo calculation was used to integrate over the trajectories of individual ions, and hence to determine how much of each ion's recoil energy is deposited in the chamber. This calculation is divided into three stages. Stage one uses data from an external source to determine the stopping powers. Stages two and three involve a C++ calculation that was written using the data from stage one. The code for this program is available from the author on request.

3.2.2 Stage one: the stopping powers

The energy deposited by an ion in matter is calculated by knowledge of the *linear stopping power* S. This calculation follows directly from the definition of S which is given by:

$$S(E) = -\frac{dE}{dx} \tag{3.17}$$

E is the energy of the ion and x is its distance traveled.

$S(E)$ determines the amount of energy lost by the ion as it is stopped by the gas. As such, $S(E)$ is a crucial element in the calculation of $\overline{E}_{dep}$ and σ_{Edep}. S is determined by the properties of the gas mixture, by the mass and charge of the ion, and by E.

The objective of this stage of the calculation was to determine the stopping powers of the ions in the gas mixtures being studied. This objective was achieved using version 2003.26 of the simulation package SRIM that was obtained from reference [61]. SRIM is a group of programs that are designed specifically to calculate the stopping powers and ranges of ions in matter. SRIM calculations are carried out using a statistical method that takes into account Coulomb effects as they occur in the form of screening, overlapping electron shells, electronic and interatomic bond structures, and the velocity dependent charge state of the ion. SRIM also takes into account stopping from internuclear interactions. A description of the method involved can be found in books written by the SRIM authors [62].

The SRIM programs output stopping powers for a particular mixture of gases at particular pressures and stoichiometric combinations. However, it is preferable for the beam monitor Monte Carlo to be adjustable so that it apply to a variety of gas compositions. In order to allow for this flexibility, the stopping power data were obtained for each gas individually. The process of mixing the gases was then integrated into the Monte Carlo itself.

The method for combining the stopping power data is obtained based on the observations that: 1) The interactions of an ion with the gas are probabilistic and determined by single ion-atom or ion-molecule interactions; and that 2) the gas constituents of the monitor can be treated to a good approximation as ideal gases. The result of observation 1) is that the number of interactions leading to energy loss scales linearly with the number of gas molecules present. The result of observation 2) is that intermolecular interactions cannot contribute to an ion's energy loss. The energy loss per ion-molecule interaction is therefore independent of the density of the gas and the nature of the other molecules.

It was therefore assumed that the stopping power can be obtained as a linear combination of the individual stopping powers of the constituent gases. The coefficient that determines the contribution of each gas is that gas's volume density which, for an ideal gas,

is proportional to pressure [1]. In order to express this statement in a concise mathematical form, the value of $S(E)$ for each individual gas at STP will be referred to as $S_g(E)$ where g denotes the gas. $S(E)$ is then determined in terms of the $S_g(E)$ which are weighted by the pressures P_g of their corresponding gases. This is expressed as:

$$S(E) = \sum_g P_g S_g(E) = P_{3He} S_{3He}(E) + P_{4He} S_{4He}(E) + P_{N2} S_{N2}(E) \qquad (3.18)$$

where P_g is measured in atmospheres at 0 °C.

Figure 3.6 shows the data that were obtained from the SRIM calculations. Some features are worth noting. First of all, at higher energies, the curves for the proton and the triton are very similar but scale differently as a function of energy. This can be understood by considering the fact that, for constant ionic charge and constant material properties, the stopping of energetic ions is determined uniquely by the ion's speed. Speed is in turn uniquely determined by the ratio between kinetic energy (T) and mass (M). It is therefore expected that the two curves be the same, if plotted versus T/M. Since the triton is three times as massive as the proton, this explains why similar features at higher energies occur for $T_t = 3T_p$ (p = proton, t = triton).

Secondly, the ratio between the peak stopping power values for helium and nitrogen is consistent with the value that has been empirically observed [63]. This ratio is different from that predicted by the Bethe-Bloch formula [2] since at such energies the velocity-dependent charge state of the ion becomes important. Thirdly, the stopping power from nuclear interactions becomes important at eV energies where it is one to two orders of magnitude more important than the electronic stopping power. This is the only range in energies where the difference between ^{3}He and ^{4}He is noticeable, due to the smaller mass of the ^{3}He nucleus. Both nuclear and electronic stopping powers were included in the beam monitor Monte Carlo.

These stopping power data were integrated into the Monte Carlo algorithm as arrays

[1] This method for mixing stopping powers of ideal gases happens to be a special case of *Bragg's Rule* which states that the mass stopping power (stopping power per unit mass) of a material is a linear sum, weighted by mass, of the individual mass stopping powers of the material's constituents.

[2] The Bethe-Bloch formula (accurate in determining stopping powers for heavy ions of greater then a few hundred keV energy) is discussed in popular textbooks such as [64].

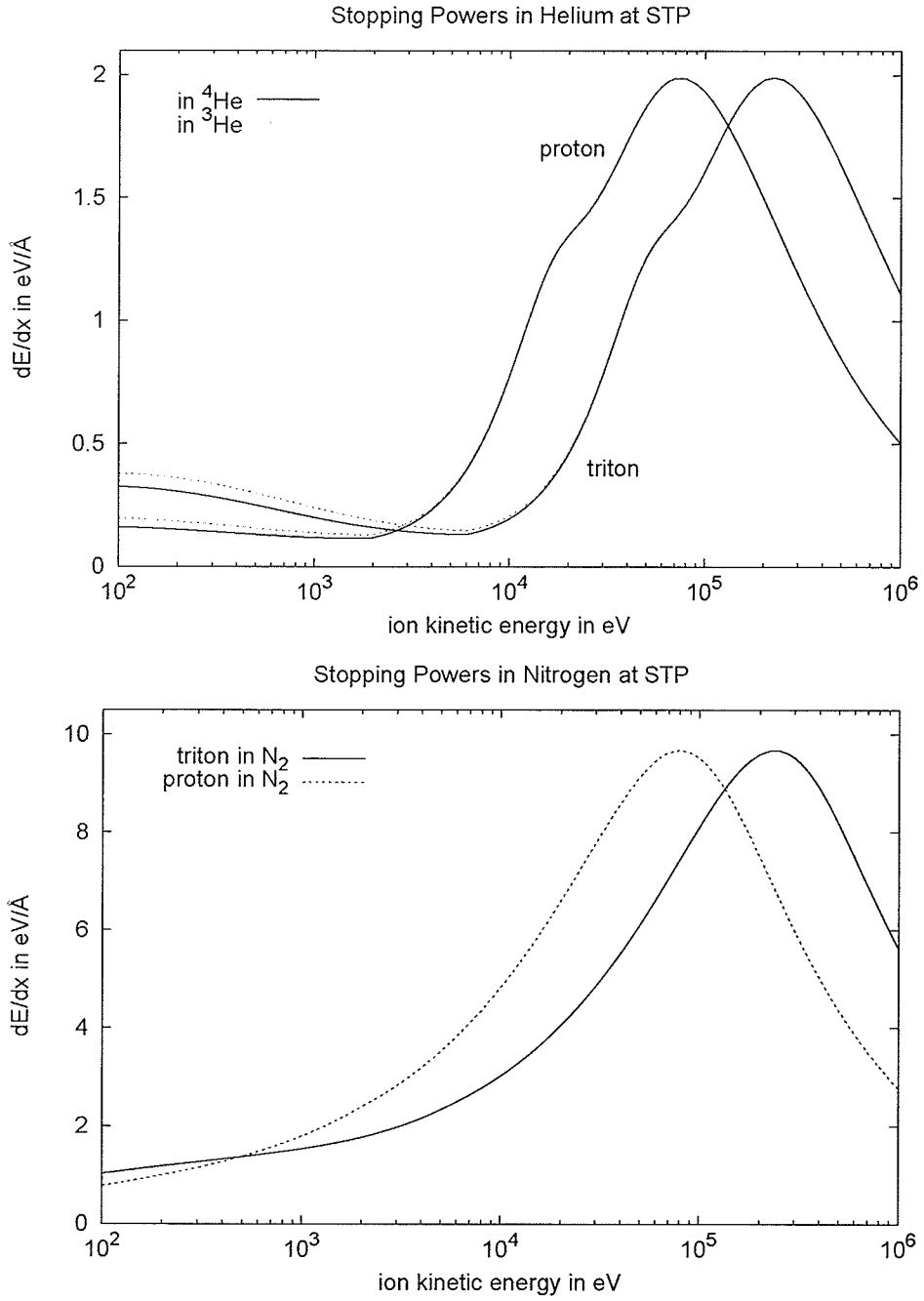

Figure 3.6: The stopping powers of protons and tritons in helium and nitrogen gas, as obtained from SRIM. The energy range shown includes the energies of the ions that are produced by neutron detection in the beam monitors.

with 130 values at logarithmic increments between 10 eV and 900 keV. A routine was written that allowed to linearly interpolate the data between array entries.

3.2.3 Stage two: energy deposited as a function of distance

The purpose of stage two was to use the stopping power data in order to determine the amount of energy deposited into the gas mixture by each ion separately, as a function of its distance traveled ($E_{dep}(x)$).

At this stage a simplification was made. It was assumed that the ions experience no change in energy except for that caused by the stopping of the gas. This assumption is incorrect due to the fact that the very functioning of the monitors is dependent on the application of a high voltage. However, since the proton and triton are both of charge e, and since the voltage is typically 3 kV, this leads to an error on the order of 3 keV per ion, or 1.2% of the average amount deposited. This error is of minimal significance to the analysis and the approximation was deemed worthwhile due to the fact that the simulation would have otherwise been much more computationally demanding.

The method for this stage of the calculation follows directly from equation (3.17). The result is equation (3.19), which relies on the fact that S is determined uniquely by the ion's energy E, which in turn is determined uniquely by the distance traveled by the ion.

$$E_{dep}(x) = \int_0^x S\left(E(x)\right) dx \tag{3.19}$$

A calculation using equation (3.19) and the SRIM data was done iteratively by allowing an ion to travel over small distance increments δx, thus causing it to lose energy $\delta \mathrm{E} = \mathrm{S(E)}\delta x$ at each increment. In the program, E was updated each time by taking into account the amount of energy lost, until the total energy had been exhausted. A record was thus created of the energy deposited by each ion as a function of its distance traveled. These data were stored for later use by the program.

The distance after which the ion's energy is exhausted was recorded as the range of the ions in the gas. It was determined that for a beam monitor containing 0.04 atm ^{3}He, 0.46 atm ^{4}He and 0.5 atm N_2, a 191 keV triton travels 0.52 cm and a 573 keV proton travels 1.64 cm. These calculations can be compared to table 3.2, which shows the ranges

that were output directly by the SRIM program for the same gas mixture. The small discrepancy between the ranges from the Monte Carlo and from SRIM was considered when determining the uncertainty in the results from the Monte Carlo (see section 3.2.6).

	energy (keV)	range (mm)	longitudinal straggling (mm)	lateral straggling (mm)
proton	500	13.2	0.56	0.60
	550	15.2	0.64	0.66
	600	17.2	0.72	0.73
	650	19.5	0.80	0.80
triton	170	4.5	0.36	0.48
	180	4.7	0.36	0.49
	200	5.0	0.37	0.50
	225	5.4	0.38	0.51

Table 3.2: Proton and triton ranges calculated by SRIM for a gas combination similar to that of the NPDGamma beam monitors. The proton and triton have recoil energies of 576 and 191 keV respectively. Straggling is explained briefly on page 70.

3.2.4 Stage three: Generation of the E_{dep} distribution

The final stage was a Monte Carlo simulation which generated the product ions at random locations with random directions. The purpose of this simulation was to determine how far each ion would travel before leaving the detection region. The distance traveled determines the amount of energy $E_{dep,i}$ deposited by the i^{th} ion.

An ion is considered as having left the detection region when it has hit an aluminum electrode. This is because an electrode, being a conductor, is an equipotential surface. Ionization created in the electrodes will therefore not contribute any current to the detector

signal.

Since the beam is 9.5 cm wide, some protons travel beyond the 12 cm $\times$ 12 cm square area defined by the parallel electrodes. It is not initially obvious how to treat these ions since the electric field at these boundaries has not been determined. However, it was determined that the plates are large enough for their boundaries to have a negligible effect on the calculation of $\overline{E}_{dep}$ and σ_{Edep}. This is discussed in section 3.2.6.

In determining how far the ions travel before hitting a wall, another simplification was made. It was assumed that the ions travel in straight lines. This assumption is not strictly correct for two reasons.

The first reason is the very nature of the stopping by the gas. The stopping of a particle in matter is a process that is determined by many interactions averaged over its entire trajectory. The result is a statistical effect that for a sufficiently large particle represents itself as a drag force. However, a particle the size of an ion experiences an effect analogous to a random walk which causes the ion's path to deviate from a straight line. The same effect causes the total distance traveled by the ions to vary. For a mixture of 0.5 atm ^{3}He and 0.5 atm N_2, it was determined from SRIM that this effect (which is referred to as straggling) can lead to deviations that are approximately 5% of the total distance traveled for the proton and 10% for the triton (see table 3.2).

However, deviations from the average path are expected to not occur preferentially in any direction. Furthermore, the symmetry of the capture region and of the neutron beam is assumed to be such that variations in the path of the ions do not alter $\overline{E}_{dep}$.

The second reason why it is incorrect to state that ions travel in straight lines is the existence of the electric field. It should be noted here that the ion chambers contain a sufficiently small amount of ^{3}He for the neutrons to have only an unnoticeable preference for capture near the upstream wall of the capture region. Deviations in $E_{dep,i}$ created by ions that deposit less energy by being pulled towards one wall will therefore be equally compensated by opposite deviations in $E_{dep,i}$ on the other side of the chamber.

These two effects which cause extra deviations in the motion of the ions were therefore assumed to not alter $\overline{E}_{dep}$. They most likely lead to an increase in σ_{Edep} which is

itself a measure of such variations, but precise knowledge of σ_{Edep} is not important for the interpretation of the beam monitor data.

Once it has been decided that the ions travel in straight lines, it is possible to generate trajectories and calculate the energy deposited by each ion before it leaves the detection region. This was carried out according to the series of steps explained below.

random number generation

Random number distributions are generated in the Monte Carlo by starting with a uniform normalized distribution p(r)=1 with $r \in [0,1]$. Numbers from the uniform distribution are mapped into the distribution of interest via a method that is discussed in popular texts on computational methods (see for example pp. 81-82 of [65]). This method can be summarized in the form of an equation. A random number $z \in (-\infty, \infty)$ is generated according to a general probability density P(z) by use of equation (3.20).

$$r = \int_{-\infty}^{z} P(z)dz. \tag{3.20}$$

step one: generation of random capture locations

When generating a neutron capture, first the location at which the capture occurs is considered. Where the neutron is captured is a probabilistic process determined by three factors: 1) the geometry of the capture region; 2) the distribution of neutrons perpendicular to the beam; and 3) the attenuation of the beam parallel to the direction of the neutrons' travel.

The capture region is a 9.9 mm $\times$ 119.9 mm $\times$ 119.9 mm rectangular box. Fringe effects at the boundaries are not of importance (see p. 78). An energetic ion that exists in this region will contribute to the signal collected at the electrodes.

The beam is 9.5 cm $\times$ 9.5 cm square. It is concentric with and perpendicular to the parallel plates of the monitor. In a plane parallel to the plates, the probability for detection is assumed to be equally likely at any point in this square. This straightforward distribution is very close to the actual situation [42]. However, since the parallel plates are wide enough for the boundaries to be neglected, and since the spacing between the plates is constant,

the areal distribution of the beam is irrelevant.

Parallel to the axis of the beam, the density of the beam follows an exponential decay due to attenuation as neutrons undergo charge exchange with ^{3}He nuclei. As a result, a captured neutron will have a higher probability for being detected near the upstream wall of the capture region. This effect is not of importance for thin monitors, which attenuate 0.8% of the beam over 1 cm of ^{3}He at 10 meV. However, the effect will be of greater significance for monitors of higher ^{3}He content.

The density of neutrons along the z axis parallel to the beam is expressed as $N(z) = N(0)exp(-n\sigma z)$ where $z = 0$ exists at the upstream wall of the capture region. The width of the capture region is l, and the volume number density and cross section of ^{3}He are n and σ respectively. The number of neutrons that have been detected between $z = z_1$ and $z = z_2 > z_1$ is $N_{det}(z_1, z_2) = N(z_1) - N(z_2)$. The probability for an event of interest to lie between z and $z + dz$ is therefore given by equation (3.21).

$$P(z)dz = \frac{N_{det}(z, z+dz)}{N_{det}(0, l)} = \frac{n\sigma exp(-n\sigma z)dz}{1 - exp(-n\sigma l)} \tag{3.21}$$

It is now possible to apply equation (3.20) in order to generate numbers according to the distribution given in equation (3.21). The result is given in equation (3.22). The number $z \in [0, l]$ is generated according to the distribution in equation (3.21) and $r \in [0, 1]$ is generated from the uniform distribution.

$$z = -\frac{1}{n\sigma} ln\left(1 - \left[1 - exp\left(-n\sigma l\right)\right] r\right) \tag{3.22}$$

step two: generation of random recoil directions

Once the capture location of the neutron has been determined, the direction of recoil of the ions must be generated. The momentum of the neutron is small enough that the two ions can be considered as having opposite recoil momenta. A random direction out of a 4π solid angle is determined for the direction of travel of the proton. The triton travels in the opposite direction.

Both an azimuthal angle $\phi \in [0, 2\pi)$ and a polar angle $\theta \in [0, \pi]$ must be generated every time that a random direction is created. The probability density $P(\theta, \phi)$ for a given pair

of angles is determined by the size of the corresponding solid angle element, as shown in equation (3.23).

$$P(\theta,\phi)d\theta d\phi = \frac{d\Omega}{4\pi} = \frac{sin\theta d\theta d\phi}{4\pi} \tag{3.23}$$

The solid angle element $d\Omega$ is independent of the azimuthal angle ϕ. As a result, the probability density $P(\phi)$ is uniform between the limits of ϕ. The resulting $P(\phi)d\phi$ is shown in equation (3.24).

$$P(\phi)d\phi = \frac{d\phi}{2\pi} \tag{3.24}$$

The method for generating ϕ from the uniform density $P(r)$ is shown in equation (3.25).

$$\phi = 2\pi r \tag{3.25}$$

In order for ϕ and θ to be generated independently, it is necessary that $P(\theta,\phi)$ be separable in terms of θ and ϕ. From equation (3.23), it can be seen that this is indeed the case. Furthermore, from equations (3.23) and (3.24), $P(\theta)d\theta$ can be determined. This result is shown in equation (3.26).

$$P(\theta)d\theta = \frac{sin\theta d\theta}{2} \tag{3.26}$$

The method for generating θ from the uniform density $P(r)$ follows directly from equation (3.20) and is shown in equation (3.27).

$$\theta = arccos(2r) \tag{3.27}$$

step three: determination of the energy deposited per ion

The following parameters have now been established: 1) the location at which the two ions are created; 2) the initial energy and direction of travel of each ion; 3) the boundaries of the capture region; 4) the maximum range of each ion; and 5) the amount of energy deposited by each ion as a function of its distance traveled. It is therefore possible to determine how much energy an ion deposits by knowing how far it is allowed to travel before being stopped by the gas or before leaving the detection region. The sum of the energies for the two ions is recorded for each neutron capture. This calculation is repeated for many neutron captures

so that a mean and standard deviation are determined. It is worth noting that, without the approximation that the ions travel in straight lines, it would have been necessary to calculate the entire trajectory and integrate over the energy lost by each ion individually.

3.2.5 The form of the E_{dep} distribution

the distribution for one neutron at a time

The above procedure was carried out for a total of 10^7 neutron captures. The results were tallied into a histogram of 500 bins between 0 and 1 MeV. The histogram has several interesting features and is shown in figure 3.7.

A method of varying the ^{3}He content of the monitors was used in order to understand the origin of these features. This method uses a version of the Monte Carlo that calculates stopping powers for a mixture of 0.5 atm N_2 and 0.5 atm He. The ^{3}He content is only a measure of the probability for a neutron to capture near the entrance window of the chamber.

Given an infinite amount of ^{3}He, all neutrons capture exactly at the location of the upstream wall. In this case, either a proton or a triton will deposit energy in the monitor gas, but not both for a given neutron capture. The distribution corresponding to 2×10^9 atm of ^{3}He is shown in curve 1 of figure 3.7. A spike occurs in curve 1 at 191 keV, the energy of the triton. The triton has a maximum range that is less than the spacing between electrodes, and therefore deposits all of its energy in the detector. A spike also occurs in curve 1 at 573 keV, the energy of the proton. This spike arises due to the fact that many protons travel in directions that allow them to deposit all of their energy.

There is also a continuum of energies below the proton energy. This continuum corresponds to protons that are stopped by the wall. Since stopping by the wall allows for a range of distances of travel in the gas, it also therefore allows for a range of deposited energies. The low energy cutoff of the continuum corresponds to the energy deposited by protons that have traveled perpendicular to the electrodes.

The continuum is taller for smaller deposited energies (corresponding to shorter distances of travel x in the gas). This phenomenon can be explained in part by the fact that $dx/d\Omega$

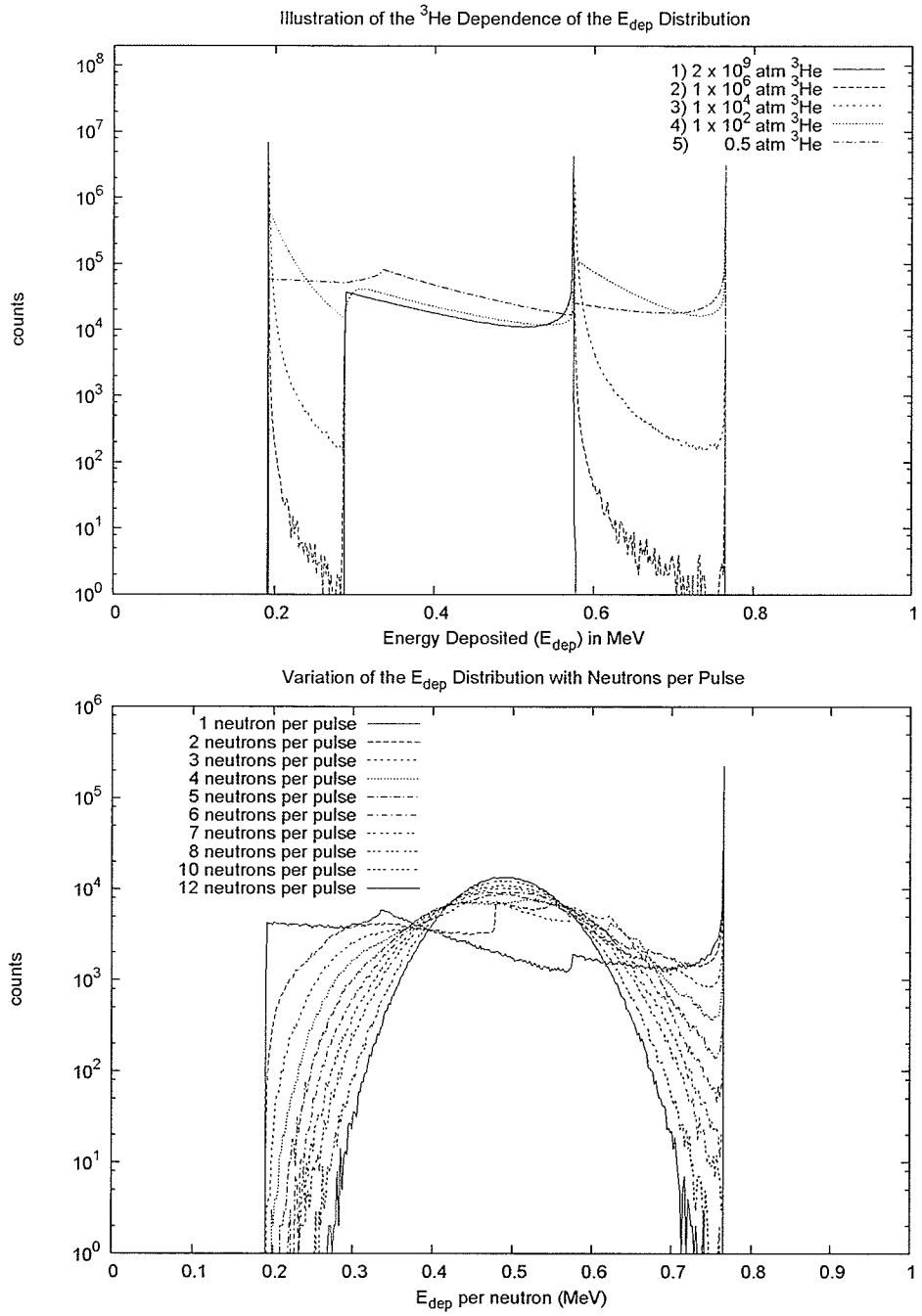

Figure 3.7: Histograms of the energy deposited per neutron in the beam monitors. The histograms in the upper graph show the distributions that result when only one neutron is considered per count (E_{dep}). This single neutron distribution is shown for various (unrealistic) ^{3}He pressures. Varying the ^{3}He pressure in this way serves as an aid for understanding the features of the single neutron distribution. The histograms in the lower graph illustrate how the distribution of E_{dep} per neutron ($\widetilde{E}_{dep}$) approaches a symmetric shape when the signal due to several neutron captures is considered.

increases with θ (θ is the polar angle measured from the direction of neutron velocity, x is the distance traveled by the proton before hitting the downstream wall, and Ω is the solid angle subtended about the point of origin of the proton). More protons are therefore collected into bins that correspond to shorter distances of travel. If dE/dx is treated as constant, then it is expected that more protons be collected into bins of smaller deposited energies.

The continuum is taller at larger deposited energies since the proton's remaining energy is small and so, as visible in figure 3.6, dE/dx is also small. Allow N to be the number of protons that hit an electrode with remaining energy E. The probability distribution $dN/dE = (dN/dx)/(dE/dx)$ therefore increases. This effect overpowers the binning effect that is mentioned in the previous paragraph since $dx/d\Omega$ is proportional to x^2, x changes by a factor of 1.5, and dE/dx changes by a factor of 10.

As the amount of ^{3}He in the chamber is decreased, the likelihood of a neutron being captured away from the upstream wall becomes greater. It then becomes possible for both ions to deposit energy. Continua begin to form at energies above both spikes. These new continua correspond to events where one ion deposits all of its energy and the other is able to deposit some of its energy. A third spike begins to develop at 764 keV, the sum of both ions' energies. This spike corresponds to the situation where the ions travel parallel to the walls and deposit all of their energy.

As the amount of ^{3}He is decreased further, it can be seen that events that were concentrated into the lower energy spikes and proton continuum become spread out throughout the histogram and into the third spike. For example, the lower edge of the proton continuum becomes spread over a range of higher energies. This shift of the lower edge is probably due to the energy dependence of $S(E)$ (see figure 3.6). As the ^{3}He content is decreased, some events that corresponded to protons starting at one wall and stopping at the other become replaced by ion pairs that start at the center of the chamber and hit both walls. The integral of $S(E)$ over the ions' paths is larger in the case of events involving both ions. The extent of this shift has not been verified quantitatively, but it makes sense to expect the lower edge of the proton continuum to spread out into events involving either one or

both ions. Furthermore, those involving both ions should shift to higher energies.

the distribution for several captures at a time

The energy distributions that are shown in the top half of figure 3.7 correspond to one neutron capture per binned event. The beam monitor data for NPDGamma contain the current signal from a large number of neutrons integrated over a time bin. It may therefore be useful to study the distribution of E_{dep} per neutron in the case where several neutrons are detected at once. For the purposes of this analysis, an event of neutrons detected together is called a *pulse*.

A histogram similar to those shown in the top half of figure 3.7 was used as a parent distribution. A number n of neutrons was created per pulse so that an average value $\widetilde{E}_{dep,j} = \sum_i^n E_{dep,i}/n$ could be determined for the j^{th} pulse. A total number of N pulses was thus created, in order to fill a histogram representing the distribution of $\widetilde{E}_{dep}$ for a given value of n. Histograms were filled for various values of n.

At this point a distinction of the different quantities involved is useful for purposes of clarity. E_{dep} is the energy deposited by a neutron in the monitor and can vary from neutron to neutron. The distribution of E_{dep} for an infinite number of neutron captures has average value $\overline{E}_{dep}$ and standard deviation σ_{Edep}. For a single pulse comprising a total of n neutron captures, E_{dep} has an average value of $\widetilde{E}_{dep}$. The distribution of $\widetilde{E}_{dep}$ for an infinite number of pulses also has average value $\overline{E}_{dep}$, but has a different standard deviation of $\sigma_{\widetilde{E}dep}$.

The lower half of figure 3.7 shows how the distribution of $\widetilde{E}_{dep}$ takes on a more symmetric form as n becomes larger. In fact, as n increases, the E_{dep} distribution approaches a Gaussian in shape. This is illustrated qualitatively in figure 3.7 by the fact that the distribution begins to look similar to a parabola when the vertical scale is logarithmic. These plots are still slightly asymmetric, however, in favor of the higher energy side of the distribution.

Figure 3.8 shows plots of the $\widetilde{E}_{dep}$ distribution for larger values of n. These histograms were fit to Gaussians in order to observe the dependence of the nature of the Gaussian on n. The Gaussian fits were carried out by searching a three-dimensional grid in the parameter space spanned by A, $\sigma_{\widetilde{E}dep}$ and $\overline{E}_{dep}$, the parameters of the Gaussian expression $g(\widetilde{E}_{dep})$

given by:

$$g(\widetilde{E}_{dep}) = \frac{A}{\sqrt{2\pi}} exp\left[-\left(\frac{\widetilde{E}_{dep} - \overline{E}_{dep}}{\sigma_{\widetilde{E}dep}}\right)^2\right]. \tag{3.28}$$

The fit corresponds to the grid point that allowed for the minimum χ^2. The error in each of the parameters was taken to be the variation that would cause the χ^2 per degree of freedom (χ^2/dof) to increase by one (if best $\chi^2/dof \leq 1$) or to double (if best $\chi^2/dof > 1$). Using this method it was determined that $\overline{E}_{dep} = 491.6 \pm 0.1$ keV and $\sigma_{Edep} = 206 \pm 3$ keV, where the uncertainties are entirely statistical. Note however that this value corresponds to a mixture of gases that is different from the mixture present in the beam monitors. For the value corresponding to the true mixture, see page 82.

3.2.6 Sources of uncertainty

The uncertainties in the calculation of $\overline{E}_{dep}$ and $\sigma_{\widetilde{E}dep}$ have been until now entirely from counting statistics. A consideration of other sources of uncertainty follows.

edge effects at the electrode boundaries

The importance of the fringe fields at the boundaries of the electrodes have not yet been considered in detail. If significant, the existence of the boundaries would alter the effective value of $\overline{E}_{dep}$ since charge created far enough from the boundaries would see no field and would therefore not be collected. In order to address this question, two calculations were done: one with walls at the boundaries of the 12 cm square electrodes and one without. Beyond these walls, neutrons were not allowed to deposit any more energy. The calculation with walls at 4800 neutrons per pulse yielded $\overline{E}_{dep} = 491.57 \pm 0.06$ keV and $\sigma_{\widetilde{E}dep} = 2.97 \pm 0.04$ keV (the results stated on page 78 and in figure 3.8 were done with walls). The calculation without the walls yielded $\overline{E}_{dep} = 491.96 \pm 0.06$ keV and $\sigma_{\widetilde{E}dep} = 2.98 \pm 0.05$ keV. The uncertainties are entirely statistical. The difference between these two results is small in comparison to other effects that will be discussed, and is therefore neglected.

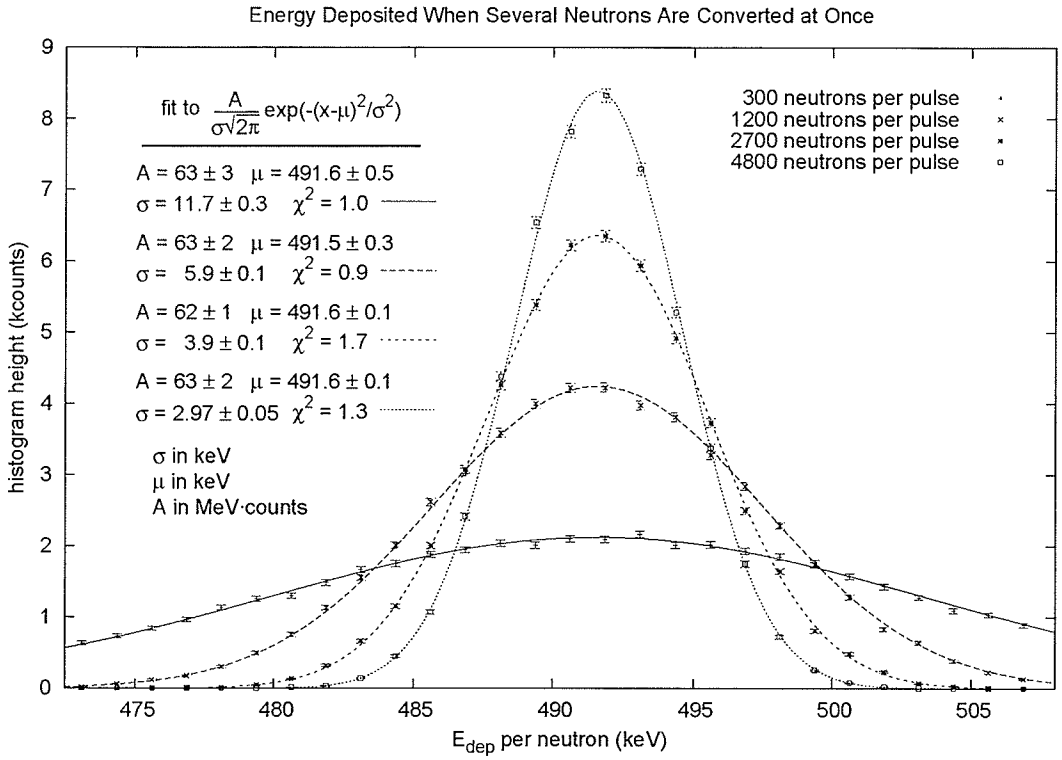

Figure 3.8: When enough neutrons are captured in the monitor at once, the distribution for the average energy deposited per neutron, $\widetilde{E}_{dep}$, is Gaussian. The gas pressures that were used in the calculation that produced this figure are slightly higher than the values that were later measured. The values that correspond to the measured pressures are given on page 82.

the high voltage

One of the assumptions of this calculation was that the high voltage electrodes do not affect the energy deposited by the ions. In reality, an ion's energy will be determined by the electric field. Attempts to calculate the importance of this effect precisely are complicated by the difficulty of calculating each ion's trajectory individually. Such calculations were avoided since they would have been much more computationally demanding.

The electric field can change the energy of the ions, thus affecting how much energy they deposit. However, due to the fact that the potential difference across the plates is 3

kV, and that the charge on each of the ions is e, the maximum energy that either ion can gain or lose due to the electric field is 3 keV.

The electric field can also affect the stopping power of the gas, which is energy dependent. However, for ions with energies that are significant for this calculation, the stopping powers can be considered constant for a change in energy of a few keV. The stopping powers change more considerably over the keV range for ions that themselves have keV energies, but such ions do not have enough energy remaining to be of importance to the calculation.

The electric field can also affect the trajectories of the ions, thus determining how far they will travel before hitting an electrode. Once again, however, ions of significant energy will not be deflected in a significant way by a 3 kV field. This effect was investigated by computing the path length of an ion's parabolic trajectory in the electric field alone and using the stopping power to estimate the difference in deposited energy that would arise from correcting for the different path length. The result was found to be much less than 3 keV per ion.

The behaviour of the ions is therefore consistent with the Monte Carlo for energies that are significantly greater than the potential energy associated with the field. The case in which both ions would change the result by the maximum amount each is expected to be rare. The uncertainty in $\overline{E}_{dep}$ and σ_{Edep} from this effect was therefore taken to be 3 keV.

ion ranges and placement of the electrodes

The distance that an ion travels before being stopped by an electrode or by the gas plays an important role in the determination of E_{dep}. The uncertainty in $\overline{E}_{dep}$ must therefore be dependent on an uncertainty in this distance, which can be broken into two independent components: 1) imprecision in the placement of the electrodes; and 2) lack of knowledge of the ion's mean range in the gas.

The drawings from LND inc. state the positions of the electrodes to within 0.1 mm, which corresponds to a 1 % uncertainty in the interelectrode gaps. The Monte Carlo was rerun with the electrode spacing at 0.96 cm and at 1.02 cm. With the walls spaced 0.96 cm the result was $\overline{E}_{dep} = 485.13 \pm 0.06$ keV and $\sigma_{Edep} = 203.29 \pm 0.05$ keV. With the walls

spaced 1.02 cm the result was $\overline{E}_{dep} = 497.61 \pm 0.06$ keV and $\sigma_{Edep} = 202.88 \pm 0.05$ keV. This gives rise to a variation of ± 0.5 %.

According to table 3.2, SRIM calculates the ranges to be 16.2 mm for the proton and 4.8 mm for the triton. This compares to the Monte Carlo which gives 16.4 mm and 5.2 mm. Since the two programs use the same stopping power data, and since the algorithm for determining the range is rather straightforward, it is not known why there would be a discrepancy in the value for the triton. In order to account for the discrepancy, the Monte Carlo was rerun with the triton range set at 4.8 mm. Energy deposited as a function of distance was changed by rescaling all triton distances linearly so that the maximum range was 4.8 mm instead of 5.2 mm.

With the ranges unchanged from their amounts calculated in the Monte Carlo, the result was $\overline{E}_{dep} = 491.38 \pm 0.08$ keV and $\sigma_{Edep} = 203.11 \pm 0.07$ keV. With the ranges forced to values that are output by SRIM, the result was $\overline{E}_{dep} = 494.82 \pm 0.08$ keV and $\sigma_{Edep} = 203.226 \pm 0.070$. This corresponds to a variation in $\overline{E}_{dep}$ of $\pm$ 0.7 %.

Another uncertainty related to the range of the ions is introduced by straggling. According to the data in table 3.2, the proton's and triton's range are uncertain due to straggling by about 5 and 8% respectively. This effect was not studied for reasons mentioned on page 70, and since the uncertainty in σ_{Edep} is not of importance.

uncertainties in the SRIM data

The primary source of data for this Monte Carlo was the SRIM simulation package. There is a wealth of experimental data that have been compared to the SRIM calculations [63]. For protons and tritons in helium, the average deviation of the calculations from these data is 5.2%. For protons and tritons in nitrogen, the average deviation is 2.9%. These deviations tend to occur on both sides of the calculation and are at the level of scatter that exists in the data themselves. Furthermore, a large part of the deviations in the helium data are due to some data sets that are in gross disagreement with the other measurements. From these observations, it has been assumed that the SRIM calculations are correct to within 2 %.

gas contents of the monitor, neutron energy

The calculations until now have been done using a monitor that contains 4 % ^{3}He, 46 % ^{4}He and 50 % N_2, with a total pressure of 1 atm at 0° C. The actual contents of the monitors differ from this, however. It was learnt from an LND representative that the pressure to which the monitors are filled is determined by the ambient temperature. Assuming that the monitors were filled indoors, a more likely total content would therefore be 0.9 amagats (an amagat is the density of an ideal gas at STP). A fluctuation of ±10° C could then give rise to a variation of ±3 % in the total gas density of the monitors.

By keeping a constant weighting of 1:1 by number density of helium atoms to nitrogen molecules, and by allowing the total density to vary from 0.86 amagats to 0.94 amagats, $\overline{E}_{dep}$ was found to vary from 459.78 ± 0.06 keV to 478.46 ± 0.06 keV, a variation of ±2 %.

Another possible source of variations in $\overline{E}_{dep}$ is the type of helium that is present. Since higher concentrations of ^{3}He (or lower neutron energies) have a tendency to cause neutron captures to occur closer to the upstream wall, the average deposited energy might change. This effect was investigated. $\overline{E}_{dep}$ of a monitor containing 0.45 amagats of ^{3}He and 0.45 amagats of N_2 was calculated to be 469.32 ± 0.06 keV, using the same seed for the random number generator. $\overline{E}_{dep}$ of a monitor containing 0.03 amagats of ^{3}He, 0.42 amagats of ^{4}He and 0.45 amagats of N_2 was also calculated to be 469.32±0.06 keV. This number corresponds to calculations of a 10 meV neutron. It was also confirmed that varying neutron energy to 100 eV had no effect on $\overline{E}_{dep}$.

3.2.7 The final result

Combining the aforementioned uncertainties in quadrature yields a final value for the uncertainty in $\overline{E}_{dep}$. The average energy deposited per n-^{3}He charge exchange event in the NPDGamma beam monitors is calculated to be $\overline{E}_{dep} = 470 \pm 20$ keV. The standard deviation is $\sigma_{Edep} = 200$ keV and has an uncertainty that is not of importance.

3.3 Beam Monitor Thickness Measurements

3.3.1 Introduction to this section

An important aspect of understanding the NPDGamma beam monitors involves knowledge of the amount of ^{3}He that they contain. The ^{3}He content determines the fraction of the incident beam that the monitors absorb and, if E_{dep} and W are known, allows for an exact conversion of monitor signal to beam flux. A study was therefore carried out to measure the ^{3}He content (also sometimes referred to as the ^{3}*He thickness*) of the beam monitors. This section discusses that study.

The beam monitors can be grouped into three types: those specified at 0.03 atm ^{3}He (the *thin* monitors), those specified at 0.5 atm ^{3}He (the *thick* monitors), and the TRIPLE monitor which was specified at 1 atm ^{3}He. These three types of monitor were treated differently when carrying out this study.

3.3.2 The Method

Since the cross-section of the $n + {}^3$He reaction is large and well determined, a measurement of the beam transmission of the monitors gives a good first estimate of the amount of ^{3}He that they contain.

However, to determine the ^{3}He concentrations from this transmission method alone would impose uncertainties due to the unknown transmission of the aluminum walls and electrodes. This observation is particularly true for the thin monitors, since a significant fraction of their attenuation arises from aluminum, but it is not of serious concern for the other three monitors. Cross-section data were not used to account for the aluminum since the concentrations of a large number of impurities are not predictable.

Ideally, an extra beam monitor would have been made from the same batch as the others, and filled with only nitrogen and ^{4}He. Such an extra monitor does not exist, so a method was developed that allows the ^{3}He content to be measured without having to correct for the aluminum, but which unfortunately still leaves a rather large uncertainty in the case of the thin monitors.

This section on beam monitor thickness measurements is divided into several subsections. First, the method that was used to determine the beam monitor thicknesses is explained in more detail. This method has two separate stages which are introduced in turn. The analysis and results are then discussed. Finally, a second method that determines the ^{3}He content by correcting for the aluminum is used as a consistency check. The aluminum correction is carried out using the measured transmission of a separate block of aluminum alloy.

Stage One: Transmission Measurements

Stage one consists of simply measuring the transmission of neutrons through the beam monitors. These measurements were carried out using the beam monitors themselves, by the method that was described on page 61.

The goal of this stage of the analysis is to divide the transmission of a thick monitor by the transmission of a thin monitor. It is assumed that the thick and thin monitor were made from the same batch of aluminum. This result therefore gives knowledge of what the transmission of the thick monitor would be if everything contained in the thin monitor were to be removed from the thick monitor. Since the two types of monitor are identical in construction except for differing quantities of ^{3}He and ^{4}He, and since ^{4}He has a negligible cross section, the end result of stage one is the transmission of the difference in ^{3}He between the two monitors.

Let the prime denote a thick monitor and let the unprime denote a thin monitor. The quantity that is determined in this stage of the analysis will be referred to as $\widetilde{T_3}$, defined by:

$$\widetilde{T_3} = T_3'/T_3, \tag{3.29}$$

where T_3' is the transmission of one of the 1 cm gaps of ^{3}He of the thick monitor, and T_3 is the transmission of one of the 1 cm gaps of the thin monitor. A transmission measurement is performed of the whole monitor, not of an individual gas gap, but the transmission of a single gap is more convenient for the analysis that follows which makes use of equation (3.30).

Stage Two: Relative Signal Measurements

In stage two, the ratio between the signal strengths of different monitors at the same flux is compared. This comparison is useful since the signal strength has a known dependence on ^{3}He concentration.

An expression for the signal from a beam monitor was derived in section 3.1.4. It was determined that complications from scattering or absorption in the aluminum walls and electrodes are not of importance when comparing the ratios between monitor signals (see page 97). The relevant expression for the pedestal-subtracted signal out of a beam monitor preamplifier then becomes:

$$V = NT_1T_3T_2(1+T_3)(1-T_3)\frac{E_{dep}}{W}eR, \tag{3.30}$$

of which all the parameters were defined in the discussion leading up to equation (3.7).

It is useful to start by assuming that the ^{3}He content of a thick monitor has already been determined and that the ^{3}He content of a thin monitor remains to be determined. Let the voltage signals of the two monitors be normalized to the same beam flux. It follows from equation (3.30) that knowledge of the ratio between thick and thin monitor signals allows for a determination of the amount of ^{3}He in the thin monitor, as expressed by:

$$T_3(1-T_3)(1+T_3) = r\left(\frac{V}{V'}\right)T_3'(1-T_3')(1+T_3'). \tag{3.31}$$

The factor r, defined by:

$$r = \frac{W}{W'}\frac{E'_{dep}}{E_{dep}}, \tag{3.32}$$

is expected to be close to unity since E_{dep} and W are expected to be the same for the two monitors. When comparing signals from the two beam monitors, the same preamplifier and high voltage setting were used.

Equation (3.31) is not useful on its own, due to the fact that the actual transmission, T_3', of the thick monitor is not known. It is necessary to introduce the analysis from stage one in which the quantity $\widetilde{T_3}$ was determined. Equation (3.31) thus yields:

$$(1-T_3)(1+T_3) = r\left(\frac{V}{V'}\right)\widetilde{T_3}(1-T_3\widetilde{T_3})(1+T_3\widetilde{T_3}). \tag{3.33}$$

From equation (3.33), it is possible to algebraically solve for T_3^2 in terms of known quantities. The positive root of that solution is given by:

$$T_3 = \sqrt{\frac{1 - r(V/V')\widetilde{T_3}}{1 - r(V/V')\widetilde{T_3}^3}}. \tag{3.34}$$

It is therefore possible to determine T_3. Once T_3 has been determined, determination of T_3' is a matter of applying equation (3.29).

3.3.3 The Setup

Figure 3.9 shows the setup that was used to make the monitor thickness measurements. Up to three beam monitors were placed in the beam at once, and data were recorded from all of them. These measurements were made in the NPDGamma experimental cave on Flight Path 12 at LANSCE. During these measurements, the locations and properties of the preamplifiers were left unchanged while the beam monitors were switched in and out of the three positions.

Since the frame overlap chopper was not in use for this analysis, a thick monitor was used at position 1 for all of the measurements. Half of an atmosphere of ^{3}He at 20 °C absorbs 90 % of overlapping neutrons at 30 ms after t-zero. Since the signal that is analyzed is the signal from the monitor at positions 2 or 3, this measure simplifies the analysis at long times of flight where the contribution from overlapping neutrons is small.

To convert the monitor signals into ^{3}He concentrations, it is necessary to know the distance to the source from the monitor that is producing the signal. Measurements were therefore made of the positions of the monitors relative to each other and to the end of the neutron guide. These measurement are illustrated and recorded in figure 3.9.

The frame overlap chopper was not in use for the monitor thickness measurements. As a result, the correspondence between time of flight and energy is only applicable when the contribution to the signal from the low energy overlap is small. In order to deal with this situation, a thick monitor was used at position 1 in figure 3.9 at all times. Since low energy neutrons are preferentially absorbed in the monitors, this measure limited the overlap visible at positions 2 and 3 to short times of flight. The longer times of flight were then made use

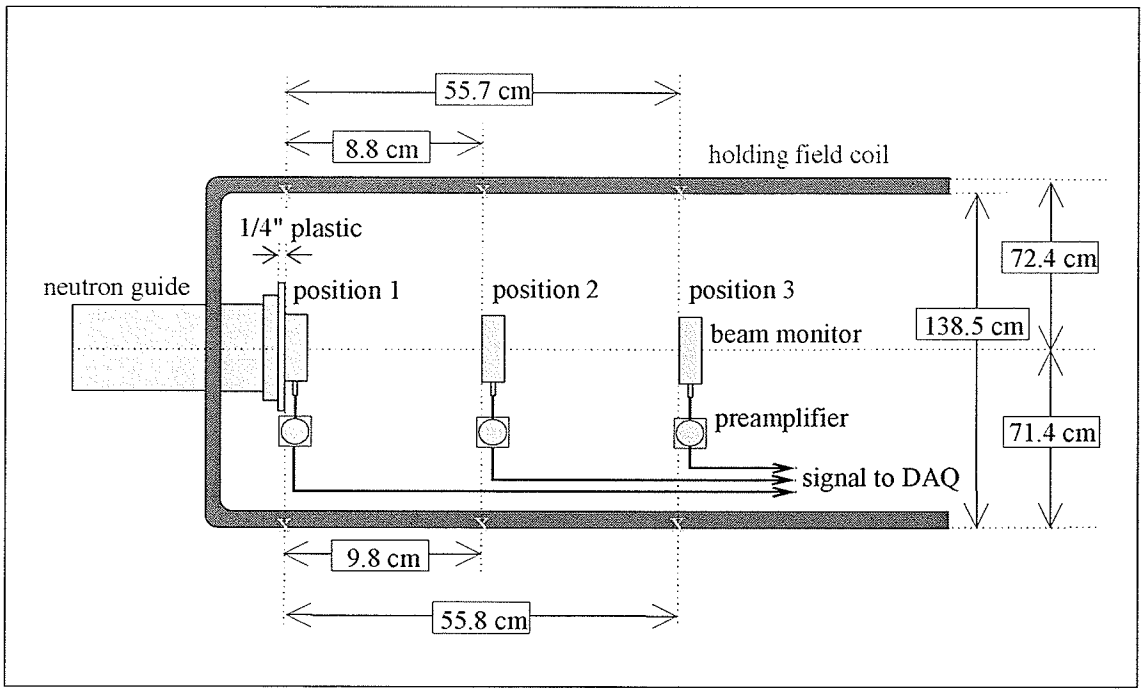

Figure 3.9: The monitor thickness measurements setup. The position of the face of each monitor was extended sideways using a straight edge and marked on either side of the holding field coils, at the locations marked by an x. The straight edge used was the flat side of a bubble level. The distance from the source to the end of the beam guide is 21.00 meters. Since the frame overlap chopper was not in use for this analysis, a thick monitor was used at position 1 for all of the measurements.

of by setting the 10 ms break in data acquisition (see page 59) to occur in the time of flight range from 48.0 ms to 8.0 ms. Data were therefore taken in the range from 8.2 ms to 47.8 ms.

The position of each monitor is given by the position of its collection electrode. All of the monitors (except the TRIPLE monitor, but this is irrelevant to the analysis) are 2 inches thick, and the collection electrode is in the center of the monitor. The monitor position data can thus be condensed from figure 3.9 to table 3.3. The uncertainties in these positions are assumed small enough that they can be ignored without any effect on the final result.

monitor	distance (m)
M1	21.04
M2	21.13
M3	21.60

Table 3.3: The beam monitor position data condensed from diagram 3.9. Distances shown are from the moderator to a monitor's collection electrode.

Stage One: Transmission Measurements

Since Flight Path 12 views a pulsed beam, it is possible to measure the transmission of the beam as a function of time of flight. Given the measured transmission of some ^{3}He, it is thus possible to fit the data to an expected theoretical curve and extract the total areal density of the ^{3}He.

The ^{3}He cross section for low energy neutrons is known to be inversely proportional to neutron speed v, with a proportionality constant that is experimentally well determined (see section 3.1.2). The neutrons that are viewed by the NPDGamma apparatus are of sufficiently low energy for the cross section to show this energy dependence in all time bins except the first (neutrons that arrive in the second time bin already have energies of less than 15 eV). Since velocity is proportional to time of flight t, and since beam transmission T decays exponentially with increasing cross section σ, the logarithm of the transmission of ^{3}He increases linearly with time of flight. These concepts are expressed in equations (3.35) to (3.37).

$$\sigma \propto t \tag{3.35}$$

$$T = exp(-n\sigma) \tag{3.36}$$

$$ln(T) = -n\sigma \propto t \tag{3.37}$$

With the monitors at positions 1 and 3 (see figure 3.9) left unchanged, data runs were taken with and without the middle monitor in the beam. This procedure is carried out according to the method for transmission measurements that is explained in section 3.1.8.

The arrangements that were used are shown in table 3.4.

run number	position 1	position 2	position 3
1319	**prototype**	*54*	*55*
1340	**prototype**	air	*55*
1309	**53**	*55*	*54*
1291	**53**	air	*54*
1313	**prototype**	**53**	*55*
1340	**prototype**	air	*55*
1289	**53**	**prototype**	*54*
1291	**53**	air	*54*
1279	**53**	**TRIPLE**	*54*
1291	**53**	air	*54*

Table 3.4: Data-taking arrangements for stage one of the method. Data runs for this stage were taken in pairs. The first run of each pair has a monitor at position 2 for which the transmission is being determined. For the second run the monitor at positon 2 is removed. The signal at position 3 therefore changes as determined by the attenuation of the monitor at position 2. The positions are as shown in figure 3.9. Thick monitors are indicated by bold type and thin monitors are indicated by italics. The descriptors 53, 54 and 55 are the last two digits of a monitor's serial number, as shown in table 3.1. Pedestal runs were also taken. Pairs of monitor transmission runs (for example runs 1313 and 1309) were also used to determine the relative transmission of two monitors. The results of these measurements are shown in table 3.6

The aluminum also contains materials that have absorption cross sections, which are similarly proportional to time of flight. For low energies, the absorption cross sections dominate. At higher energies, attenuation in the aluminum is dominated by scattering, which is roughly independent of energy. Bragg scattering, enhanced attenuation that occurs at specific times of flight, is also present in the aluminum transmission spectrum.

Stage Two: Relative Signal Measurements

With the monitor at position 1 left unchanged, the monitor at position 2 was switched. The two separate signals at position 2 were then compared to each other by normalization to the signal at position 1, hence yielding V/V' from equation (3.34). Table 3.5 shows the arrangements under which data were taken during this stage of the measurements.

run number	position 1	position 2	position 3
1319	**prototype**	*54*	*55*
1313	**prototype**	**53**	*55*
1324	**prototype**	*55*	air
1313	**prototype**	**53**	*55*
1309	**53**	*55*	*54*
1289	**53**	**prototype**	*54*

Table 3.5: Data-taking arrangements for stage two of the method. Data runs were again taken in pairs. The beam monitor at position 2 is changed in order to observe the relationship between the signal in a thick monitor and the signal in a thin monitor. The monitor at position 3 is irrelevant. The monitor at position 1 is also not of importance, provided it is not changed between the two measurements. The positions are as shown in figure 3.9. Thick monitors are indicated by bold type and thin monitors are indicated by italics. The descriptors 53, 54 and 55 are the last two digits of a monitor's serial number, as shown in table 3.1.

It is important to note that the relative signal measurements, which were made using monitors at position 2, are viewed at a different distance from the source than the transmission measurements, which were made using monitors at position 3. For a given time of flight, the cross section that determines the measured V/V' is therefore different than the cross section that determines the measured $\widetilde{T_3}$.

When analyzing the measurements of $\widetilde{T_3}$ for comparison to V/V' via equation (3.34), $\widetilde{T_3}$ was therefore adjusted to the value that would be viewed at position 2. $\widetilde{T_3}$ at position 2 is slightly larger than at position 3, as determined by the dependence of σ on L that is given

in equation (3.3).

3.3.4 The Analysis

Stage One: Transmission Measurements

During this stage of the analysis, the transmission of each of the beam monitors was determined individually.

It is also worth noting that the data shown in all of the monitor thickness measurements are averaged over a small number (tens) of beam pulses. Statistical variations in the signal are more important than systematic variations. The error bars shown in the plots of data from monitor thickness measurements are therefore entirely statistical.

Figure 3.10 shows a plot of the logarithm of the measured transmission of one of the thin monitors. This measurement includes the transmission of the aluminum electrodes and walls.

Figure 3.11 shows a plot of the logarithm of the measured transmission of one of the thick monitors. Shown is the transmission of the monitor as a whole, as well as the transmission with the contents of a thin monitor removed.

Similar linear fits were carried out for all of the transmission measurements that are shown in table 3.4. The results of these measurements are summarized in table 3.6.

Stage Two: Relative Signal Measurements

$\widetilde{T_3}$ and V/V' having been measured, it is possible, by assuming a value of r and by applying equations (3.29) and (3.34), to determine the thicknesses of both thick and thin monitors.

Propagation of uncertainties will now be discussed. Since the uncertainties in $\widetilde{T_3}$, V/V' and r are uncorrelated, the uncertainty in T_3 can be expressed using equations (3.38) to (3.42) where $S = r\,(V/V')$. Equation (3.38) follows from equation (3.34), and equation (3.40) follows from the assumption that r is approximately unity.

$$\delta T_3^2 = \left(\frac{\partial T_3}{\partial S}\right)^2 \delta S^2 + \left(\frac{\partial T_3}{\partial \widetilde{T_3}}\right)^2 \delta \widetilde{T_3}^2 \tag{3.38}$$

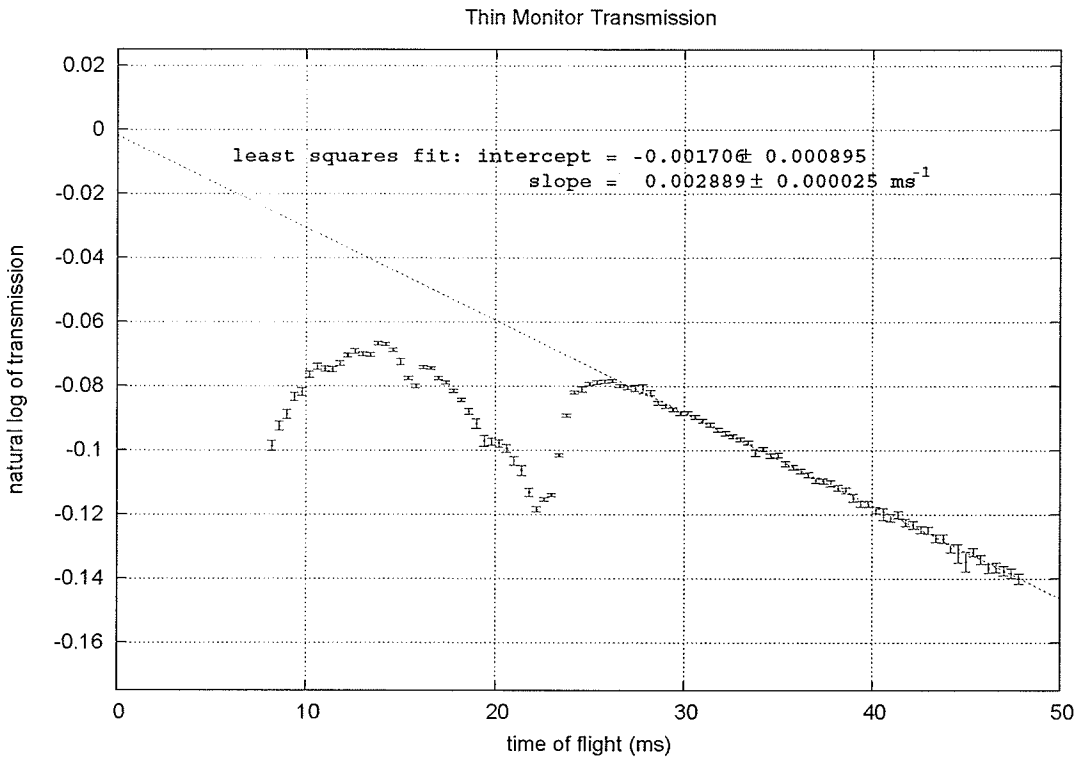

Figure 3.10: The transmission measurement of a thin monitor, from stage one of the thickness measurements. This thin monitor is serial number 084154. The slope and intercept are for a least squares fit to the data beyond a time of flight of 29 ms. The drop in transmission at 22 ms arises as a result of Bragg scattering from the aluminum windows. The frame overlap chopper was not in use when these data were taken.

$$\left(\frac{\delta S}{S}\right)^2 = \left(\frac{\delta r}{r}\right)^2 + \left(\frac{\delta\left[V/V'\right]}{\left[V/V'\right]}\right)^2 \tag{3.39}$$

$$\delta T_3^2 = \left(\frac{\partial T_3}{\partial S}\right)^2 \left(\delta\left[\frac{V}{V'}\right]\right)^2 + \left(\frac{\partial T_3}{\partial \widetilde{T_3}}\right)^2 \delta\widetilde{T_3}^2 + \left(\frac{\partial T_3}{\partial S}\right)^2 \left(\frac{V}{V'}\right)^2 \delta r^2 \tag{3.40}$$

$$\frac{\partial T_3}{\partial S} = \frac{\widetilde{T_3}^3(1 - S\widetilde{T_3}) - \widetilde{T_3}(1 - S\widetilde{T_3}^3)}{2T_3(1 - S\widetilde{T_3}^3)^2} \tag{3.41}$$

$$\frac{\partial T_3}{\partial \widetilde{T_3}} = \frac{3S\widetilde{T_3}^2(1 - S\widetilde{T_3}) - S(1 - S\widetilde{T_3}^3)}{2T_3(1 - S\widetilde{T_3}^3)^2} \tag{3.42}$$

$\delta\left(\widetilde{T_3}^4\right)$ was determined using the linear fits that are recorded in table 3.6. An extra 1% is added in quadrature to the relative uncertainty of $ln\left(\widetilde{T_3}\right)$. This additional uncertainty in

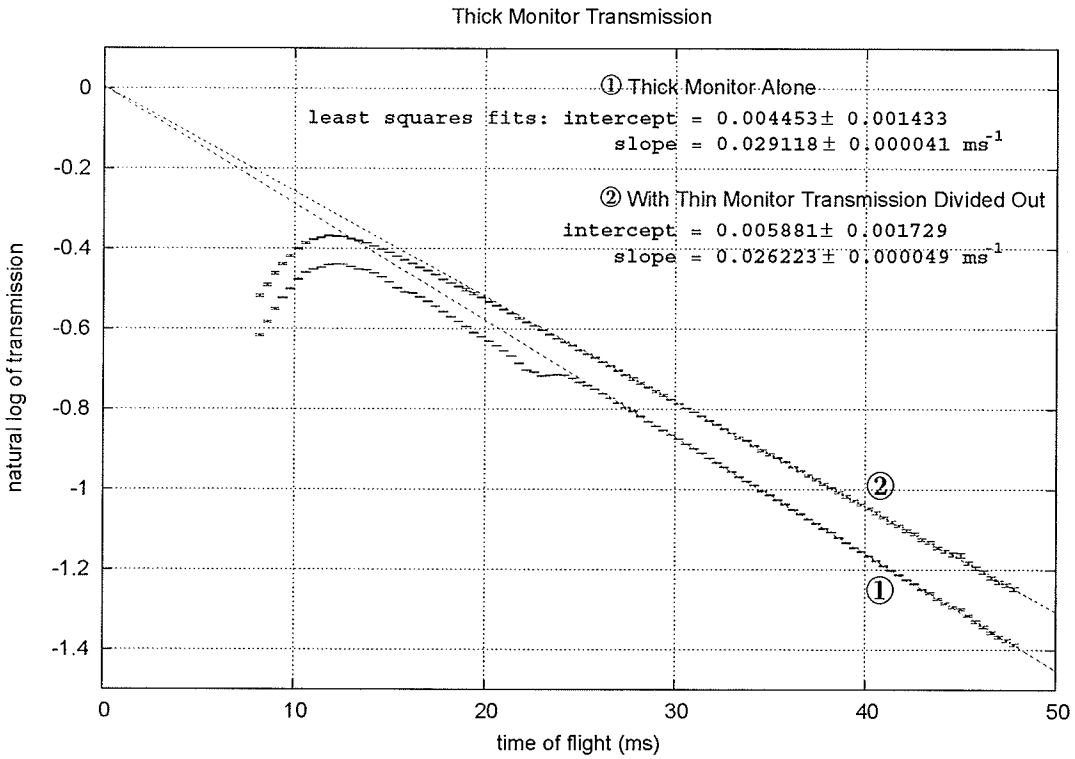

Figure 3.11: The transmission measurement of a thick monitor, from stage one of the thickness measurements. This thick monitor has serial number 084153. The first curve shows the transmission data for the thick monitor alone. The second curve shows the transmission of the thick monitor, divided by the transmission of a thin monitor. This thin monitor has serial number 084154, and its data used here are the same as those shown in figure 3.10. The linear fits were for times of flight greater than 29 ms. The frame overlap chopper was not in use when these data were taken, which explains the deviation from the straight line at short times of flight. Structures common to the transmission spectra for the two monitors, such as enhanced attenuation due to Bragg scattering in the aluminum, are not present in the ratio, justifying the assumption that the two monitors are made from the same batch of material.

$\widetilde{T}_3$ arises due to the fact that the spacing of the electrodes might not be uniformly divided over the width of the monitor. The ratio $[V/V']$ is determined time bin by time bin, directly from the beam monitor voltage measurements.

The factor r is assumed to be close to unity since the stoichiometric makeup by chemical element is assumed to be similar for any two chambers (the TRIPLE monitor is not involved

item 1	item 2	intercept	slope (ms^{-1})	χ^2/d.o.f.
54	air	-0.0017 ± 0.0009	-0.00289 ± 0.00003	0.6
55	air	0.0076 ± 0.0050	-0.00327 ± 0.00014	2.0
53	air	0.0045 ± 0.0014	-0.02912 ± 0.00004	0.7
53	*54*	0.0059 ± 0.0017	-0.02622 ± 0.00005	0.5
53	*55*	-0.0056 ± 0.0040	-0.02578 ± 0.00011	1.6
53	**prototype**	0.0040 ± 0.0041	-0.00140 ± 0.00012	1.4
prototype	air	-0.0024 ± 0.0044	-0.02765 ± 0.00013	1.5
prototype	*54*	-0.0003 ± 0.0038	-0.02477 ± 0.00011	1.3
prototype	*55*	-0.0099 ± 0.0050	-0.02438 ± 0.00015	0.2
TRIPLE	air	-0.0220 ± 0.0073	-0.05429 ± 0.00022	1.3

Table 3.6: A summary of beam monitor transmission measurements. Columns 3 and 4 show the results of a linear least squares fit to the natural logarithm of the transmission. The transmission of item 2 was divided out from the transmission of item 1. Thick monitors are indicated by bold type and thin monitors are indicated by italics. The descriptors 53, 54 and 55 are the last two digits of a monitor's serial number, as shown in table 3.1. Because of the quality of the fits, the uncertainties in these results are determined from the fits themselves. Slopes corresponding to pure ^{3}He can be converted to a ^{3}He areal density using equation (3.3), and the M3 distance provided in table 3.3.

in the relative signal analysis). However, it is understood that the contents of the chambers vary, and as such, r will vary. This variation in r is due separately to variations in W and in E_{dep}.

The W value of a mixture of gases can be determined as a weighted average of the individual values W_i of its n constituents:

$$W = \frac{\sum_i^n f_i P_i W_i}{\sum_i^n f_i P_i}, \tag{3.43}$$

where P_i is the partial pressure of the i^{th} constituent, and f_i is a weighting factor [66]. A large contribution to the variation in the gas contents is assumed to be due to variations in

the ambient temperature at the time of filling. Since the density of an ideal gas at constant pressure is proportional to temperature, a change in temperature will affect the total gas density but will not affect the fractional representation of constituent densities. As a result, variations in temperature at the time of filling are not expected to affect W to a large extent. However, variations in W may be caused by inconsistencies at the time of filling. Assuming the values of 42.7 eV for He and 36.5 eV for N_2 that are given on p. 42 of [59], assuming that f_i is on the order of unity, and assuming that variations in partial pressures are not greater than 5 %, this gives rise to an uncertainty in W/W' that is around ± 4 %.

Not all of the uncertainties in the E_{dep} calculation need to be considered for an uncertainty in E_{dep}/E'_{dep}. This is because some sources of uncertainty such as the existence of the high voltage are expected to contribute equally for both monitors. The only sources of uncertainty that are related to variations from monitor to monitor are the placement of the electrodes and the total pressure. The uncertainty in E_{dep}/E'_{dep} was thus assumed to be 3 %. Adding the uncertainties for W/W' and E_{dep}/E'_{dep} in quadrature, the relative uncertainty $\delta r/r$ is 0.04.

The results from application of equations (3.29) and (3.34) are recorded in table 3.7. The ^{3}He contents are averages that were calculated over 47 time bins from 29.0 ms to 47.8 ms. The relative uncertainty over this range was constant and the variations in T_3 and T'_3 were small compared to the uncertainties. The uncertainties from time bin to time bin are not independent of each other so were not reduced during the averaging.

3.3.5 The transmission of aluminum

The ^{3}He contents of the beam monitors have now been measured using a combination of transmission and relative signal measurements. In this second method, the transmission of an aluminum block is used to correct for the portion of the monitor's transmission that arises from the aluminum, and thus to verify the accuracy of the analysis in section 3.3.4.

The same setup that is displayed in figure 3.9 was used for this measurement, with the monitor at position 2 replaced by a 1.035" wide block of 6061 aluminum alloy. The block had 6061 stamped on it, by the manufacturer or distributor. The width of the block was

thin monitor	^{3}He content (10^{22} m^{-2})	slope at M3 (ms^{-1})	thick monitor	^{3}He content (10^{22} m^{-2})	slope at M3 (ms^{-1})
54	1.01 ± 0.07	0.00055	**53**	13.1 ± 0.1	0.00710
55	0.99 ± 0.07	0.00054	**53**	12.8 ± 0.1	0.00699
55	0.99 ± 0.07	0.00054	**prototype**	12.2 ± 0.1	0.00664

Table 3.7: The ^{3}He contents of the NPDGamma beam monitors from a combination of transmission and relative signal measurements. Each row of this table corresponds to a pair of monitors that was used in one set of relative signal measurements. The ^{3}He contents are areal number densities for one gap between electrodes (specified at 9.9 mm wide). The areal densities are calculated using the transmissions T_3 and T_3'; the known distance of M2 from the source; and equation (3.3). The slope at M3 is calculated using equation (3.3) and the M3 distance, and is shown for comparison with table 3.6. Monitors 55 and 53 are listed twice since, as a consistency check, their signals were compared to more than one monitor (in the case of monitor 55, the result ended up being the same). Note that one mole of ideal gas at 0 °C has a number density of 2.687×10^{25} atoms/m^3 per atmosphere.

determined to be uniform using a pair of calipers. The result of this measurement is shown in figure 3.12.

The measurement in figure 3.12 corresponds to a distance from the source of 21.60 m, the same as for the measurements recorded in tables 3.6 and 3.7. Table 3.8 shows the transmission measurements from table 3.6 corrected for the presence of the aluminum. The corrected data were arrived at by subtracting a fraction 0.133 of the aluminum slope from the monitor slope. The factor 0.133 corresponds to the ratio between the total width of aluminum in a beam monitor and the width of the block.

In table 3.8, the aluminum-corrected data are compared to the relative signal data from table 3.7. The comparison demonstrates good agreement between the two sets of results. It was concluded that the composition of the block corresponds well to the composition of the aluminum in the monitors.

A discrepancy exists in table 3.8 between the second and third columns for monitor 55.

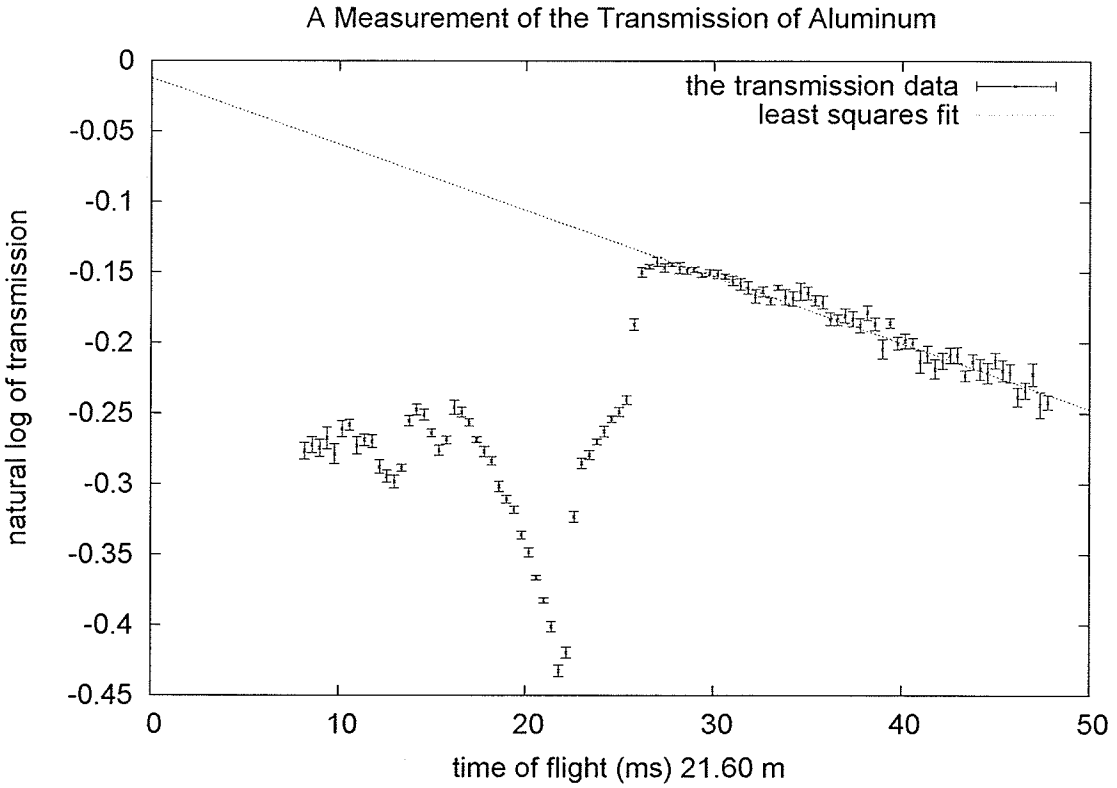

Figure 3.12: A transmission measurement of a 1.035" wide block of 6061 aluminum alloy. A fit to the data at times of flight greater than 29 ms gives $ln(T) = -(0.0047 \pm 0.0001)\,(t/\text{ms}) - (0.012 \pm 0.005)$ with reduced $\chi^2 = 1.7$. The frame overlap chopper was not working when this measurement was made. The large dip at 22 ms occurs due to enhanced attenuation as a result of Bragg scattering from the crystalline aluminum. A Bragg edge at the same time of flight is visible due aluminum in the flight path, as shown in figure 3.15.

Due to the fact that its aluminum-subtracted attenuation is bigger, it seems that monitor 55 has a higher ^{3}He content than monitor 54. In such a case, it is still possible for monitor 53 and monitor 54 to have similar flux-normalized signals if monitor 55 contains less nitrogen.

The uncertainty associated with excluding T_2 from equation (3.7) was then considered. Using values that have now been measured ($T_3 = 0.974$, $T_3' = 0.711$, $T_2 = 0.991$ and $V/V' = 0.142$ for monitors 54 and 53 at 47 ms), equation (3.31) with T_2 included was solved using Newton's method. The result for T_3 differed from the previously recorded

monitor	relative signal	aluminum subtracted
54	0.55 ± 0.04	0.56 ± 0.01
55	0.54 ± 0.04 0.54 ± 0.04	0.66 ± 0.03
53	7.10 ± 0.05 6.99 ± 0.05	7.12 ± 0.01
prototype	6.64 ± 0.05	6.76 ± 0.03
TRIPLE	not applicable	13.41 ± 0.05

Table 3.8: A comparison of two methods that were used to determine the ^{3}He content of the beam monitors. The data shown are the slopes seen at 21.60 m from the source (the M3 distance), in units of s^{-1}. The first data column shows the results from table 3.7, which were determined using the relative signal measurements. The second data column shows the results of the aluminum correction to the transmission measurements. The uncertainties shown in the second data column are entirely statistical and do not take into account uncertainties associated with unknown impurities in the aluminum. The agreement is good (except perhaps for monitor 55), and thus it is concluded that the aluminum block is of similar composition to the aluminum in the monitors. Note that an ideal gas at 0°C has a number density of 2.687×10^{25} atoms/m^3. For a 9.9 mm wide gap at 21.60 m from the beam source, this corresponds to a slope of 14.4 s^{-1}.

value by less than a tenth of a percent. This conclusion was verified to be independent of whether T_2 is caused by absorption or scattering. Ignoring T_2 was therefore justified.

3.3.6 Summary

Table 3.9 shows a summary of the results of the beam monitor thickness measurements. In arriving at this table, the relative signal results were used. For monitor 53, the average of the two results was taken, but the uncertainty was not reduced.

The relative signal method was not used for the TRIPLE monitor since doing so would require a more detailed knowledge of W/E_{dep} for the different gas mixtures. However, since

the TRIPLE monitor contains a large amount of ^{3}He, its transmission is not affected greatly by the aluminum that it contains. It is thus possible to use transmission measurements alone to determine its ^{3}He content. The amount of aluminum was assumed the same as the amounts in the other four monitors, and an uncertainty was added that corresponds to the transmission of this same amount of aluminum.

By comparing tables 3.9 and 3.1, it is possible to compare the specified and measured ^{3}He contents. Monitor 53 and the prototype have a partial pressure of approximately half an atmosphere of ^{3}He at room temperature, and the TRIPLE monitor contains approximately one atmosphere at room temperature. Furthermore, variations in the contents of these three monitors are around what one would expect from variations in temperature at the time of filling. The thin monitors, however, have a measured content that is 30 % higher than the specified content. It is possible that a limitation of the filling valve or pressure gauge does not allow for accurate filling of low pressures.

If similar beam monitors are ordered in the future, and if precise knowledge of the contents is desired, it is recommended to 1) order an extra monitor of identical construction that contains only nitrogen and ^{4}He; and 2) explicitly specify the contents to the manufacturer in units of a number density. Also, it should be kept in mind that a large portion of the uncertainty from the relative signal measurements arises from the fact that the nitrogen content has not been measured.

	^{3}He content		
monitor	relative signal	aluminum corrected	specified
54	1.01 ± 0.07	1.03 ± 0.02	0.73
55	0.99 ± 0.07	1.21 ± 0.06	0.73
53	12.98 ± 0.09	13.07 ± 0.02	12.53
prototype	12.23 ± 0.09	12.41 ± 0.06	12.53
TRIPLE	not applicable	24.7 ± 0.2	25.1

Table 3.9: A summary of the beam monitor thickness measurements. Shown is the content of one 9.9 mm gap of gas in units of (10^{22} atoms ^{3}He)m^{-2}. The first data column shows the measurements that were made using a combination of transmission and relative signal measurements. The second data column shows the results of a separate method that corrected the transmission of the monitors with the transmission of a separate block of aluminum. Except for the entry corresponding to the TRIPLE monitor, the uncertainties in the second data column are entirely statistical. The third data column shows the specified contents as a number density in the same units, corresponding to the pressures in table 3.1 at a temperature of 20 °C.

3.4 Beam Flux Measurements

3.4.1 Beam monitor calibration

Given equation (3.7), it is possible to convert a beam monitor signal into a measurement of beam flux. However, in order to do so, some of the quantities shown in equation (3.7) must be experimentally verified. By viewing the monitor signal under known conditions, it should be possible to determine these quantities and thus to provide a calibration of the monitor.

The original intention was to calibrate the NPDGamma beam monitors at a source of calibrated neutron flux, e.g. at the National Institute of Standards and Technology in Gaithersburg, Md. However, since an absolute calibration of the beam monitors is not important to meet the goals of the NPDGamma experiment, and due to time and budgeting constraints, this option was not pursued.

This section discusses an attempted absolute calibration of M1 using another method. M1 is used since it is mounted directly on the end of the beam guide and therefore sees the entire beam as it exits from the guide, uncollimated and unattenuated. The calibration is carried out by comparing the M1 signal to a Monte Carlo calculation of the absolute flux from the beam guide. A surprising discrepancy remains, however, between the resulting calibration and the expected values of E_{dep}, W and T_3. This discrepancy is particularly surprising since a calibration was performed using a ^{6}Li-doped scintillation counter at another beamline (Flight Path 11 at LANSCE) in 2001 with the prototype monitor and no such discrepancy was observed [67].

The neutrons for the NPDGamma experiment are created when the 800 MeV proton beam, which arrives from the LANSCE storage ring in 250 ns wide pulses at 50 Hz, strikes a tungsten spallation target. The high energy neutrons from this reaction are slowed by backscattering from a liquid hydrogen moderator. Assuming constant spallation target characteristics, constant moderator properties, constant beam transport characteristics, and constant proton energy, the beam flux that is incident on a monitor is expected to be proportional to the flux of the proton beam that is incident on the spallation target.

The flux of the proton beam (the proton current or I_p) that strikes the spallation target

is measured in units of μA. A pulsed signal of frequency proportional to the proton current is sent from accelerator control and received by the NPDGamma data acquisition system. The proton current signal arrives at a rate of 500 Hz per μA of proton current, and a scaler is used to count proton current pulses for a period of 45 ms per beam pulse. The result is an integer I_{raw} that is stored in the data files, beam pulse by beam pulse, for later use. Conversion of I_{raw} to a current in μA is thus achieved by the following formula:

$$(I_p/\mu A) = \frac{I_{raw}}{(500\text{ Hz})(45\text{ ms})}. \tag{3.44}$$

The hypothesis that beam flux is proportional to the proton current signal from the accelerator control room was tested by observing the dependence of the M1 preamplifier voltage V_1 on proton current signal I_p over a range of data runs. M1 was used since it is mounted directly on the end of the beam guide and therefore sees unattenuated beam.

This investigation is summarized in figures 3.13 and 3.14. Figure 3.13 shows V_1 at particular time bins normalized to I_p, plotted versus the run number. Figure 3.14 shows the proton current plotted versus run number. By visually comparing figures 3.13 and 3.14, it can be seen that variations in the normalized M1 signal are uncorrelated with proton current, indicating a nearly linear relationship between V_1 and I_p. The proportionality between V_1 and I_p appears to be good at the level of $\pm 5\%$.

Given this linear relationship, and assuming that it is valid in general, it is possible to compare the predicted flux from the M1 signal to a previous measurement of the beam flux at Flight Path 12. Figure 3.15 shows the M1 signal from run 2995, a typical data run that was randomly chosen for this purpose. M1 is the monitor with serial number 084154.

Equation (3.7) indicates a linear relationship between the beam flux N that is incident on the face of a monitor and the output voltage V of its preamplifier. For the purposes of calibration, equation (3.7) is restated as equations (3.45) to (3.47).

$$V = NQRP \tag{3.45}$$

$$Q = T_1 T_2 e \overline{E}_{dep}/W \tag{3.46}$$

$$P = T_3\left(1 - T_3^2\right) \tag{3.47}$$

Q is ideally independent of the beam monitor, P depends on the monitor's ^{3}He content,

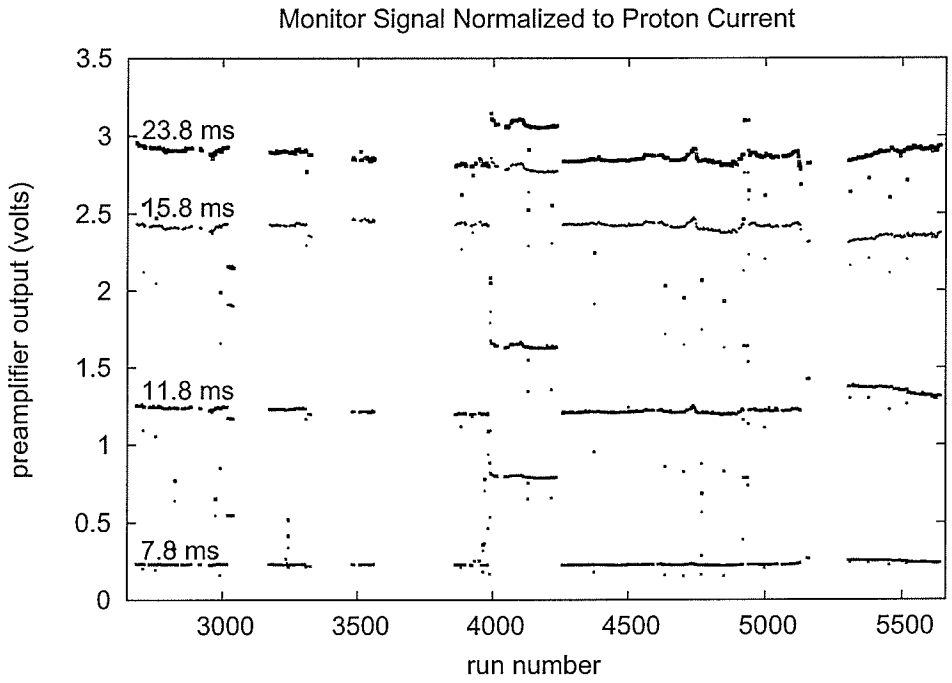

Figure 3.13: Shown plotted in this figure is the M1 signal V (at 21.04 m from the moderator), normalized to 100 μA beam current I_p (plotted is $V/I_p \times 100\mu$A), at four different time bins, over a range of data runs. The same preamplifier was used for all of these data runs. This figure shows that V/I_p is stable to within about $\pm$ 5%. The different voltages at different times of flight is explained by the time of flight dependence of the beam flux and of the capture probability in the beam monitors (see figures 2.3, 3.15 and 3.17). The anomaly in the range between run 4000 and run 4250 is explained by the fact that the frame overlap chopper was not working, therefore giving rise to a greater monitor signal, particularly at shorter times of flight. These data runs cover the period of time between March 19$^{\text{th}}$ 2004 and April 21$^{\text{st}}$ 2004.

and R depends on the preamplifier. T_3 and N depend on time of flight while Q and R are independent of time of flight [3]. A factor of T_2 has been ignored in the definition of P since doing so introduces an inaccuracy that is negligible compared to the uncertainties.

[3] E_{dep} was determined in section 3.2.6 to be independent of neutron energy and independent of ^{3}He content. T_1T_2 is roughly independent of time of flight and differs from unity by less than 2 %, introducing negligible uncertainty.

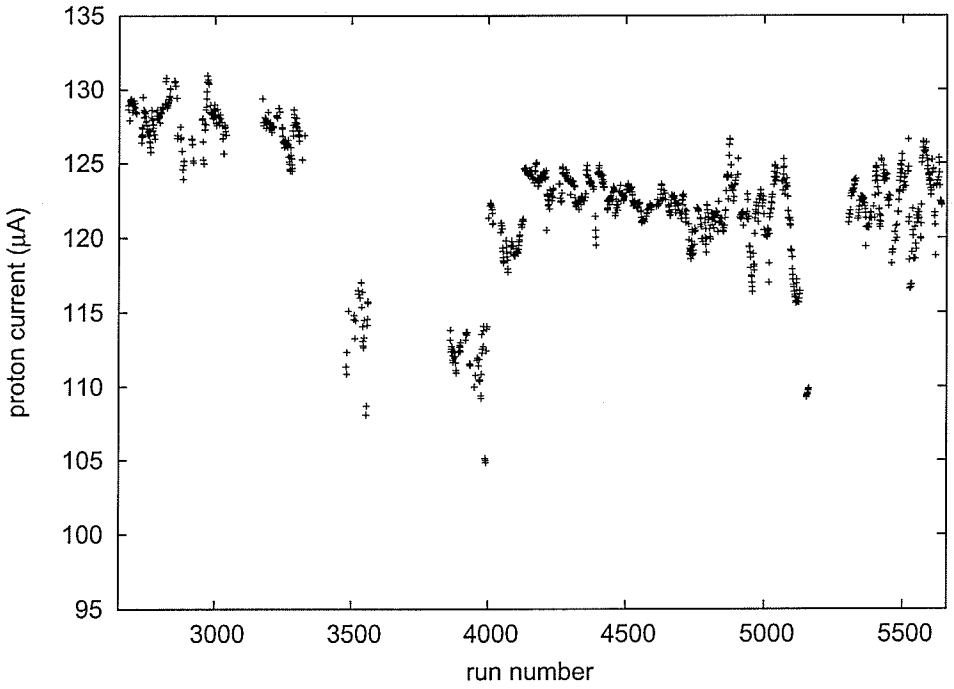

Figure 3.14: Proton current versus run number.

A determination of Q, T_3 and R is thus a calibration of a beam monitor. The monitor-depedent quantity T_3 was determined in section 3.3. The current section deals with the monitor-independent quantities R and Q.

The preamplifier gain R was determined by applying a variable DC voltage v_1 across a known resistance R_S and the preamplifier input as shown in figure 3.16. By measuring v_1,v_2 and v_3 for several values of v_1 with a precision voltmeter, $R = (v_3 - v_2)R_S/(v_1 - v_2)$ was determined to be 5.90 MΩ, and independent of v_1, with negligible uncertainty.

Figure 3.17 shows a conversion of the data from figure 3.15 to beam flux using equation (3.7). To convert V to a quantity that is proportional to beam flux, V is divided by RP. The time of flight dependence of P can thus be observed by comparing figures 3.15 and 3.17. However, the conversion between V/RP and beam flux is undetermined since the scaling factor Q has not been measured.

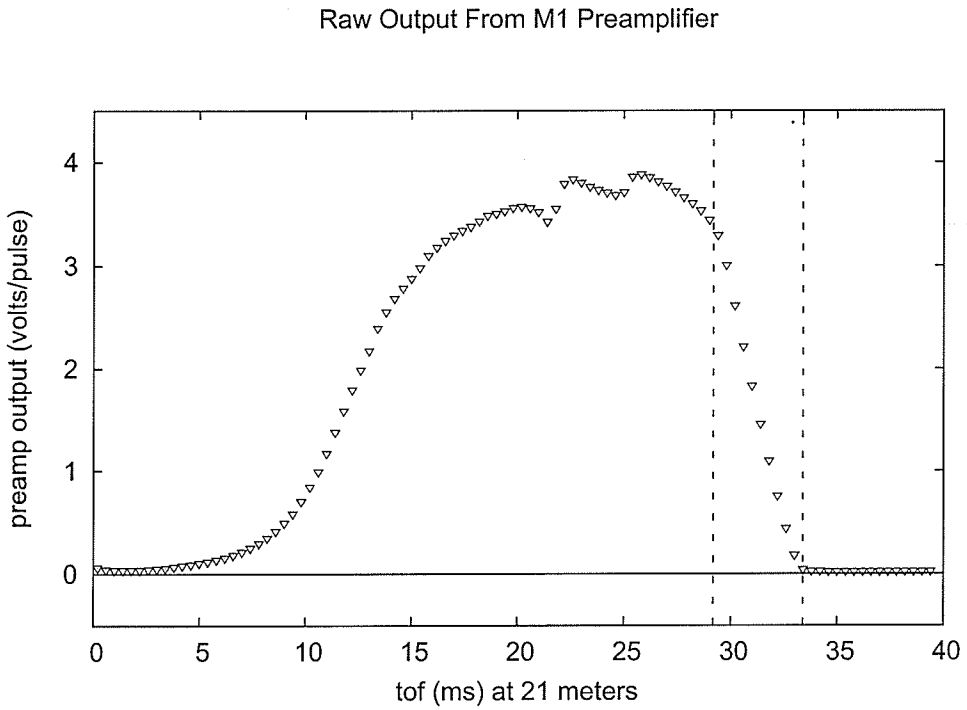

Figure 3.15: Shown plotted in this graph is the raw voltage signal from the M1 preamplifier, for 100 time bins between 0 and 40 ms after the beginning of a beam pulse. These particular data are from run 2995. The signal shown is averaged over 10,000 beam pulses, and so the statistical error bars are too small to show. Drops in the voltage are visible at 21.5 ms and at 24.5 ms. These drops arise from enhanced beam attenuation that is due to Bragg scattering from aluminum in the flight path. Higher order Bragg edges exist at shorter times of flight, but are only visible at higher time resolutions. The front of the blades of the frame overlap chopper can be seen to be sweeping through the beam between the two vertical lines near 30 ms. The proton current had an average value of 129 μA and had a pulse-to-pulse standard deviation of 1 μA during run 2995.

As a determination of Q, the result is compared to a Monte Carlo calculation [41] that is based on an absolute measurement of the beam flux [42]. This earlier measurement was performed using a ^{6}Li-doped scintillation counter (of which the efficiency for neutron capture is known) at a time when only the first 8 meters of beam guide had been installed. The Monte Carlo calculation uses this result to predict the flux at 100 μA proton current after

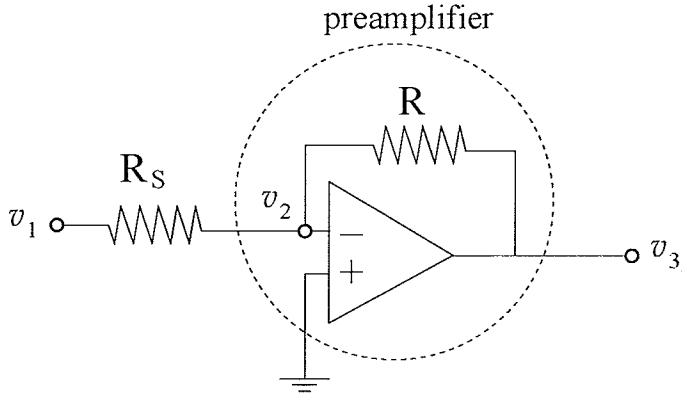

Figure 3.16: A preamplifier gain measurement. The preamplifier of gain R is represented schematically by the components inside the circle. The resistor R_S is of known resistance. The DC voltage v_1 is varied and v_1, v_2, and v_3 are measured.

the beam has passed through the remaining length of the guide. Q can thus be determined by normalizing the monitor signal to 100 μA proton current (by dividing V in figure 3.15 by 1.29), and by then comparing it to the Monte Carlo.

A sample determination of Q is carried out here at 15 ms time of flight. The Monte Carlo predicts $N = 2.8 \times 10^{10}$ neutrons/s. Equation (3.3) provides $\sigma = 8380 \pm 10$ b at the M1 distance of 21.04 m. Thus $P = 0.017 \pm 0.001$ using $n = (1.01 \pm 0.07) \times 10^{22}$ m^{-2} from table 3.9. $V = 2.28$ V from figure 3.15 thus yields $Q = (5000 \pm 700)e$, taking into account an 8 % uncertainty in the ^{6}Li measurement and assuming a 10% uncertainty in the Monte Carlo. Assuming $E_{dep} = 470 \pm 20$ keV and $T_1 T_2 \approx 0.985$, this yields a value for W of 93 ± 14 eV. This value of W is in unequivocal disagreement with the values in the range of 30-40 eV that are quoted in textbooks [59, 64]. An examination of figure 3.17 shows that the discrepancy comes from an overall normalization factor since the shape of the Monte Carlo and the shape of the monitor flux measurement agree. The source of this discrepancy has not yet been determined.

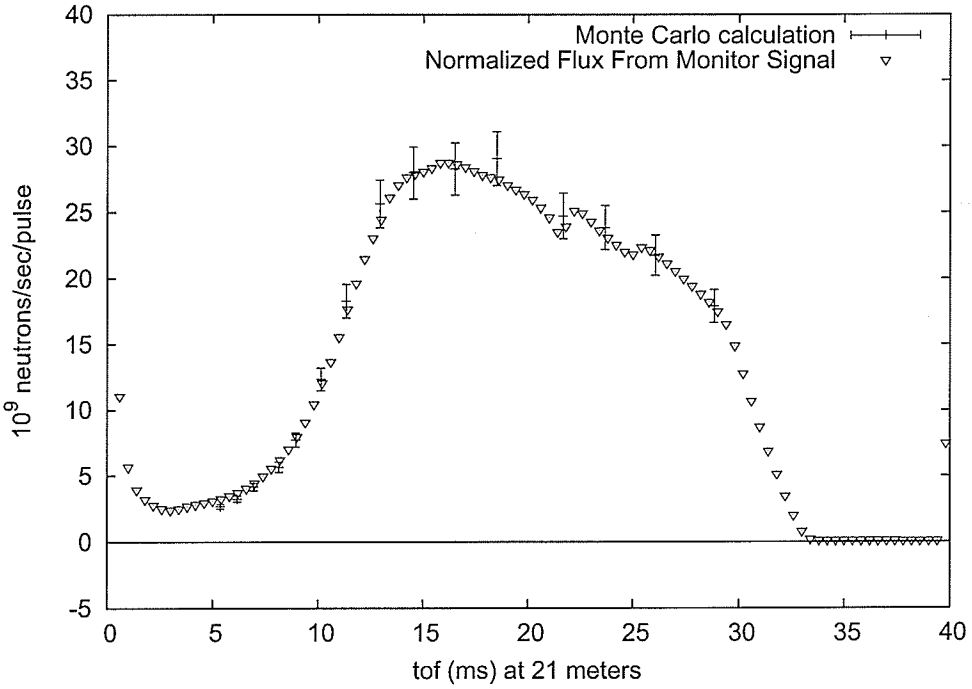

Figure 3.17: Time of flight spectroscopy using M1. The triangular data points are the same data that are shown in figure 3.15, converted to beam flux by application of equation (3.7), and normalized to 100 μA proton current. The data points with error bars are a Monte Carlo calculation [41] that is based on an absolute measurement of the beam flux that was performed during the commissioning of Flight Path 12 [42]. The Monte Carlo was carried out at a proton current of 100 μA. Application of equation (3.45) to the data from figure 3.15 is limited by the existence of the undetermined constant Q. Comparison of the two sets of data yields a determination of Q and hence a calibration of the beam monitors.

3.4.2 Noise in a single beam monitor

Referring to equation (3.7), the signal from a beam monitor preamplifier is proportional to several factors that can be represented as separate sources of noise. The goal of this section is to predict the signal variations that are expected from these sources of noise and to compare this to observation. For the purposes of this section, equation (3.7) is re-expressed

as:

$$V = I_p P_{cap} \frac{\widetilde{E}_{dep}}{W} R. \tag{3.48}$$

where the new quantity P_{cap} will soon be introduced. Contributions to noise will be represented as σ_x to denote the standard deviation of a contributing variable x.

The processes that determine the conversion of a proton from the storage ring to a neutron capture in a beam monitor are statistical in nature and are determined by the number of spallation neutrons created per incident proton; by the probability for scattering from the moderator; by the probability for transmission through the guide and apparatus; and by the probability for capture in the monitor.

As explained in section 3.1.6, the beam monitor voltage signal is stored by the NPDGamma data acquisition after being integrated over each of 100 time bins of 0.4 ms duration. Allow N_{cap} to be defined as the number of neutrons captured during one time bin. The proportionality between I_p and N_{cap} is defined as $P_{cap} \equiv N_{cap}/I_p$. With I_p held constant, $\sigma_{Pcap}/P_{cap} = \sigma_{Ncap}/N_{cap}$. While σ_{Ip} varies from run to run depending on the conditions of the accelerator, σ_{Pcap} is thus determined by counting statistics.

The third factor from equation (3.7) to be considered is $\widetilde{E}_{dep}$: the average energy deposited per neutron capture event for one particular beam pulse at one particular time bin. From neutron capture to neutron capture, the variation in deposited energy is determined by the geometry of the capture region and was calculated in section 3.2. Since the number of neutrons captured during one time bin is finite, the amount of energy deposited in the beam monitors over a given time bin varies from pulse to pulse, even at constant rate of neutron detection. As was discussed in section 3.2, the variation in $\widetilde{E}_{dep}$ is given by $\sigma_{\widetilde{E}dep} = \sigma_{Edep}/\sqrt{N_{cap}}$ where σ_{Edep} is the variation in E_{dep} from neutron to neutron. The average values of $\widetilde{E}_{dep}$ and σ_{Edep} are stated on page 82.

The fourth factor to be considered is W, the average amount of energy required to separate an electron-hole pair in the gas mixture. The variation in W from neutron capture to neutron capture is diminished as a result of the fact that approximately 10^4 ionization events occur per neutron capture (W is approximately 40 eV, and E_{dep} is 470 keV). It is assumed that the variation σ_W from ionization to ionization is not larger than W itself. The

relevant quantity, $\sigma_W/(W\sqrt{N_e})$ where N_e is the number of ionizations per neutron capture, is therefore at least an order of magnitude smaller than σ_{Edep}/E_{dep}.

The final quantity to be considered is R, the gain of the preamplifier. Contributions from this source of noise can be studied by observing the pedestals. The standard deviation in the pedestal at one time bin from pulse to pulse was found to exist at the level of less than 1 mV, which, for signals that are measured in volts, is significantly less than the other variations that are being discussed.

Summarizing the sources of noise that have been discussed, the total variation in a beam monitor signal V is given by:

$$\begin{aligned}\left(\frac{\sigma_V}{V}\right)^2 &= \left(\frac{\sigma_{Ip}}{I_p}\right)^2 + \left(\frac{\sigma_{Ncap}}{N_{cap}}\right)^2 + \left(\frac{\sigma_R}{R}\right)^2 \\ &+ \left(\frac{1}{\sqrt{N_{cap}}}\frac{\sigma_{Edep}}{\overline{E}_{dep}}\right)^2 + \left(\frac{1}{\sqrt{N_{cap}}}\frac{\sigma_W/\sqrt{N_e}}{W}\right)^2 \end{aligned} \tag{3.49}$$

where σ_{Ncap} is given by statistics to be $\sqrt{N_{cap}}$. It is possible to ignore variations in W and R for reasons that are previously discussed. This simplification yields:

$$\left(\frac{\sigma_V}{V}\right)^2 = \left(\frac{\sigma_{Ip}}{I_p}\right)^2 + \frac{1}{N_{cap}}\left(1 + \left(\frac{\sigma_{Edep}}{\overline{E}_{dep}}\right)^2\right). \tag{3.50}$$

Using the values for $\overline{E}_{dep}$ and σ_{Edep} that are stated on page 82, noise intrinsic to the beam monitors is expected to exist a factor of 1.19 above counting statistics (i.e. $1.19/\sqrt{N}$ instead of $1/\sqrt{N}$).

Figure 3.18 shows the variation in the M1 preamplifier signal over a data run of 10,000 beam pulses. The distribution is visibly Gaussian in shape, but has a standard deviation that is larger than would be expected purely from counting statistics and variations in E_{dep}. This larger standard deviation is most likely caused by fluctuations in beam flux throughout the data run. It is not possible to verify that σ_{Ip} accounts for the entire discrepancy since it was not determined how I_p is measured before being sent by the accelerator central control.

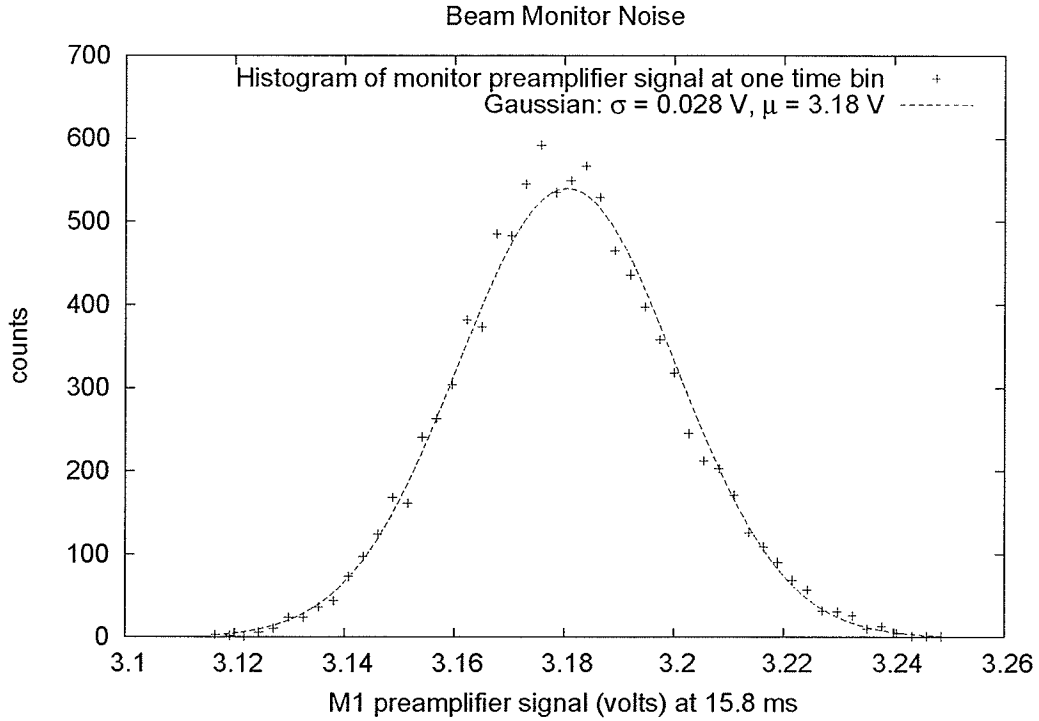

Figure 3.18: A histogram of the M1 preamplifier signal at the time bin that lies between 15.6 and 16.0 ms. Each count corresponds to a voltage that was recorded at that time bin during one of the beam pulses. The entire 10,000 pulses from data run 2317 are histogrammed. Over this data run, the proton current had an average value of 127.7 μA and a relatively small standard deviation of 0.7 μA (this standard deviation cannot be easily compared to the standard deviation on this graph since it is not known how I_p is averaged before being sent as a signal to the NPDGamma data acquisition system).

3.4.3 Noise that is uncorrelated between two beam monitors

By observing the signal from two monitors that are simultaneously in the beam, it is possible to eliminate noise that is common to the two monitors, and that is therefore due to fluctuations in beam intensity. Equation (3.48) can be used to give the ratio between two monitor signals:

$$F \equiv \frac{V_2}{V_1} = \left(\frac{I_{p,2}}{I_{p,1}}\right)\left(\frac{N_{cap,2}}{N_{cap,1}}\right)\left(\frac{\widetilde{E}_{dep,2}}{\widetilde{E}_{dep,1}}\right)\left(\frac{W_1}{W_2}\right)\left(\frac{R_2}{R_1}\right). \tag{3.51}$$

If V_1 and V_2 are always observed during the same beam pulse, then $I_{p,1}/I_{p,2}$ is unity with a standard deviation of zero. Variations in W_1/W_2 and R_1/R_2 will be ignored for reasons that were discussed in section 3.4.2. However, N_{cap} and $\widetilde{E}_{dep}$ will vary independently between the two monitors in a significant way. $\overline{E}_{dep}$ and σ_{Edep} are expected to be the same for the two monitors, so the standard deviation of V_1/V_2 can be represented as:

$$\left(\frac{\sigma_F}{F}\right)^2 = \left(\frac{1}{N_{cap,1}} + \frac{1}{N_{cap,2}}\right)\left(1 + \left(\frac{\sigma_{Edep}}{\overline{E}_{dep}}\right)^2\right) = 1.19\left(\frac{1}{N_{cap,1}} + \frac{1}{N_{cap,2}}\right). \tag{3.52}$$

In this analysis, the signals of M1 and M2 will be studied during the time bin centered at 16.2 ms. The preamp gains of M1 and M2 were measured to be 5.90 MΩ and 5.85 MΩ respectively. Furthermore, during the relative signal analysis, the M1 and M2 signals were found to be virtually indistinguishable with the same preamplifier, beam flux and beam energy. The beam energy that is observed by M2 at 16.2 ms is the beam energy that is observed by M1 at a time that is 0.3 ms (less than the width of a time bin) earlier. This is due to the fact that M1 and M2 are 35 cm apart and the fact that M1 is 21 m away from the moderator. The beam flux does not change significantly over 0.3 ms at 16.2 ms (see figure 3.17), so it is assumed that the following relationship is valid to within 1 %:

$$\frac{N_{0,1}}{N_{0,2}} = \frac{V_1}{V_2}\,, \tag{3.53}$$

where N_0 refers to incident flux.

Over a 0.3 ms time period at around 16.2 ms, the capture probabilities in M1 and M2 do not change by more than 2 %. If N_0 is replaced with N_{cap}, then equation (3.53) is good to within 10 % (due to the uncertainties in table 3.9). With this in mind, equation (3.52) becomes:

$$\left(\frac{\sigma_F}{F}\right)^2 = \frac{1.19}{N_{cap,1}}\left(1 + \frac{V_1}{V_2}\right). \tag{3.54}$$

Allow the subscript 1 to refer to M1 and the subscript 2 to refer to M2. Figure 3.19 shows V_2/V_1 histogrammed from pulse to pulse at the time bin that is centered at 16.2 ms. The 10,000 beam pulses from data run 5639 are histogrammed. Shown also is a Gaussian

with $\sigma = 0.00585$ and $\mu = 0.844$. From this figure, it can be concluded that $V_1/V_2 = 1.18$. From the Monte Carlo that is shown in figure 3.17, from table 3.9, from the proton current of 122 μA, and from equation (3.3), $N_{cap,1}$ is predicted to be 2.5×10^5. From equation (3.54), the predicted noise is therefore $\sigma_F/F = 0.0032$. The observed noise, $\sigma_F/F = 0.0069$, is a bit more than a factor of two larger than this.

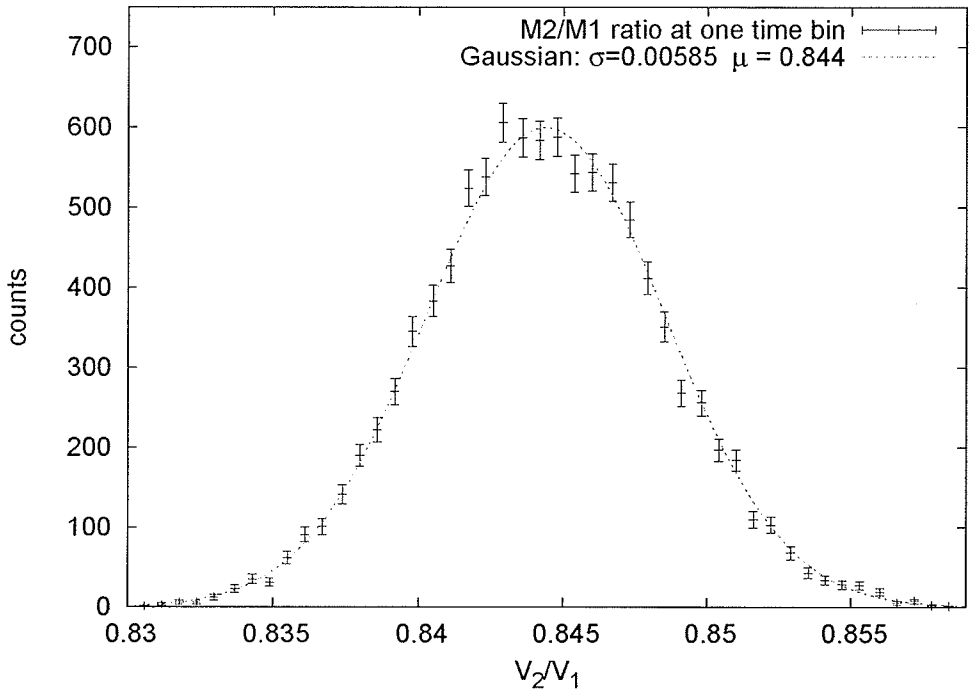

Figure 3.19: A histogram showing noise in the ratio between two beam monitor signals. The M2/M1 ratio at the 13.8 ms time bin was histogrammed for 10,000 beam pulses over data run 5639. During this data run, the polarizer cell was not in the beam, so the difference in M1 and M2 signals arises as a result of attenuation from M1 and the oven walls. Error bars are statistical.

The observed noise is therefore larger than that predicted by counting statistics from the Monte Carlo and by variations in E_{dep}. If the discrepancy in the value of W that is discussed on page 106 is caused by a lower than expected beam flux, then this would account for nearly all of the extra noise. It is also possible that less charge is being collected per neutron than expected. This could occur if the monitors were to contain less nitrogen

than specified. Such a discrepancy would not be observable since nitrogen has a small cross section for interaction with neutrons. In such a case, $\overline{E}_{dep}$ would be smaller than was calculated and σ_{Edep} would be larger than was calculated. This situation would also give rise to higher noise and a smaller observed flux.

By comparing figures 3.18 and 3.19, it can be seen that noise inherently in the beam monitors is smaller than the noise that is inherently in the beam. Furthermore, given the high beam flux, this level of noise is very acceptable.

Chapter 4

BEAM MONITOR POLARIMETRY

4.1 *Introduction to Polarization Measurements*

The neutron beam for NPDGamma is polarized using a ^{3}He neutron spin filter, the concept of which was introduced in section 2.5. The usefulness of this type of beam polarizer arises from the spin-dependent cross section of the n $+^3$ He reaction.

As was discussed in section 3.1.2, the cross-section for neutrons on ^{3}He is very large and almost exclusively passes through the (n, p) channel with 764 keV of kinetic energy released. Due to the fact that the reaction occurs via a $J^\pi = 0^+$ resonance, the cross section is very strongly spin dependent. Both the neutron and the ^{3}He nucleus have total internal angular momentum and parity of $J^\pi = \frac{1}{2}^+$. The n-^{3}He charge exchange reaction therefore only occurs when the two spins are antiparallel.

Due to the tendency for polarized ^{3}He to almost exclusively remove neutrons of one particular spin state from the beam, and to leave neutrons of the other spin state virtually unaffected, polarized ^{3}He is a very effective spin filter [68]. One convenient aspect of these spin filters is that the polarization of an initially unpolarized neutron beam as it exits the filter can be determined by performing transmission measurements on the ^{3}He cell. Furthermore, for diagnostic purposes, the same transmission measurements can be used to determine the polarization of the ^{3}He.

Consider a neutron that will be found to exist in the $|+\rangle$ state. The probability for interaction with a ^{3}He nucleus in the $|+\rangle$ state is assumed to be zero while for a ^{3}He nucleus in the $|-\rangle$ state it is finite. The probability for such a neutron to be transmitted through a volume of ^{3}He is given by:

$$T_+ = exp\left(-n_{-3}\sigma_p\right) = exp\left(-n_3\left(1 - P_3\right)\sigma\right) \tag{4.1}$$

where: $\sigma_p = 2\sigma$ is the cross section for neutron and ^{3}He of opposite spin states; $n_{\pm 3}$ is the areal density of ^{3}He in the $|\pm\rangle$ state; $n_3 = n_{+3} + n_{-3}$; and P_3 is the ^{3}He polarization that is defined by:

$$P_3 = \frac{n_{+3} - n_{-3}}{n_{+3} + n_{-3}}. \tag{4.2}$$

Similarly, the probability for transmission of a neutron that will be found to exist in the $|-\rangle$ state is given by:

$$T_- = exp\left(-n_{+3}\sigma_p\right) = exp\left(-n_3\left(1 + P_3\right)\sigma\right). \tag{4.3}$$

An unpolarized beam is composed 50% of neutrons that will be found to exist in the $|+\rangle$ state and 50% of neutrons that will be found to exist in the $|-\rangle$ state. Equations (4.1) and (4.3) yield a simple expression for the transmission $T_{3,P}$ of an initially unpolarized beam through a region of polarized ^{3}He:

$$T_{3,P} = \frac{T_+ + T_-}{2} = exp(-n_3\sigma)cosh(n_3\sigma P_3). \tag{4.4}$$

An expression for the polarization of the beam downstream of the cell (P_n from equation (2.4)) can be similarly determined:

$$P_n = \frac{T_+ - T_-}{T_+ + T_-} = tanh(n_3\sigma P_3). \tag{4.5}$$

Equation (4.4) for an unpolarized cell is reduced to:

$$T_{3,0} = exp(-n_3\sigma). \tag{4.6}$$

It thus follows that σ is the cross section relevant for describing the transmission of an unpolarized beam through unpolarized ^{3}He. This cross section is therefore the one for which the measurement has been quoted in equation (3.2).

Using the identity $tanh^2x = 1 - sech^2x$, the beam polarization can be expressed in terms of the ratio of transmissions, $T_{3,0}/T_{3,P}$:

$$P_n = \sqrt{1 - \left(\frac{T_{3,0}}{T_{3,P}}\right)^2}. \tag{4.7}$$

Equation (4.7) is useful since it allows for the polarization of the beam to be determined in terms of ratios of transmission probabilities that are measurable using the beam monitors. Furthermore, these beam monitor measurements may be made simultaneously with gamma asymmetry measurements. Despite the fact that the preamplifier gains, the beam flux, the ^{3}He concentration, the ^{3}He cross-section and the ^{3}He polarization all affect measurements that are made individually in the application of equation (4.7), it is not necessary to know any of these quantities to determine beam polarization. It must only be assured that the single quantity that changes between the two measurements is P_3. Furthermore, since the transmissions of any other intervening materials are independent of the ^{3}He polarization, only the factor $T_{3,0}/T_{3,P}$ will survive a ratio between transmission measurements [1].

Some limitations of equation (4.7) should be noted. First of all, it cannot be used if more than one neutron energy is present in the beam at once. Also, transmission measurements can only determine the absolute value of polarization; to determine the sign of the polarization it is necessary to know the helicity of the light that is used to optically pump the rubidium in the cell.

4.2 The Method of a Polarization Measurement

4.2.1 The beam polarization

For regular gamma asymmetry data-taking, the apparatus is set up as shown in figure 2.1. Throughout asymmetry data-taking, beam polarization measurements are made. Photographs of the aspects of the apparatus that are relevant to polarimetry can be found by referring to figures 2.4 and 2.5. A diagram of the materials present in the beam between M1 and M2 during data taking is shown in figure 4.6.

At a time before a series of gamma asymmetry data runs are taken, an initial ^{3}He transmission measurement is made with the polarizer cell unpolarized. $V_{1,0}$ and $V_{2,0}$ are the pedestal-subtracted voltage signals that are obtained from M1 and M2 respectively at this time. Using similar conventions to those used in equations (3.15), these voltages can

[1] It is true that scattering does not cancel perfectly, but it is shown in section 4.4 that this effect is not of significance for NPDGamma polarimetry measurements.

be expressed as given in equations (4.8) and (4.9) where N is the flux incident on M1; $f_1 R_1$ and $f_2 R_2$ are the gains of the two monitor-preamp combinations; α would be the ratio of the two voltages in a situation where the two monitor-preamp combinations are identical and the attenuating materials between them are removed; and $t = T_2 T_4$ where T_2 is the transmission of the oven walls and T_4 is the transmission of the cell walls (see figure 4.6).

$$V_{1,0} = N f_1 R_1 \tag{4.8}$$

$$V_{2,0} = N \alpha t T_{3,0} f_2 R_2 \tag{4.9}$$

At a time after the ^{3}He cell has been polarized, beam polarization measurements are made. Let the pedestal-subtracted M1 and M2 signals that are obtained at this time be referred to as $V_{1,P}$ and $V_{2,P}$ respectively. As the cell is polarized, $T_{3,0}$ changes to $T_{3,P}$ and N in general may take on a different value, which is referred to as $\widetilde{N}$. None of the properties of M1, M2, or of the polarizer are adjusted during data taking, so $V_{1,P}$ and $V_{2,P}$ are expressed as shown in equations (4.10) and (4.11).

$$V_{1,P} = \widetilde{N} f_1 R_1 \tag{4.10}$$

$$V_{2,P} = \widetilde{N} \alpha t T_{3,P} f_2 R_2 \tag{4.11}$$

To determine the ratio of transmissions of unpolarized to polarized ^{3}He in the cell, it is sufficient to calculate the ratio involving four pedestal-subtracted voltage signals that is given by:

$$\frac{V_{2,0}/V_{1,0}}{V_{2,P}/V_{1,P}} = \frac{N \alpha t T_{3,0} f_2 R_2 / N f_1 R_1}{\widetilde{N} \alpha t T_{3,P} f_2 R_2 / \widetilde{N} f_1 R_1} = \frac{T_{3,0}}{T_{3,P}}. \tag{4.12}$$

4.2.2 The ^{3}He polarization

After the beam polarization has been determined, it is possible to determine the ^{3}He polarization as well. At another time before data-taking has ended, the polarizer cell is removed from the apparatus, but everything else including the oven is left untouched. The pedestal-subtracted voltage signals at this time are given by V_1' and V_2'. From equation (3.16), the product $T_4 T_{3,0}$ can be found:

$$\frac{V_{2,0}/V_{1,0}}{V_{2,P}'/V_{1,P}'} = T_4 T_{3,0}. \tag{4.13}$$

With knowledge of the properties of the glass that the ^{3}He cell is composed of, and hence of T_4, it is thus possible using equations (4.5), (4.6) and (4.13) to determine the ^{3}He polarization.

4.3 An Example of a Polarization Measurement

4.3.1 Selecting the data

The purpose of this discussion is to illustrate the method of a polarization measurement. The data runs that will be discussed, and a short explanation of them, can be found in table 4.1. All of these data runs were taken at a time when the frame overlap chopper was in use.

between M1 and M2		run number
unpolarized cell	oven	2995
polarized cell	oven	2709
unpolarized cell	oven	5632
no cell	oven	5639
GE180 glass window		5517
no GE180 glass window		5519

Table 4.1: The data runs that were selected for a sample polarization measurement. Runs 2995 and 2709 are used to determine the beam polarization. Runs 5632 and 5639 are used to determine the transmission of the unpolarized cell (including the transmission of its glass walls). Runs 5517 and 5519 are used to determine the transmission of a 3.5 mm thick window of GE180 glass. These final two data runs can be used to provide knowledge of the transmission of the cell walls which are composed of GE180 glass. GE180 is a special type of glass that does not contain boron. Runs 2995 and 5639 are interchangeable. Run 2709 is one of many that could have been used, but was picked randomly as a representative of a typical set of data with polarized beam. All of the data runs shown above have a corresponding pedestal run that was taken within a few hours time from the data run itself.

4.3.2 A measurement of beam polarization

Figure 4.1 shows the signal from M2, normalized to the same proton current, under the conditions when: 1) the polarizer cell is polarized; and 2) the polarizer cell is unpolarized. The purpose of this figure is to provide an illustration of the polarization-dependent transmission of the ^{3}He cell.

The transmission of ^{3}He is dependent on its areal density and on its polarization (see section 4.1). The effect of the factor $exp(-n_3\sigma)$ from equation (4.4) cannot be seen in figure 4.1 since it is common to the two plots. However, the effect of the factor $cosh(n_3\sigma P_3)$ can be seen due to its dependence on P_3. At short times of flight, σ approaches zero, so the effect of this factor is small. However, as σ increases linearly with time of flight, the effect of this factor, and hence the polarization dependence of the transmission through the polarizer, becomes more important.

As was discussed in section 4.1, it is the ratio of the flux at M2 under these separate conditions that allows for a determination of the beam polarization P_n. In order to determine P_n, equations (4.7) and (4.12) were applied once per time bin to the pedestal-subtracted data.

The result is shown plotted in figure 4.2. A fit is also shown of the function from equation (4.5). Some general features are worth noting. First of all, the data tend to deviate above the curve for short times of flight and below the curve for long times of flight. This behaviour has not been explained, although it should not be due to the curvature of the cell or interference from scattering, as is explained in sections 4.4 and 4.5. Qualitatively, this behaviour is consistent with the observation that low energy neutrons from two pulses previous may be present in the beam. One would expect an admixture of low energy neutrons to diminish the ratio T_0/T_P (see figure 4.1), thus increasing the measured value of the polarization. This effect should be the largest at short times of flight since this is when the high energy neutrons leave only a small signal in the monitors, and since this is when the population of overlapping neutrons is the largest. However, this possibility was not investigated in any quantitative manner.

The fit shown in figure 4.2 was determined using the hyperbolic arctangent of the data

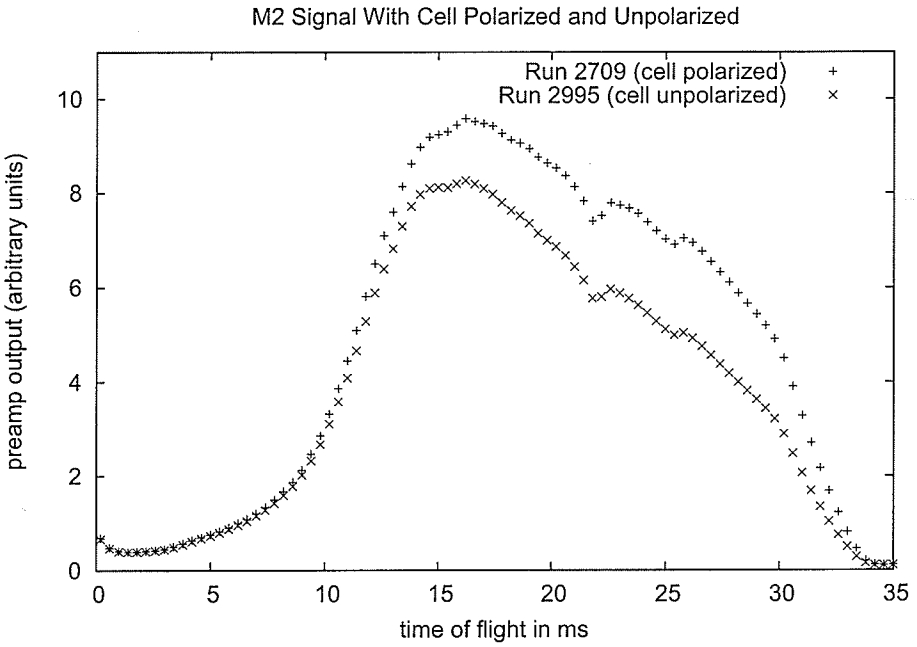

Figure 4.1: Plots showing the polarization-dependent signal in M2. These plots show the monitor signals averaged over 10,000 pulses, so the statistical error bars are too small to display. These two plots are normalized to the same proton current and so can be used to demonstrate the polarization-dependent transmission of the ^{3}He cell. It is the ratio between these two signals that allows for the beam polarization to be determined. Note that the normalization could also have been done using the M1 signal, as is done in the analysis that follows. Normalization to proton current or M1 is essentially equivalent for these two runs (see figure 3.13).

points shown and a least squares fit to a straight line. A straight line with zero intercept:

$$arctanh\left(\sqrt{1-\left(\frac{T_{3,0}}{T_{3,P}}\right)^2}\right) = n_3\sigma P_3 \tag{4.14}$$

is expected, where n_3 and P_3 are constants and σ is proportional to time of flight.

The method of the linear fit is explained in figure 4.3. The result is:

$$n\sigma P_3 = (0.033 \pm 0.001\ \mathrm{ms}^{-1})t. \tag{4.15}$$

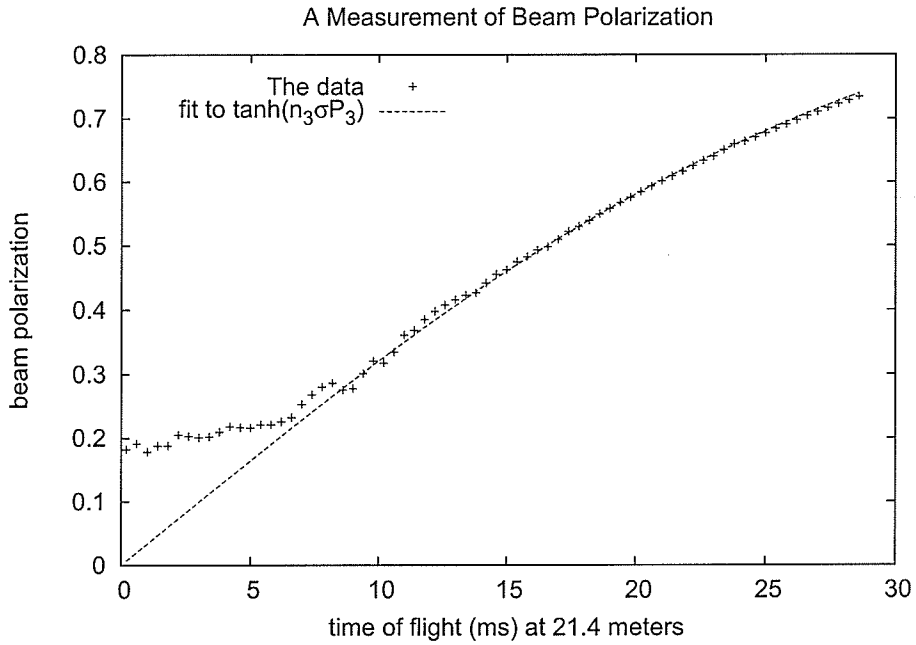

Figure 4.2: Beam polarization measured as a function of time of flight, using data that is shown in table 4.1. The statistical error bars are too small to be shown. The effects of scattering and cell curvature on this measurement were investigated, and were found to be negligible. The fit has a tendency to be below the data at short times of flight and above the data at long times of flight. These deviations, including the specific behaviour of the large deviations at short times of flight, are reproduced for other data runs, but have not been quantitatively explained. The times of flight relevant for a measurement of A_γ using liquid hydrogen are at greater than 12.5 ms which corresponds to 15 meV.

This provides an expression for the beam polarization:

$$P_n = tanh(at) \pm \left[1 - tanh^2(at)\right] t\delta a, \tag{4.16}$$

where t is time of flight, $a = 0.033$ ms^{-1} and $\delta a = 0.001$ ms^{-1}. The relative uncertainty in P_n is therefore approximately 2 % and roughly independent of time of flight. This uncertainty is sufficient for a measurement of A_γ at the proposed precision. If the nature of the deviation from the fit at short times of flight is understood, then this uncertainty may

decrease considerably.

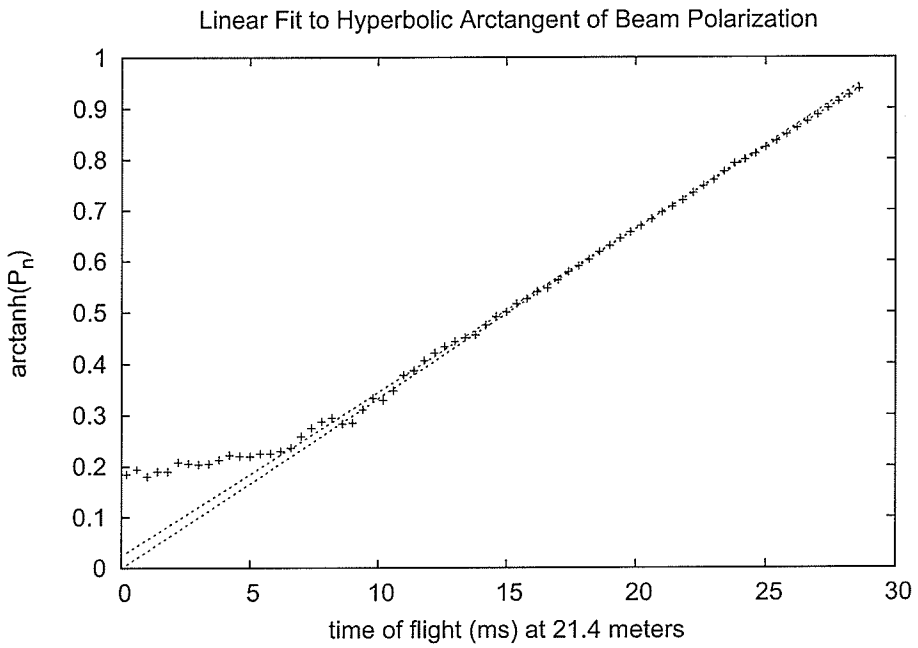

Figure 4.3: The hyperbolic arctangent of beam polarization is expected to be linearly proportional to time of flight (t) as shown in equation (4.14). Two linear fitting methods were performed of $arctanh(P_n)$ versus t in order to determine an uncertainty for P_n. The first method was a least squares fit between 24.2 ms and 28.6 ms that did not impose restrictions on the intercept and that yielded $arctanh(P_n) = 0.033+0.032t$. The second method was a least squares fit between 10.6 ms and 28.6 ms that was forced to pass through the origin. The second method yielded $arctanh(P_n) = 0.033t$. The graph above shows these two fits along with the data. As it is expected from equation (4.14), the intercept was assumed to be zero. The variation in the slope was then taken to give the uncertainty in the fit. The result is stated in equation (4.15).

4.3.3 A measurement of the ^{3}He polarization

As described in section 4.3.2, a value for $n\sigma P_3$ has now been determined. It is thus possible to determine P_3 by measuring n. This discussion involves the ^{3}He cell that was used during the commissioning run, and that is referred to as *BooBoo*.

In order to determine n, the transmission of the unpolarized cell was measured. The logarithm of the transmission of unpolarized ^{3}He versus time of flight is expected to be a straight line passing through the origin, with slope proportional to n. The proportionality constant is determined by the distance L from the moderator, and by equation (3.3).

However, the cell has walls that are composed of GE180 glass, and that therefore also attenuate the beam. GE180 is a special type of glass that does not contain boron. This type of glass is desirable since boron has a large cross-section for neutron absorption. The presence of boron would therefore give rise to unnecessary attenuation of the beam. In addition, since the boron cross section is also proportional to time of flight, the existence of an unknown quantity of boron would introduce uncertainties during the measurement of the cell's ^{3}He content.

In order to extract a ^{3}He content from the unpolarized cell transmission measurement, the transmission of the cell walls must be corrected for. In order to do so, the transmission of a window of GE180 glass [69] was measured using the standard beam monitor method of section 3.1.8. The result of this measurement is shown in figure 4.4. The transmission of the glass depends much less on time of flight than the ^{3}He does, and so a determination of the ^{3}He content is only slightly affected by uncertainties associated with the glass.

There is a unique linear combination of glass and ^{3}He transmissions that corresponds to a given transmission measurement. This can be stated as:

$$ln(T_3) = ln(T_0) - f ln(T_5), \tag{4.17}$$

where T_0 is the directly measured transmission of the whole cell, T_5 is the directly measured transmission of the sample glass window, f is a factor that depends on the amount of glass in the cell ($(T_5)^f = (T_4)^2$, see figure 4.6), and T_3 is the transmission of the ^{3}He alone.

Equation (4.17) can be taken advantage of in order to determine both the ^{3}He areal density and glass thickness. This was carried out by performing linear fits of $ln(T_3)$ versus $ln(T_0) - f ln(T_5)$ for variable values of f. For each value of f, four fits were performed over the following time of flight ranges: 8.2 ms to 28.2 ms, 8.2 ms to 18.2 ms, 18.2 ms to 28.2 ms, and 14.2 ms to 23.0 ms. The variation of the slope and intercept over these regions allowed for a determination of their uncertainties.

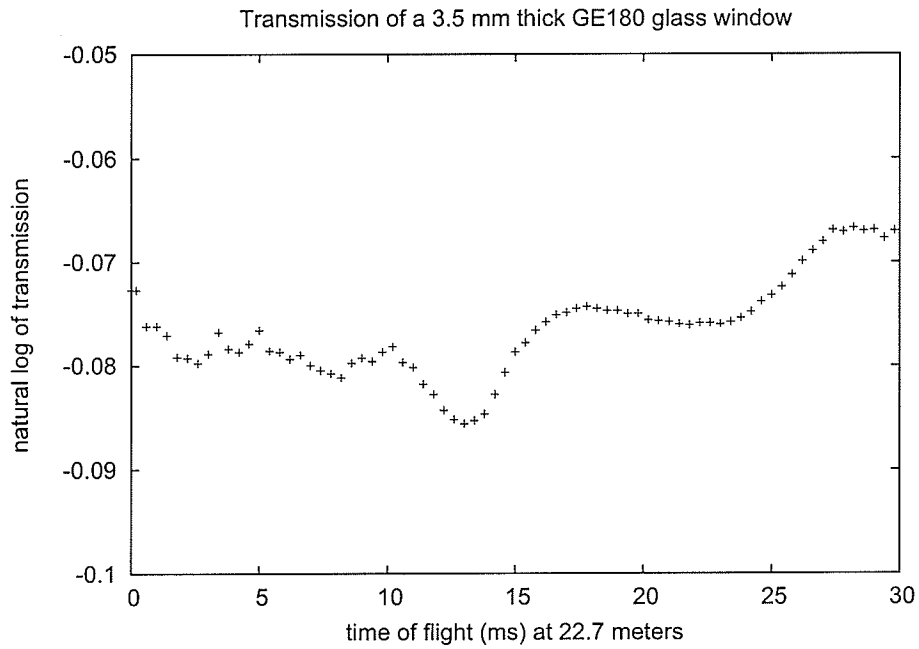

Figure 4.4: This transmission measurement of a 3.5 mm thick GE180 window was carried out using M3 normalized to M2 and so corresponds to a different distance from the source than the other measurements discussed in this chapter. This difference was corrected for by rescaling the time axis of the glass data. It's interesting to note that the transmission increases slightly at long times of flight, despite the expectation that small amounts of absorption would cause the cross section to increase slightly. This observation might be explained by the fact that glass is not entirely amorphous, and so the transmission may depend on effects from diffraction.

It was determined that the quality of the fit was not affected by the value of f. Instead, the thickness of the glass was determined by forcing the intercept to be zero. An average intercept of zero was found to occur for 6.0 mm glass thickness, and the largest deviation of the four fits from zero corresponded to 0.5 mm. Due to the fact that the composition of the glass is likely to vary from sample to sample, and since the cell and window were not necessarily made from the same batch of glass, the value for the glass thickness is stated as 6 ± 1mm. This value is consistent with the thickness of 3-4 mm per wall that was estimated by the builders of the cell [70].

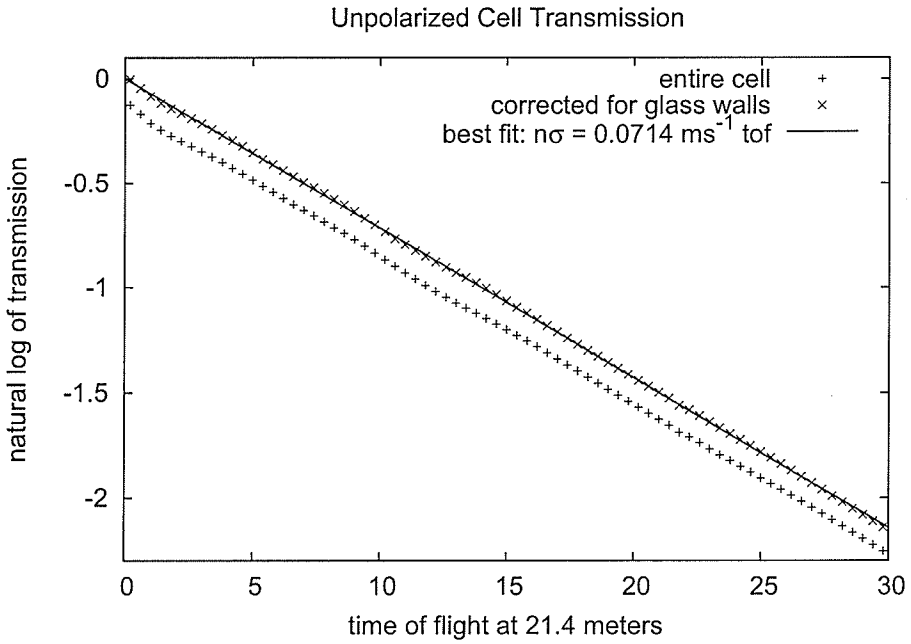

Figure 4.5: A measurement of the ^{3}He content of the polarizer cell BooBoo. The lower set of data points is the raw measurement of the transmission of the entire cell. The upper set shows the same set of data with a correction for the glass transmission. These data show a remarkably linear dependence on time of flight and are confirmation of the fact that σ varies inversely with neutron speed.

The slope for a glass thickness of 6.0 mm was determined to have an average value over the four fits of 0.0714 ms^{-1} and a variation of 0.0004 ms^{-1}. Another uncertainty that was taken into account was the lack of knowledge of the M1 pedestal (see p. 60). Using the offset from the chopper-closed signal as opposed to the shutter-closed signal gave rise to a difference in the slope of 0.2 %. Finally it was observed that changing the value of f not only changed the intercept but also the slope. Changing the glass thickness by 1 mm affected the slope by about 0.4 %. Combining these sources of uncertainty in quadrature and being generous for the sake of caution gives a slope of

$$n\sigma = 0.0714 \pm 0.0009 \text{ ms}^{-1}. \tag{4.18}$$

For a distance to the source of 21.4 meters, this corresponds to $n\sigma = 4.85$ amagat·cm (one amagat is the density of an ideal gas at STP).

It is now possible to determine the ^{3}He polarization. Combining the results from equations (4.15) and (4.18), the ^{3}He polarization was determined to be 0.46 ± 0.01. By using this method it is possible to know at any time during an asymmetry measurement whether the polarizer is functioning at the appropriate level.

This polarization is lower than was expected given bench tests that had been performed earlier. Later measurements have shown ^{3}He polarizations as high as 57 % [71, 72]. However, the ^{3}He polarization appears to be unstable and varies between 30 % and 57 %. Work is underway to improve the long-term stability of the ^{3}He polarization.

4.4 *Effects from scattering on beam monitor polarimetry measurements*

4.4.1 Introduction

This section addresses the problem of neutron scattering in and around the ^{3}He spin filter. As explained in previous sections of this chapter, neutron and ^{3}He polarization measurements are made using beam monitor ratios to determine the transmission of the polarizer cell. This measurement can only be exact if the transmission is determined of the ^{3}He inside the polarizer alone, or if the transmission from other materials cancels out of the ratio.

Ideally, the solid angles subtended by M1 and M2 about the sources of scattering would be sufficiently small for scattered neutrons to not contribute to monitor signals. In such a case, scattered neutrons could be treated in the same manner as absorbed neutrons. However, in the NPDGamma apparatus, the cell is bracketed between the two monitors, as shown in figure 4.6 which shows the setup that was used during data-taking in March of 2004. Since there are scattering materials located between the two monitors, it is not immediately obvious whether equation (4.7) can be used without applying a correction to the result.

In this section, the setup of the apparatus around the polarizer and M1 and M2 is analyzed, in order to arrive at an estimate of the amount of scattering. Applying the results from section 4.3, values for the beam polarization and cell thickness are assumed. With knowledge of this information, calculations are done in order to compare the true beam polarization to the beam polarization as it would be measured using the beam monitors. The conclusion arrived at from this analysis is that scattering affects both the neutron and ^{3}He polarization measurements by a negligible amount.

4.4.2 An estimate of the effect of neutron scattering on the polarimetry measurements

The materials (other than ^{3}He) that exist close to the beam monitors during a polarization measurement are: 1) Two 3-4 mm thick cell walls, made from GE180 glass; 2) Two 2 mm thick oven walls, made of pure silicon, and 3) 3.5 mm of aluminum inside the monitors

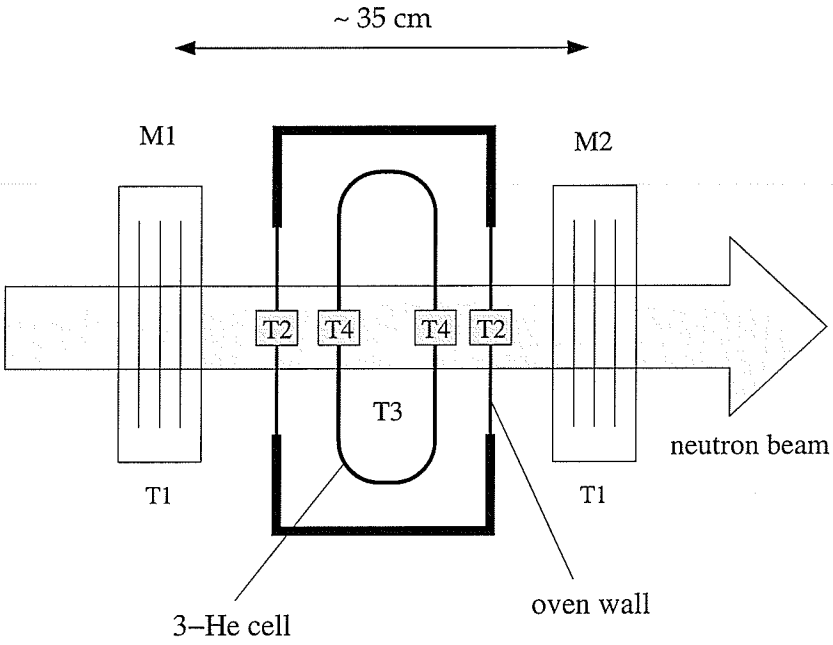

Figure 4.6: A diagram that includes consideration of scattering materials that are present during a polarization measurement. Monitors M1 and M2 are used to measure the transmission of the polarizer cell. T_1 is the transmission of M1. T_3 is the transmission of the ^{3}He inside the polarizer, T_2 is the transmission of the silicon walls of the polarizer oven, and T_4 is the transmission of the GE180 glass walls of the polarizer cell.

themselves. A fraction of the beam is lost in all of these materials, primarily as a result of scattering.

From observations of the ratio of M1 and M2 signals during run 5639 (see figure 3.19), and correcting for the transmission of M1, the transmission of one of the oven windows is approximately 0.94. Observations of transmission of a block of aluminum (see section 3.3.5) provide for the estimate for transmission of 3.5 mm of aluminum to be approximately 0.97. The transmission of the monitors is dependent on energy due to the ^{3}He that they contain, but for the purposes of this discussion, the total transmission of the monitors will

be taken to be 0.95, independent of energy. Here T_1 is used to denote the probability for transmission through the whole monitor and T_1' is used to denote the probability for not being scattered from the monitor. The transmission of a 3.5 mm thick window of GE180 glass was measured using the beam monitors and was found to vary (over the energies 4 meV to 50 meV) between 0.92 and 0.93 (see section 4.3.3). A summary of all of these results is provided in table 4.2.

	label	estimated value
entire beam monitor	T_1	0.95
3.5 mm Al	T_1'	0.97
2 mm Si	T_2	0.94
4 mm GE180 glass	T_4	0.91

Table 4.2: Estimates of the transmission of materials other than ^{3}He that are present in the beam during a polarization measurement (see figure 4.6). The attenuations from aluminum, silicon and glass are due to a large extent to scattering.

4.4.3 An estimation of the solid angles

Having determined the extent of the scattering, it is now necessary to determine the solid angle subtended by the monitors about the scattering materials. The solid angles that are considered are shown in figure 4.7.

In order to calculate the effective solid angle for a given window, it would be possible to integrate the contributions from infinitesimal elements across the whole window. However, the element at the center of a scattering object will contribute the largest amount to the effective solid angle. If the whole window is treated as if it corresponded to the same solid angle as the center, the result will be an overestimate of the contribution from scattering. If the result determined from this method is negligible, then the real effect will also be negligible. The distances relevant to this calculation are shown in table 4.3.

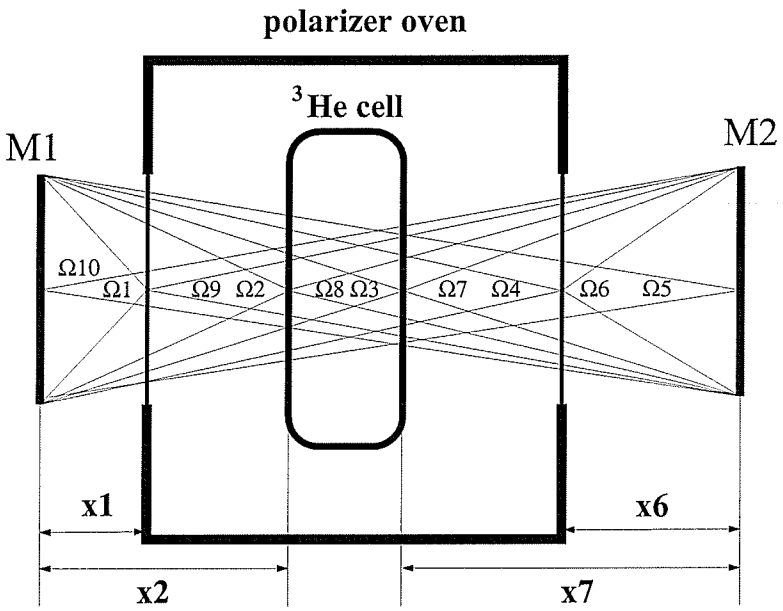

Figure 4.7: Each solid angle to be considered is shown labeled in this diagram. x_i are the distances that correspond to the solid angles Ω_i.

Each solid angle can then be determined using the following expression:

$$\frac{\Omega_i}{4\pi} = \frac{1}{2}\left(1 - \frac{x_i}{\sqrt{x_i^2 + (a/2)^2}}\right), \tag{4.19}$$

where a is approximately 12 cm, the width of a beam monitor. Using this method, the following values were found:

$$\frac{\Omega_1}{4\pi} = 0.20, \quad \frac{\Omega_2}{4\pi} = 0.051, \quad \frac{\Omega_3}{4\pi} = 0.029, \quad \frac{\Omega_4}{4\pi} = 0.014, \quad \frac{\Omega_5}{4\pi} = 0.0089.$$

It will later be demonstrated that Ω_6 to Ω_{10} will cancel out of the final answer and can therefore be ignored.

from	to	distance (cm)
M1	first silicon window	5.0
M1	first GE180 window	13.8
M1	second GE180 window	19
M1	second silicon window	28
M2	first silicon window	31
M2	first GE180 window	22.4
M2	second GE180 window	17
M2	second silicon window	8.3
M1	M2	35.5

Table 4.3: The distances between objects that are considered in this discussion of the effect of scattering on a polarization measurement. (see figure 4.6).

4.4.4 Determination of the size of the effect from scattering

In order to estimate the extent of the scattering effect, only first-order corrections will be considered. Here a first-order scattering correction is one that treats the second scatter of any neutron to be equivalent to an absorption. Also, any scatter will be considered to be isotropic in the lab. This latter simplification is justified by the low energies that are involved. Due to the low energies, a partial wave expansion of the neutron-scattering center system will be primarily s wave and therefore spherically symmetric.

The observed signal (S_1) from M1 is given by the number of neutrons in the beam before hitting M1, plus first-order corrections due to backscatter and subsequent losses on the way back to M1. Referring to figures 4.6 and 4.7, the expression for S_1 can be represented as:

$$\begin{aligned} S_1 &= K_1 N \\ &\quad + K_1 N T_1 (1 - T_2) \frac{\Omega_1}{4\pi} \\ &\quad + K_1 N T_1 T_2 (1 - T_4) \frac{\Omega_2}{4\pi} T_2 \end{aligned}$$

$$
\begin{aligned}
&+ K_1 N T_1 T_2 T_4 T_3 (1 - T_4) \frac{\Omega_3}{4\pi} T_3 T_4 T_2 \\
&+ K_1 N T_1 T_2 T_4 T_3 T_4 (1 - T_2) \frac{\Omega_4}{4\pi} T_4 T_3 T_4 T_2 \\
&+ K_1 N T_1 T_2 T_4 T_3 T_4 T_2 (1 - T_1') \frac{\Omega_5}{4\pi} T_2 T_4 T_3 T_4 T_2 \\
&= K_1 N (A + B T_3^2)
\end{aligned} \tag{4.20}
$$

where A = 1.015, B = 0.0024, N is the number of neutrons incident on the face of M1, and K_1 is the time of flight-dependent proportionality between beam flux and preamplifier voltage.

Similarly, the signal (S_2) in M2 is the number of neutrons that are transmitted to M2, plus first order corrections due to forward scatter and subsequent losses on the way forwards to M2:

$$
\begin{aligned}
S_2 = &K_2 N T_1 T_2 T_4 T_3 T_4 T_2 \\
&+ K_2 N T_1 T_2 T_4 T_3 T_4 (1 - T_2) \frac{\Omega_6}{4\pi} \\
&+ K_2 N T_1 T_2 T_4 T_3 (1 - T_4) T_2 \frac{\Omega_7}{4\pi} \\
&+ K_2 N T_1 T_2 (1 - T_4) T_3 T_4 T_2 \frac{\Omega_8}{4\pi} \\
&+ K_2 N T_1 (1 - T_2) T_4 T_3 T_4 T_2 \frac{\Omega_9}{4\pi} \\
&+ K_2 N (1 - T_1') T_2 T_4 T_3 T_4 T_2 \frac{\Omega_{10}}{4\pi} \\
&= K_2 N x T_3,
\end{aligned} \tag{4.21}
$$

where the functional form of x is irrelevant since it will cancel out before the final result is reached.

The ratio between S_2 and S_1 for a given data-taking run is then given by:

$$
R = \frac{S_2}{S_1} = \frac{K_2 N x T_3}{K_1 N (A + B\,(T_3)^2)}. \tag{4.22}
$$

The ratio of ratios $S2/S1$ (unpolarized) to $S2/S1$ (polarized) is therefore given by:

$$
\frac{R_0}{R_P} = \frac{K_2 N x T_{3,0} / K1 N (A + B\,(T_{3,0})^2)}{K_2 N' x T_{3,P} / K1 N' (A + B\,(T_{3,P})^2)} = \left[\frac{T_{3,0}}{T_{3,P}}\right] \left\{\frac{A + B\,(T_{3,P})^2}{A + B\,(T_{3,0})^2}\right\} \tag{4.23}
$$

where N is the number of neutrons incident on M1 at the time that the beam is unpolarized and N' is the number of neutrons incident on M1 at the time that the beam is polarized.

The factor that is in the square brackets is the required result, while the quantity on the left-hand side is what is measured. Since $T_{3,P} > T_{3,0}$, and since A and B are positive quantities, the correction factor will in all cases be greater than unity. If the correction is not taken into account, measured polarization will therefore be less than actual polarization:

$$\frac{R_0}{R_P} > \frac{T_{3,0}}{T_{3,P}} > 0 \implies \sqrt{1-\left(\frac{R_0}{R_P}\right)^2} < \sqrt{1-\left(\frac{T_{3,0}}{T_{3,P}}\right)^2}. \tag{4.24}$$

4.4.5 Application to the conditions at Flight Path 12

The goal of this analysis is to find out to what extent the correction factor that occurs in curly braces in equation (4.23) differs from unity. To achieve this goal, the measurements that were discussed in section 4.3 were used. Thus $P_3 = 0.46$ and $n\sigma = (0.0714\ \mathrm{ms}^{-1})\mathrm{t}$ as seen by M2, where t is time of flight. These measured values of the ^{3}He polarization and ^{3}He thickness were assumed to be representative of the true values that exist. Using this assumption, true beam polarization, measured ^{3}He polarization, and measured beam polarization were calculated as a function of time of flight. These calculations were carried out using the following set of expressions:

$$\begin{aligned}
\text{the transmission of the unpolarized } ^3\text{He}: &\quad T_{3,0} = e^{-n\sigma} \\
\text{the transmission of the polarized } ^3\text{He}: &\quad T_{3,P} = T_{3,0}\ cosh(n\sigma P_3) \\
\text{the beam polarization}: &\quad P_n = \sqrt{1-\left(\frac{T_{3,0}}{T_{3,P}}\right)^2} \\
\text{the measured transmission ratio}: &\quad \frac{R_0}{R_P} = \left[\frac{T_{3,0}}{T_{3,P}}\right]\left\{\frac{A+B\,(T_{3,P})^2}{A+B\,(T_{3,0})^2}\right\} \\
\text{the measured beam polarization}: &\quad P_n' = \sqrt{1-\left(\frac{R_0}{R_P}\right)^2} \\
\text{the measured } ^3\text{He polarization}: &\quad P_3' = arctanh(P_n')/n\sigma.
\end{aligned}$$

The results of these calculations are shown in table 4.4.

4.4.6 Conclusion

The ratios P_n'/P_n and P_3'/P_3 are all within 0.1% of unity. This represents a small deviation compared to the uncertainty in an actual polarization measurement. Considera-

tof (ms)	P_n	P_n'	P_n'/P_n	P_3'	P_3'/P_3
6	19.4552	19.4354	0.9990	45.9520	0.9990
10	31.7118	31.6936	0.9994	45.9716	0.9994
14	42.9934	42.9795	0.9997	45.9829	0.9996
18	53.0752	53.0655	0.9998	45.9895	0.9998
22	61.8497	61.8433	0.9999	45.9934	0.9999
26	69.3124	69.3084	0.9999	45.9958	0.9999
30	75.5360	75.5335	1.0000	45.9973	0.9999
34	80.6417	80.6402	1.0000	45.9982	1.0000
38	84.7742	84.7733	1.0000	45.9988	1.0000

Table 4.4: Estimations of corrections to polarimetry measurements from scattering. These calculations correspond to a ^{3}He polarization of P_3 =0.46 and a cell thickness of $n\sigma = (0.0714\ \mathrm{ms}^{-1})\,t$ where t is time of flight. P_n is the true beam polarization. P_3' and P_n' are respectively the ^{3}He and beam polarizations that would be measured given the assumptions regarding scattering.

tions from scattering therefore have a negligible effect on beam monitor polarimetry for the NPDGamma experiment.

4.5 Effects of Polarizer Cell Curvature on Beam Monitor Polarimetry

4.5.1 Introduction

This section addresses the effect of polarizer cell curvature on beam monitor polarimetry for the NPDGamma experiment. Measurements of neutron and ^{3}He polarization have so far been carried out by employing beam monitor ratios that use the full width of the beam. This method may introduce errors if the cell is of nonuniform thickness over the width of the beam. Since the polarizer cell was of nonuniform thickness, it is important to consider the effect of the curvature of the cell on the polarization measurements.

The problem is addressed by assuming the ^{3}He polarization that was measured in section 4.3, and by assuming a simple model for the ^{3}He areal density distribution. Mathematical expressions are derived for the true beam polarization, the measured beam polarization, and the measured ^{3}He polarization. As will be explained, a numerical approach is used to determine to what extent the true polarizations differ from the polarizations that were determined from the beam monitor ratios. The effect was found to be negligible.

4.5.2 An expression for beam polarization that takes into account cell curvature

Here an expression is derived for the polarization of the full beam after leaving a polarizer cell of general shape. The beam is assumed to be unpolarized and of uniform density before entering the polarizer.

Consider a polarizer cell that has nonuniform thickness. The areal density, t, of the ^{3}He inside the cell can be expressed as a function of the position in the x-y plane, where z is the beam direction. The total number of neutrons incident on the cell is given by N_0 and the total number of neutrons leaving the cell is given by N. This situation is illustrated in figure 4.8.

In order to determine the polarization of the full beam after leaving the cell, first consider some region of the beam that is sufficiently small for the beam transmission to be assumed uniform over that region. Allow there to be many such regions (n in total), each subscripted by the index i, that together cover the whole width of the beam. The i^{th} region is centered

at the point $(x, y)_i$. The area occupied by the whole beam is given by A while the area occupied by the i^{th} region is given by δA_i.

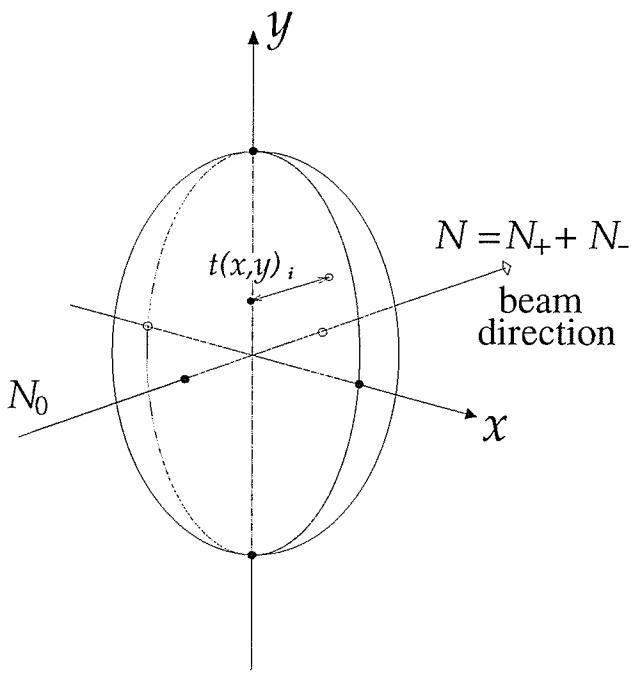

Figure 4.8: The thickness of the NPDGamma polarizer cell is nonuniform.

On leaving the polarizer cell, the number of neutrons at point $(x, y)_i$ that have spin oriented in the up direction is then given by

$$\delta N_+^i = \frac{\delta A_i}{A} N_0 \, exp(-t(x,y)_i \, [1 - P_3] \, \sigma) \tag{4.25}$$

and the number of neutrons with spin oriented in the down direction is given by

$$\delta N_-^i = \frac{\delta A_i}{A} N_0 \, exp(-t(x,y)_i \, [1 + P_3] \, \sigma). \tag{4.26}$$

If $N_+ = \sum_i^n \delta N_+^i$ is the total number of neutrons oriented in the up direction and $N_- = \sum_i^n \delta N_-^i$ is the total number of neutrons oriented in the down direction over the whole beam downstream of the polarizer cell, then the polarization P_n of the beam after leaving the cell is given by:

$$P_n = \frac{N_+ - N_-}{N_+ + N_-} = \frac{\sum_i \delta A_i exp(-\sigma t(x,y)_i) sinh(\sigma t(x,y)_i P_3)}{\sum_i \delta A_i exp(-\sigma t(x,y)_i) cosh(\sigma t(x,y)_i P_3)}. \quad (4.27)$$

4.5.3 An expression for the neutron polarization as measured from the beam monitor ratios

An expression will now be derived for the neutron polarization that is measured using the beam monitor ratios. This quantity will be referred to as P_n' in order to distinguish it from the true beam polarization P_n.

As discussed in sections 4.1 to 4.3, the following expression is used to determine the neutron polarization:

$$P_n' = \sqrt{1 - \left(\frac{T_{3,0}}{T_{3,P}}\right)^2}, \quad (4.28)$$

where $T_{3,0}$ is the transmission of the full beam through the ^{3}He when it is unpolarized and $T_{3,P}$ is the transmission of the full beam through the ^{3}He at the time that the polarization measurement is being made.

The number of neutrons that transmit through an area element δA_i of the cell is

$$\delta N_i = \frac{N_0}{A} \delta A_i \; exp(-\sigma t(x,y)_i) \quad (4.29)$$

if the cell is unpolarized or

$$\delta N_i = \frac{N_0}{A} \delta A_i \; exp(-\sigma t(x,y)_i) cosh(\sigma t(x,y)_i P_3) \quad (4.30)$$

if the cell is polarized.

The transmission of the full beam, whether polarized or unpolarized, is given by $T = N/N_0$ where $N = \sum \delta N_i$. This yields

$$T_0 = \frac{1}{A} \sum_i^n exp(-\sigma t(x,y)) \delta A_i \quad (4.31)$$

and

$$T = \frac{1}{A} \sum_i^n exp(-\sigma t(x,y)) cosh(\sigma t(x,y) P_3) \delta A_i. \quad (4.32)$$

Therefore, according to equation (4.28), the measured beam polarization will be:

$$P_n' = \sqrt{1 - \left(\frac{\sum exp(-\sigma t(x,y)) \delta A_i}{\sum exp(-\sigma t(x,y)) cosh(\sigma t(x,y) P_3) \delta A_i}\right)^2}. \quad (4.33)$$

4.5.4 An expression for the ^{3}He polarization as measured from the beam monitor ratios

The measured ^{3}He polarization, P_3', is determined in terms of other measured or known quantities by use of the expression:

$$P_n' = tanh(\sigma t' P_3'). \tag{4.34}$$

The well-known n-^{3}He cross section is denoted by σ as usual, and t' is the areal density of ^{3}He over the whole cell, as determined from a full beam transmission measurement:

$$T_0 = exp(-\sigma t'). \tag{4.35}$$

P_3' can thus be calculated in terms of other known or calculable quantities.

4.5.5 The calculations

In order to evaluate the difference between P and P', some assumptions about the properties of the cell need to be made. First a model of the cell dimensions will be assumed. At NIST, the thickness at the center of the cell was determined to be 5.5 atm·cm [73], and at LANSCE t' was determined from beam monitor measurements to be 4.85 atm·cm. A simple model is to assume that the two walls of the cell are conical in shape and rotationally symmetric about the beam axis. The cell would then have a peak thickness in the center of 5.5 Atm·cm and the slope of the walls would be determined in order to give $t' = 4.85$ Atm·cm. This corresponds to the following expression for t:

$$t = 5.5 \text{ Atm} \cdot \text{cm} - (0.172 \text{ Atm})r \tag{4.36}$$

where r is the perpendicular distance from the cell axis.

The rest of the required assumptions are: L, the distance from the source to M2, is 21.40 meters (measurements of cell transmission are made using M2); $P_3 = 0.46$; the neutron beam is 9.5 cm × 9.5 cm square and of constant areal density. With these assumptions in mind, t', P_n, P_n' and P_3' were numerically determined for various times of flight. The results are summarized in table 4.5.

4.5.6 Conclusion

According to this analysis, the ratio between true beam polarization and measured beam polarization differs from unity by 0.1 % or less. Similar corrections to the ^{3}He polarization are 0.2 % or less. These corrections are small enough to have a negligible effect on polarimetry measurements for the NPDGamma experiment. It is therefore acceptable to use monitor transmission ratios in the calculation of ^{3}He and neutron polarizations.

tof (ms)	t′ (Atm·cm)	P_n	P'_n	P'/P	P'_3	P'_3 / P_3
2.0	4.8570	0.0660	0.0659	1.0011	0.4605	1.0010
6.0	4.8554	0.1952	0.1950	1.0011	0.4603	1.0007
10.0	4.8538	0.3179	0.3175	1.0011	0.4602	1.0004
14.0	4.8522	0.4306	0.4301	1.0011	0.4600	1.0001
18.0	4.8506	0.5312	0.5306	1.0010	0.4599	0.9998
22.0	4.8490	0.6187	0.6181	1.0010	0.4598	0.9995
26.0	4.8475	0.6930	0.6924	1.0009	0.4597	0.9993
30.0	4.8459	0.7550	0.7544	1.0008	0.4596	0.9990
34.0	4.8443	0.8059	0.8053	1.0007	0.4595	0.9988
38.0	4.8428	0.8470	0.8465	1.0007	0.4594	0.9986

Table 4.5: Estimations of corrections to polarimetry measurements from polarizer curvature.

Chapter 5

SUMMARY AND CONCLUSION

This thesis has discussed several aspects of the NPDGamma experiment. The motivation behind NPDGamma was discussed, followed by an explanation of the experimental setup. The principal focus of this thesis was a detailed analysis of the neutron beam monitors which were custom built for the experiment.

The goal of the NPDGamma experiment is to observe the spatial distribution of gamma rays that are emitted during the fusion of a proton and a neutron. To within eight orders of magnitude, the spatial distribution is expected to be isotropic. At higher levels of precision, a correlation is expected to occur between the direction of gamma emission and the direction of neutron spin. It is this correlation that the NPDGamma collaboration proposes to measure.

In order to conduct this measurement, a high flux polarized cold neutron beam is required. Given the high beam flux, detection is run in current mode. The fact that the beam is pulsed allows for time of flight studies which are useful in performing diagnostic measurements throughout the experiment. To minimize the depolarization of the beam inside the liquid hydrogen target, the ortho- to para-hydrogen ratio of the liquid hydrogen must be minimized and monitored. Also, in order to extract a meaningful result from the measured asymmetry, the beam polarization must be known.

The NPDGamma beam monitors are ionization chambers that contain ^{3}He. They function by application of a high voltage and produce an electrical current that is directly proportional to the flux of the incident neutron beam. As such, they are particularly useful as a continuous monitor of beam flux, of beam polarization, and of the ortho- to para-hydrogen ratio of the liquid hydrogen target.

In this thesis, some properties of the beam monitors were studied. These studies were

started with a discussion of the $n + {}^3\mathrm{He}$ interaction, and with a Monte Carlo calculation that was used to determine the average amount of energy deposited into the monitors per captured neutron. It was determined that the energy deposited per neutron has an average value of 470 ± 20 keV and a standard deviation of 200 keV.

Each monitor has a specified total ^{3}He content that is dependent on its purpose. The ^{3}He contents of each monitor were measured using two separate methods that are discussed in section 3.3. The results from the two methods were found to be mostly in agreement, but were not in complete agreement with the specifications. These results are restated in table 5.1. It was concluded that the method of filling the monitors was approximate, at least partially due to the fact that they were not filled at constant temperature. A difficulty of attaining small pressures to high accuracy is also hypothesized.

	^{3}He content		
monitor	relative signal	aluminum corrected	specified
54	1.01 ± 0.07	1.03 ± 0.02	0.73
55	0.99 ± 0.07	1.21 ± 0.06	0.73
53	12.98 ± 0.09	13.07 ± 0.02	12.53
prototype	12.23 ± 0.09	12.41 ± 0.06	12.53
TRIPLE	not applicable	24.7 ± 0.2	25.1

Table 5.1: A summary of the beam monitor thickness measurements, in units of (10^{22} atoms ^{3}He)m^{-2} per 9.9 mm gas gap (there are in total four such gas gaps). The first data column shows the measurements that were made using a combination of transmission and relative signal measurements. The second data column shows the results of a separate method that corrected the transmission of the monitors with the transmission of a separate block of aluminum. Except for the entry corresponding to the TRIPLE monitor, the uncertainties in the second data column are entirely statistical. The third data column, corresponding to the pressures in table 3.1 at 20 °C, shows the specified contents.

It was demonstrated that the beam monitors work at a level of precision that is on the order of neutron counting statistics. Given the high beam flux, this precision is sufficient for all beam monitor analysis that is relevant to NPDGamma. It was also determined that the beam monitors provide a time of flight-dependent signal that is in agreement with the energy spectrum of the neutron beam. A discrepancy remains, however, in the absolute conversion of beam flux to current signal. This discrepancy does not affect the performance of the beam monitors and is not relevant to NPDGamma data analysis, but should be resolved by further measurements. An independent calibration of the beam monitors at a calibrated neutron source would provide a test of the calibration that was discussed in this thesis.

In chapter 4, the application of the beam monitors to beam polarimetry was demonstrated. The qualitative observations from polarization measurements were consistent with what is expected from theory. The quantitative results were somewhat low compared to what was expected, but it was later observed that the ^{3}He polarization has an unexplained tendency to drift over a fairly wide range. The relative uncertainty in both the ^{3}He and beam polarization was found to be at the level of 2 %, where the uncertainty in the beam polarization is roughly independent of energy. This level of precision is sufficient for a measurement of A_γ and will decrease significantly when the deviation of the data from the theoretical fit is understood.

If similar beam monitors are ordered in the future, some considerations should be kept in mind. First of all, HN connectors are not intended for use with voltages of several kilovolts, and give rise to sparking if extra care is not taken. For high voltages, SHV connectors would likely be ideal. If precise knowledge of the ^{3}He contents is desired, it would be worthwhile to avoid miscommunication by explicitly stating the required contents in units of volume density. If precise knowledge of the ^{3}He content is to be determined from experiment, it would be worthwhile to ensure that at least one extra monitor is made, of identical construction, containing N_2 and ^{4}He but no ^{3}He. However, knowledge of the ^{3}He content is not required in order to provide adequate performance for the NPDGamma experiment.

The beam monitors have been demonstrated to be very reliable monitors of beam

flux. They consistently provide a reliable signal. They were the first component of the NPDGamma apparatus to take data when the Flight Path 12 beam shutter was first opened in February of 2004, and have been in continuous use during NPDGamma data-taking ever since. They do not break down and, during the 2004 commissioning run, only failed to produce a signal when a preamplifier was blown by a faulty high voltage supply. They are not susceptible to gamma background and do not introduce noise or background to the surrounding apparatus. Once the liquid hydrogen target is installed, they should prove to be a reliable means of monitoring its ortho- to para-hydrogen ratio.

BIBLIOGRAPHY

[1] Ch. Elster R. Machleidt, K Holinde. *Physics Reports*, 149:1–89, 1987.

[2] S. Kistryn. *Phys. Rev. Lett.*, 58:1616, 1987.

[3] Jean-Louis Basdevant. *Mécanique Quantique.* École Polytechnique, 1986.

[4] Claude Cohen-Tannoudji, Bernard Diu, and Franck Laloë. *Quantum Mechanics.* John Wiley & Sons, 1977.

[5] J. J. Sakurai. *Modern Quantum Mechanics.* Addison-Wesley, revised edition, 1994.

[6] E. Merzbacher. *Quantum Mechanics.* John Wiley & Sons, Inc., third edition, 1998.

[7] T. D. Lee and C. N. Yang. *Phys. Rev.*, 104:254, 1956.

[8] C. S. Wu et al. *Phys. Rev.*, 105:1413, 1957.

[9] Donald H. Perkins. *Introduction to High Energy Physics.* Addison Wesley, third edition, 1987.

[10] N. Tanner. *Phys. Rev.*, 107:1203, 1957.

[11] R. Haas, L. B. Leipuner, and R. K. Adair. *Phys. Rev.*, 116:1221, 1959.

[12] Yu Abov. et al. *Phys. Lett.*, 12:25, 1964.

[13] Lobashov et al. *Phys. Lett.*, 25B, number 2:104, 1967.

[14] R. J. Blin-Stoyle. *Phys. Rev.*, 118:1605–1607, 1960.

[15] E. G. Adelberger and W. C. Haxton. *Ann. Rev. Nucl. Part. Sci.*, 35:501, 1985.

[16] W. Haeberli and B. R. Holstein. Parity violation and the nucleon-nucleon system. In W. C. Haxton and E. M. Henley, editors, *Symmetries and Fundamental Interactions in Nuclei*, pages 17–66. World Scientific, 1995.

[17] M. J. Ramsey-Musolf and S. A. Page. preprint: hep-ph/0601127, to appear in *Ann. Rev. of Nucl. Part. Sci.* Vol 56, January 2006.

[18] B. R. Holstein B. Desplanques, J. F. Donoghue. *Ann. Phys.*, 124:449, 1980.

[19] B. R. Holstein. *Phys. Rev. D*, 23:1618, 1981.

[20] B. Desplanques. In N. Auerbach and J. D. Bowman, editors, *Parity-Non-Conserving Nucleon-Nucleon Interactions.* World Scientific, Singapore, 1996.

[21] S. K. Krane. *Introductory Nuclear Physics.* John Wiley & Sons, 1988.

[22] G. Barton. *Nuovo Cimento*, 19:512, 1961.

[23] B. Desplanques and J. Missimer. *Nucl. Phys.*, A 300:286, 1978.

[24] R. Schiavilla, J. Carlson, and M. W. Paris. *Phys. Rev.*, C70:044007, 2004.

[25] A. R. Berdoz et al. *Phys. Rev. Lett.*, 87:272301, 2001.

[26] S. A. Page et al. *Phys. Rev. C*, 35:1119, 1987.

[27] C. D. Bass et al. *J. Res. Natl. Inst. Stand. Technol.*, 110:205–208, 2005.

[28] W. C. Haxton. *Phys. Rev. Lett.*, 46:C98, 1981.

[29] M. Bini et al. *Phys. Rev. Lett.*, 55(8):795, 1985.

[30] C. S. Wood et al. *Science*, 275:1759, 1997.

[31] W.C. Haxton. *Science*, 275:1753, 1997.

[32] W. S. Wilburn and J. D. Bowman. *Phys. Rev.*, C57:3425–3429, 1998.

[33] W. C. Haxton, C. P. Liu, and M. J. Ramsey-Musolf. *Phys. Rev. Lett.*, 86:5247–5250, 2001.

[34] Willem T. H. van Oers. *Nucl. Phys.*, A684:266c–276c, 2001.

[35] J. Byrne. *Neutrons, Nuclei and Matter: An Exploration of the Physics of Slow Neutrons.* Institute of Physics Publishing, 1994.

[36] N. A. Jelley. *Fundamentals of Nuclear Physics.* Cambridge University Press, 1990.

[37] M. T. Gericke. *The NPDGamma Experiment: The Weak Interaction Between Nucleons and Parity Violation in Cold Neutron Capture.* PhD thesis, Indiana University, 2004.

[38] R. Schiavilla, J. Carlson, and M. W. Paris. *Phys. Rev.*, C67:032501, 2003.

[39] J. F. Cavaignac, B. Vignon, and R. Wilson. *Phys. Lett.*, B67:148–150, 1977.

[40] G. S. Mitchell et al. *Nucl. Instr. and Meth.*, A521:468–479, 2004.

[41] G. S. Mitchell. Private communication.

[42] P.-N. Seo et al. *Nucl. Instr. and Meth.*, A 517:285, 2004.

[43] B. Lauss. First measurement of the guide coil field and the magnetic environment in the new npdγ cave at LANSCE. NPDGamma technical note 20 http://p23.lanl.gov/len/npdg/technotes/technotes.html, 2004.

[44] M. T. Gericke et al. *Nucl. Instr. and Meth.*, A540:328–347, 2005.

[45] W. S. Wilburn et al. *Nucl. Instr. and Meth.*, A 540:180, 2005.

[46] J. D. Bowman et al. Measurement of the parity-violating gamma asymmetry A_γ in the capture of polarized cold neutrons by para-hydrogen, $\vec{n} + p \rightarrow d + \gamma$. LA-UR-98-4413, Los Alamos National Laboratory.

[47] The NPDGamma Collaboration. A measurement of parity-violating gamma-ray asymmetry in polarized neutron capture on the deuteron: Letter of intent for the Fundamental Nuclear Physics Beamline at the SNS. Submitted to Oak Ridge National Laboratory, Aug 18, 2005.

[48] W. S. Wilburn et al. *J. Res. Natl. Inst. Stand. Technol.*, 2005.

[49] H. R. Weller; G. M. Hale D. R. Tilley. *Nucl. Phys*, A541:1, 1992.

[50] Evaluated Nuclear Structure Data Files. http://www.nndc.bnl.gov/ensdf/, January 26 2006.

[51] C. D. Keith et al. *Phys. Rev. C*, 69:034005, 2004.

[52] V. P. Alfimenkov et al. *Sov. J. Nucl. Phys.*, 25:607, 1977.

[53] P. R. Huffman et al. *Phys. Rev. C*, 70:014004, 2004.

[54] F. L. H. Wolfs et al. *Phys. Rev. Lett.*, 63:2721, 1989.

[55] LND inc. Radiation Detectors, 3230 Lawson Blvd., Oceanside, New York 11572, U.S.A.

[56] S. A. Page. Performance of the NPDGamma beam monitors in the fall, 2001 test run. unpublished, May 20, 2001.

[57] J. J. Szymanski et al. *Nucl. Instr. and Meth.*, 340:564–571, 1994.

[58] A. K. Vijh. *IEEE Trans. Electr. Insul.*, IE-12 No 4:313–315, 1977.

[59] Emilio Segrè. *Nuclei and Particles.* Benjamin/Cummings, 1977.

[60] Adrian C. Melissinos. *Experiments in Modern Physics.* Academic Press, 1966.

[61] J. F. Ziegler. SRIM & TRIM: Particle interactions with matter. http://www.srim.org.

[62] J. P. Biersack J. F. Ziegler and U. Littmark. *The Stopping and Range of Ions in Solids.* Pergamon Press, 1985, new edition in 2003.

[63] J. F. Ziegler. Plots of SRIM-2003 calculations and experimental results. http://www.srim.org/SRIM/SRIMPICS/STOPPLOTS.htm.

[64] W. R. Leo. *Techniques for Nuclear and Particle Physics: A How-to Approach.* Springer-Verlag, second revised edition, 1994.

[65] Philip R. Bevington and D. Keith Robinson. *Data Reduction and Error Analysis for the Physical Sciences.* McGraw-Hill Inc., second edition, 1992.

[66] D. J. Thomas and M. Burke. *Phys. Med. Biol.*, 30 No. 11:1201–1213, 1985.

[67] S. A. Page. Private communication.

[68] D. R. Rich et al. *Nucl. Instr. and Meth.*, A481:431–453, 2002.

[69] Glass sample courtesy of T. Gentile, NIST.

[70] T. Gentile. Private communication.

[71] M. Sharma. Neutron polarization analysis for $n + p \rightarrow d + \gamma$. unpublished technical note, Oct 29 2005, http://www.physics.lsa.umich.edu/chupp/npdg3He.

[72] T. Chupp et al. A large area polarized ^{3}He neutron spin filter. to be published.

[73] T. Gentile. Private communication.

[74] Glenn F. Knoll. *Radiation Detection and Measurement.* John Wiley & Sons, 1989.

[75] W. S. C. Williams. *Nuclear and Particle Physics.* Oxford Science Publications, 1992.

[76] A. A. Hamian. *The measurement of parity violation in proton-proton scattering at 221 MeV.* PhD thesis, University of Manitoba, 1998.

[77] J. Bland. The TRIUMF E497 parity violation experiment in the 221 MeV $\vec{p}p$ system: A complete analysis of the Feb97, Jul 98, May99 data runs. Master's thesis, University of Manitoba, 2001.

[78] Barry R. Holstein. *Weak Interactions in Nuclei.* Princeton University Press, 1989.

[79] David Griffiths. *Introduction to Elementary Particles.* Wiley, 1987.